Numerical Simulation of Miscible Fluid Flows in Porous Media

by

© Mohammad Jalal Ahammad
B. Sc.(Hons), M. Sc.

A thesis submitted to the
School of Graduate Studies
in partial fulfillment of the
requirements for the degree of
Master of Science.

Department of Computational Science
Memorial University of Newfoundland

May 2014

St. John's Newfoundland

Abstract

The study of miscible flow in porous media is an important topic in many disciplines of science and engineering, especially in the field of petroleum engineering. For example, Carbon dioxide (CO_2) may be injected into an oil reservoir in order to improve the oil recovery rates, which is called enhanced oil recovery (EOR). This thesis focuses on the study of a miscible displacement of two fluids, such as CO_2 and oil, in a porous medium. An upscaling methodology for modeling multiscale features of the flow and the porous medium has been studied, where the overall pressure drag and skin friction exerted on the porous medium has been modelled by combining the Darcy's law with a statistical mechanical theory of viscosity, which is an important contribution of this thesis.

A numerical methodology for capturing the multiphysics and multiscale nature of the governing motion has been studied. The temporal discretization employs the second order Crank-Nicolson scheme for viscous and diffusive phenomena, and an explicit method for all other terms. The nonlinear advection terms in the momentum equation has been treated with an Euler explicit flux form central finite difference method; however, the advection of the CO_2 mass flux has been treated with a streamline based Lagrangian method. In order to implement the Marker-and-Cell (MAC) scheme for resolving the incompressibility, a staggered arrangement of the velocity and pressure has been presented on a collocated grid. This approach enhances the implementation of a multigrid solver, and is a novel computational model for simulating miscible displacement processes. The performance of the Lagrangian method has been assessed with respect to an equivalent flux form upwind method.

The results indicate that the viscous forces play a significant role compared to the effect of permeability on miscible displacement of CO_2 and oil, where the injected

CO_2 displaces the residual oil without being distorted, thereby enhancing the recovery of hydrocarbon. Although the present results with an idealized model lacks from verifications with field measurements, findings of this thesis provide useful feedback to further investigations on CO_2 based EOR techniques.

"*Everything should be made as simple as possible, but not simpler.*" −Albert Einstein.

Acknowledgements

First, I am very grateful to my supervisor, Dr. Jahrul Alam, for accepting me as a graduate student in his research group. I would like to express my deepest gratitude to him for his continuous support, proper guidance, and patience during the research. Also special thanks to my supervisor for introducing me to such an interesting and challenging topic for my research and careful review of the manuscript.

I am grateful to the School of Graduate Studies and the Department of Computational Science for providing financial support and the department of Mathematics and Statistics for arranging the Teaching Assistantship. I am also grateful to the University of Chittagong, Bangladesh, for sanctioning study leave with full salary and providing a partial travel grant.

Thanks also to Mr. Edmund Loveless, Ex-lecturer, Department of Mathematics and Statistics, Memorial University of Newfoundland, for proof reading of the thesis with spacial care.

Finally, I am very grateful and thankful to my parents, my wife Monuara and numerous friends for their continuous support and love, especially my daughter, Jannat, who missed me, and I also generously missed her these last two years.

"If nature were not beautiful, it would not be worth studying it. And life would not be worth living." −Henry Poincare.

Contents

List of Tables

List of Figures

Abbreviations

CFD	:	Computational fluid dynamics
CN	:	Crank-Nicolson
DOF	:	Degrees of freedom
EOR	:	Enhanced oil recovery
GHG	:	Green house gas
MAC	:	Marker and cell
NSE	:	Navier-Stokes equations
PDE	:	Partial differential equation
REV	:	Representative elementary volume
SWAG	:	Simultaneously water and gas
TB	:	Terabytes
VAT	:	Volume average technique
VRI	:	Viscosity reducing injectant
WAG	:	Water altering gas

Nomenclature

C	:	Concentration field
D	:	Diffusion coefficient
F	:	Total force
$\mathcal{N}$	:	Number of grid points
P	:	Pressure
V	:	Total volume of the REV
U	:	Dimensionless velocity
H	:	Dimensionless length
h	:	Width of the channel
t	:	Time
$\boldsymbol{u}$	:	Velocity field
u	:	Horizontal velocity component
v	:	Vertical velocity component
F^P	:	Pressure drag
F^S	:	Skin friction
V_f	:	Fraction of volume of REV which occupies fluid
c_φ	:	Model parameter
L_x	:	Size of the domain along x-axis
L_y	:	Size of the domain along y-axis

n_x : Number of grid cells along x-axis

n_y : Number of grid cells along y-axis

$\mathcal{O}(\mu\text{m})$: Order of micrometre

$\mathcal{O}(\text{km})$: Order of kilometre

∇P : Pressure gradient

Δx : Grid space along x-axis

Δy : Grid space along y-axis

Δt : Time step

α : Ratio of viscosity

κ : Permeability

$\mu(C)$: Concentration dependent viscosity

μ_0 : Viscosity of oil

μ_s : Viscosity of solvent

ϕ : Porosity of the porous medium

μ_{eff} : Effective viscosity

ρ : Density

φ : Velocity potential

ν : Kinematic viscosity

ξ : Streamline parameter

λ : Boundary layer width

Da : Darcy number

Re : Reynolds number

Re_d : Reynolds number based on pore scale

Sc : Schmidt number

mm : Millimetre

μm : Micrometer

Chapter 1

Introduction

The study of fluid flows in porous media has received considerable attention due to the increasing interests in geophysics, thermal insulation, petroleum reservoirs, and many other areas in science and engineering. This thesis focuses on the numerical simulation of miscible displacement processes in porous media. The miscible displacement of a fluid by a second fluid has received an increasing attention to scientists, especially, to the oil industries, where a solvent, such as CO_2, is used to displace the residual oil that was trapped within pores of reservoir rocks. This residual oil may be up to 70% of the original oil in a reservoir, and cannot be recovered with typical primary and secondary techniques. The increasing demand of fuel has led scientists and engineers to give attention to the recovery of the residual oil. Therefore, studies with idealized oil reservoir models – also known as reservoir simulations – play an important role, and help mitigate the financial burden of field operations. As described by Chen (2007), numerical reservoir simulations are useful to predict the performance of a oil recovery project.

The study of the miscible flow of CO_2 and oil or saline is important for developing sophisticated oil recovery techniques, as well as for mitigating the challenges of global

warming due to human induced air pollution.

1.1 CO_2 in oil production techniques

Let us now present several oil production techniques. The study of these oil recovery techniques depends also on how modellers characterize the geological features of the reservoir. Thus, the oil recovery techniques requires basic concepts on modelling porous media and geological reservoirs.

1.1.1 Porous media and geological reservoirs

The concept of porous media is well-known by scientists, and used in many disciplines of applied sciences and engineering. A fluid flow through porous media has become a common interest to a number of interdisciplinary branches and, introduced an independent field of research.

A porous medium contains pores (void space) and solids, where pores are inter connected in such a way that a fluid can flow through it continuously. For instance, consider a large stack of gulf balls. Rocks, soil, and biological tissues (*e.g.* bones, kidneys) are examples of natural porous materials; on the other hand, cemented sandstone, water filter, and ceramics etc. are examples of artificial porous materials (Bear & Bachmat, 1990). Clearly, the distribution of the void space in a stack of gulf ball is different from that in a rock or collections of arbitrary shaped rocks. In other words, a porous material may be homogeneous or heterogeneous. A porous material is homogeneous with respect to a physical property, if this property does not change within the material. Otherwise, it is called a heterogeneous porous medium. Moreover, a porous material is referred to as an isotropic medium with respect to a property, if the property does not change with direction (Bear & Bachmat, 1990). In

practical applications, there is no absolute homogeneous and isotropic porous media in the oil reservoir fields. However, when a representative elementary volume (REV) is considered in a volume averaging process, the length scale of the REV is larger than the length scale of the pore scale. In addition, the length scale of the whole domain is larger than the length scale of the REV (Whitaker, 1986). The mean average of the fluid properties remain constant within the REV (deLemos, 2006). Under this consideration, we assume the homogeneous and isotropic porous media in our model.

A reservoir is a geological rock formation beneath the earth's surface, which contains fluids, such as oil or gas. This is often called the petroleum reservoir or the oil reservoir. In other words, a reservoir is a fluid saturated subsurface porous medium. In practice, a study of a fluid flow in a porous medium typically refers to an idealized realization of oil/gas flow in a reservoir. In this thesis, a porous medium refers to an oil reservoir, unless it is mentioned otherwise.

1.1.2 Primary and secondary oil recovery

Generally, the recovery of the crude oil from the reservoir begins with drilling wells into the ground. During an early period, oil is driven toward a production well by the natural high pressure of the reservoir. This is the primary recovery stage, when the pressure is the result of the combination of a number of natural and physical mechanisms. In the primary recovery stage, around 5-15% of the oil can be recovered (Chen *et al.*, 2006). This recovery stage continues until the natural pressure of the reservoir maintains a desired level.

When the natural underground pressure falls below a certain level, the pressure becomes insufficient to force the oil upward to the production well. Thus, the reservoir's pressure needs to be increased, and this can be accomplished by injecting an-

other fluid. Generally, water is injected into the reservoir during this process. This stage of the oil recovery is referred to as secondary oil recovery process. As reported by Sen (2008), at the end of the secondary oil recovery process, approximately 20-30% of the original oil can be recovered depending upon the properties of the crude oil and the characteristics of the reservoir. However, after the primary and secondary recovery processes, about 60-80% (Gerritsen & Durlofsky, 2005) of the original oil remains trapped into the pores which is the residual oil in a reservoir. Note that about 377 billion barrels of residual oil cannot be recovered from known oil fields in USA (Sen, 2008). Clearly, world's residual oil is much more than 377 billion barrels. Thus, an enhanced oil recovery process is an important topic.

1.1.3 Enhanced oil recovery

After the secondary recovery of the reservoir life time, a number of recovery methods are developed by scientists and engineers to extract remaining trapped crude oil from a mature oil field. These techniques are termed as an enhanced oil recovery (EOR) process. Usually, at this stage the recovery techniques attempt to alter rock-fluid interactions in the oil reservoir, and to enhance the recovery process. The techniques include: steam injection, chemical injection or gas injection (*i.e.* CO_2, N_2, methane). The main objectives of this process are to eliminate saturation of the residual oil, reduce the viscosity of oil, and increase the miscibility so that oil moves toward the production wells (Chen *et al.*, 2006). An effective EOR technique would mobilise the saturated oil, and form an oil bank that can move toward production wells. Gas or liquid injection can be miscible or immiscible to oil.

1.1.4 Miscible flow and miscible displacement

Let us consider that a fluid displaces another fluid. If the molecules of these two fluids are free to mix with each other depending on their physical conditions, then mixing begins through the interface between these two fluids. Such fluids are also known as miscible fluids. For example, water can mix with juice, syrup or ethanol in any proportions of these fluids. As a result, the water may not displace juice as a distinct phase. In contrast, the mixing between CO_2 and oil may occur in a way that, during the displacement process, these two fluids may remain well separated, and occupy approximately their own volume, where mixing occurs at molecular label through the interface (Udey & Spanos, 1993; Bai & Elsworh, 1995). Thus, a full understanding of such a miscible displacement process remains an active research topic in the field of petroleum engineering (Green & Willhite, 1998). A schematic diagram of the miscible displacement process is shown in Fig 1.1.

1.1.5 Immiscible two phase flow

On the other hand, if the flowing fluids are not miscible, the resulting migration is an immiscible displacement process, where two fluids remain fully separated. For example, when warm water or steam is injected into an oil reservoir to push the oil so that it moves to the production well, the resulting flow is an immisicible two-phase flow (Ehlers & Bluhm, 2002). Note that the displacement process of oil by CO_2 may also be immiscible, depending upon the condition of the crude oil and some other related properties (Farajzadeh, 2009).

In order to outline some benefits of CO_2 based EOR, table 1.1 presents the data on the production rate of oil from 4 different countries. Clearly, miscible displacement is more effective in Canadian oil fields (3600 bbl/day/field) compared to that in US

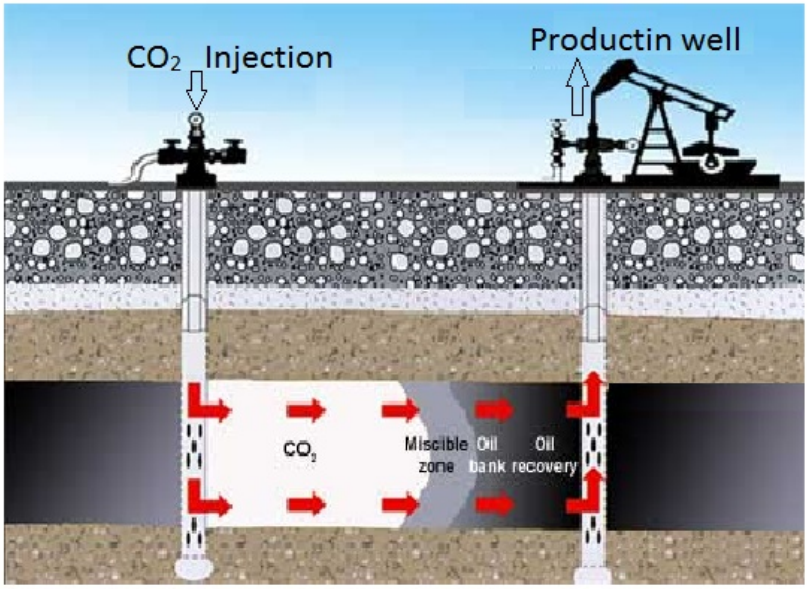

Figure 1.1: The miscible displacement oil by CO_2 has been presented schematically. The diagram depicts the vertical cross section of a reservoir where CO_2 is being injected through the injection well, and oil is being collected through the production well. The CO_2 and the oil are well separated; however, there is an overlap, where the mixing occurs. Further details of this diagram is given in Texas (2012).

(294 bbl/dat/field). Numerical modelling studies may identify potential techniques to improve the existing oil production rate.

Table 1.1: **Ongoing EOR projects using CO_2 and rate of production**

Location	Project type	Number	Production rate [bbl/day]
USA	Miscible (immiscible)	70(1)	206000(105)
Canada	Miscible	2	7200
Turkey	Immiscible	1	6000
Trinidad	Immiscible	5	320
	Source:(Farajzadeh, 2009)		

1.2 EOR as a carbon storage option

The CO_2 based EOR is closely related to the carbon capture and storage, which is the pilot project on mitigating the challenge of global warming due to human induced carbon emission, and has a notable impact on the environmental management (Gozalpour *et al.*, 2005; Holtz *et al.*, 2001). For example, the CO_2 emission from nuclear power plants may be easily captured and stored or reused for EOR (Farajzadeh, 2009). Fig 1.2 depicts the collection of CO_2 and its storage in offshore and onshore subsurface locations.

1.3 Challenges in the reservoir simulations

There are a number of unresolved challenges in reservoir simulations, which need to be addressed. According to Nobakht *et al.* (2007), accurate modelling of the effect of viscosity is one of the most challenging aspects of CO_2 based EOR process. Under

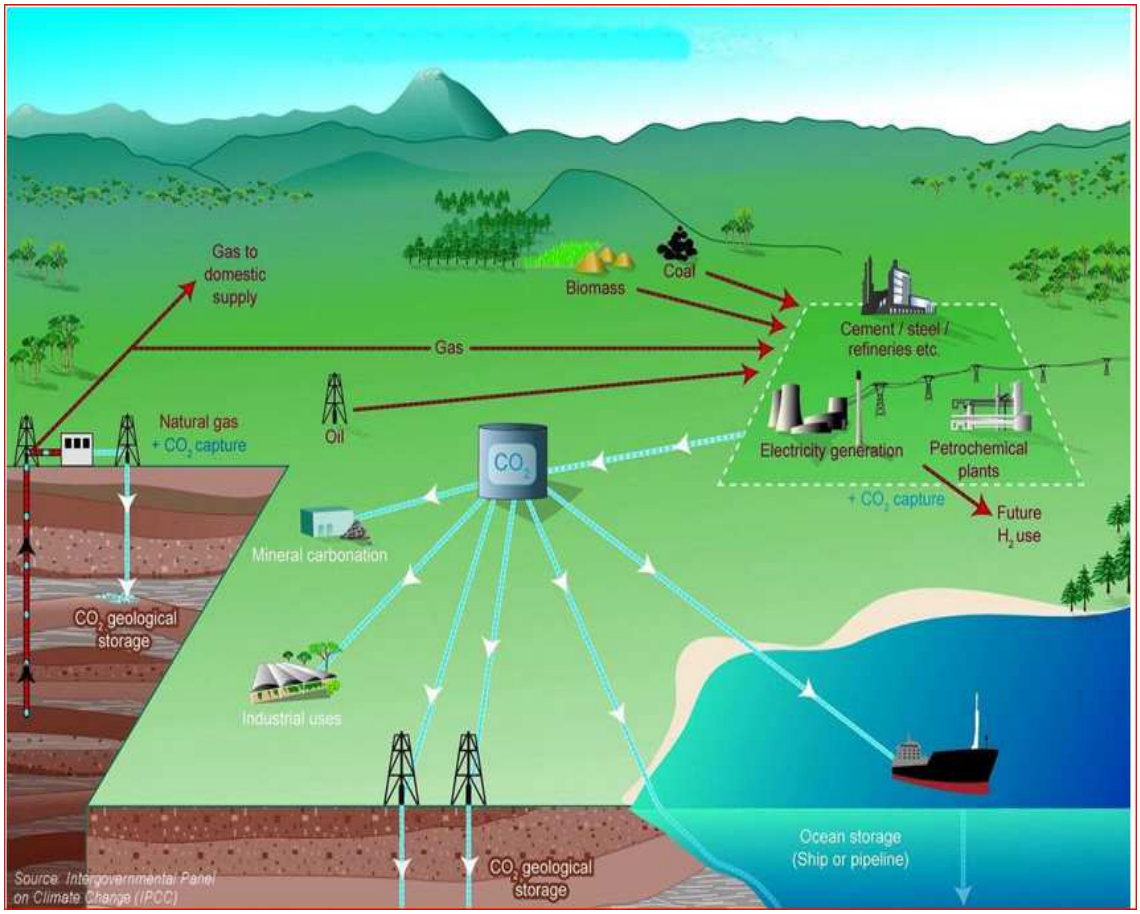

Figure 1.2: Schematic diagram of CO_2 collection and distribution.

typical reservoir conditions, the viscosity of CO_2 is less than that of crude oil. As a result, the viscosity of the flowing binary fluid (CO_2 and oil) play an important role on reducing the skin friction and the overall drag experienced by the reservoir rock. For example, in Fig 1.1, the viscosity of oil in the miscible zone will be less than that of the oil. However, an accurate prediction of the viscosity of the binary fluid in the miscible zone is an unresolved challenge. Furthermore, the availability of CO_2 and the cost of transportation must be considered for an efficient CO_2 based EOR process - a full discussion of which is outside the scope of this thesis. A principal focus of this thesis aims to understand how to control the effect of viscous forces in order to accelerate the recovery of residual oil.

Currently, the petroleum industry is one of the largest users of the high performance computing resources (see Islam *et al.*, 2010). Almost all aspects of the reservoir engineering problems – from well testing to the prediction of reservoir life – are analyzed with reservoir simulators. However, the lack of *a priori* real time data for model verification demands rigorous theoretical studies. For example, weather prediction computer models are verified with data obtained from a 'space shuttle' or a 'weather balloon', which is something that is difficult, if not impossible, in the field of reservoir modelling (Islam *et al.*, 2010). In this direction, there are two essential challenges: one is mathematical modeling of the flow physics and reservoir characteristics, and the other is the real time computational methodologies.

1.3.1 Mathematical model

The mathematical model is the most important factor for studying any fluid flow and the model should be as simple as possible, and represent the actual features of a specific flow as accurately as possible. The simplest reservoir model adopts the

Darcy's equation to approximate the conservation of momentum, where the effects of the viscous stress and inertial have been neglected (Islam *et al.*, 2010; Vafai & Tien, 1982). This approximation is fully justified with rigorous mathematical analysis and experiments with ideal flow of water through porous media. In other words, the Darcy's equation approximates the 'true' momentum transfer that occurs through pores of the medium by an 'approximation' that is representative at the 'field scale'. As mentioned by Bear (1972), the Darcy's equation remains valid when the Reynolds number is about 1. Insufficient approximation of the momentum transfer by the Darcy's equation was studied by a number of researchers (Vafai & Tien, 1982; Nguyen, 1986). Nguyen (1986) mentioned that standard Darcy flow analysis could be over-predicted the productivity rate of oil. Thus, it is needed an extended model to study the flow behavior in EOR process. The regime of a reservoir flow – where the Darcy's equation is appropriate, and where a more robust upscaling approximation is required – has been analysed thoroughly in recent years. Review of literature indicates that characterizing the reservoir heterogeneity, modeling the dynamics of binary fluids, and heat and mass transfer phenomena are among least understood topics (e.g., Nobakht *et al.*, 2007).

1.3.2 Computational challenges

The length of a petroleum reservoir is typically $\mathcal{O}(\text{km})$; for example, Jilin oil field in China is about 25 km long and 12 km wide (Yu *et al.*, 2012). The Weyburn oil field in Canada has a productive area of about 180 km^2 (Elsayed *et al.*, 1993). However, the average space between rocks, where the actual flow occurs, is $\mathcal{O}(\mu\text{m})$ (Popov *et al.*, 2009; Hasle *et al.*, 2007). Thus, for a typical reservoir that is 10 km long, 10 km wide, and 100 m deep, we need $10^{10} \times 10^{10} \times 10^{8}$ grid points for a simulation

which aims to capture the actual fluid flow with the spatial step size, $\Delta x = 1\,\mu$m. Pruess & Zhang (2008) attempted to determine the minimum Δx using the Darcy's equation, and found that $\Delta x = 1\,$mm is necessary to sufficiently resolve viscous fingering effects. With this resolution, $10^7 \times 10^7 \times 10^5$ grid points are needed. A naive estimate shows that we would require a computer memory in the range of 10^6TB – 10^{15}TB. Clearly, this is not possible with currently available computer resources, which explains the computational challenges of reservoir simulation. To meet this challenge, the development of sophisticated numerical techniques along with rigorous upscaling methodology are needed. The principal motivation of this thesis is along this direction.

1.4 Structure of the thesis

Chapter two presents a mathematical model of a miscible fluid flow in porous media. In this model, the classical Darcy's equation has been extended, where the characteristic length scale has been referred to as the meso-scale – between the field scale and the pore scale. A numerical modelling approach has been presented in chapter three. This model takes advantage of the multigrid solution technique in order to optimize the overall computation overhead. Chapter four introduces a novel streamline based Lagrangian methodology, which resolves the advection dominated mass transfer in a porous medium. Chapter five has been devoted to verification and validation of the present Lagrangian modelling system. In chapter six, the effects of permeability and viscous stress on the miscible displacement of oil by CO_2 has been investigated. Results indicate that accurate modelling of the viscous stress is more important than that of the permeability effects of reservoir rocks, in order to optimize the efficiency of oil recovery. Finally, the main conclusions of the thesis have been summarized

in chapter seven, where some related future research directions have been discussed briefly.

Chapter 2

A mathematical model for miscible flows in porous media

A petroleum reservoir is a formation of a porous medium which contains hydrocarbons (Islam *et al.*, 2010). Hydrocarbons are produced by drilling wells into the reservoirs. Before the final oil production, a number of simulations may provide useful feedback to the field operations. The ultimate goal of numerical simulations is the understanding of the reservoir fluid flow and the prediction of the overall reservoir performance (Islam *et al.*, 2010). The reservoir simulation mainly depends on a bonafide physical model, the development of a mathematical model, an optimal numerical method to discretize the mathematical model, and an efficient computational algorithm (Chen, 2007). The physical model aims at representing the geological features of a reservoir, which resolves essential features as much as possible, and a mathematical model expresses the dynamics of the flow inside the reservoir. An optimal numerical method helps to approximate the model equations, and an efficient computational algorithm helps to get the most accurate solution by implementing a numerical method (Chen, 2007).

2.1 Objective of the chapter

This chapter concentrates on the development of a mathematical model, which aims to study an upscaling methodology for the flow of miscible fluids in porous media. The main view of this upscaling methodology is to approximate the actual flow behavior at pore scale to a much larger scale, which may be called the meso-scale. The volume averaging technique (VAT) has been studied in order to upscale the fluid flow in a porous medium. A statistical mechanical approach is applied to address the skin friction exerted by the porous media.

2.2 Upscaling of a flow in porous media

The upscaling methodology aims to model the 'true' flow through the pores of a reservoir by an overall 'approximation' of the flow in the reservoir. This may be explained by the schematic scale separation diagram, which is adopted from Popov *et al.* (2009) and presented in Fig 2.1. In Fig 2.1, the left panel, the top right panel, and the bottom right panel illustrate the field scale, meso-scale, and micro-scale, respectively. The actual flow occurs at the pore scale which is $\mathcal{O}(\mu\text{m})$ and is known as the micro scale (Popov *et al.*, 2009; Hasle *et al.*, 2007). The upscaling methodology aims to develop a model to represent the rocks and the average flow at meso-scale or at field scale (Elsayed *et al.*, 1993). Clearly, upscaling at the meso-scale may be more accurate compared to upscaling at the field scale. In the field operation, in order to get some quick and coarse estimate, field scale upscaling is necessary. Thus, traditional reservoir models typically adopt the field scale upscaling (see, Garibotti & Peszyǹska, 2009). There may be two possible approaches: i) employ the field scale model to simulate the flow using a mesh that is as fine as possible; ii) employ

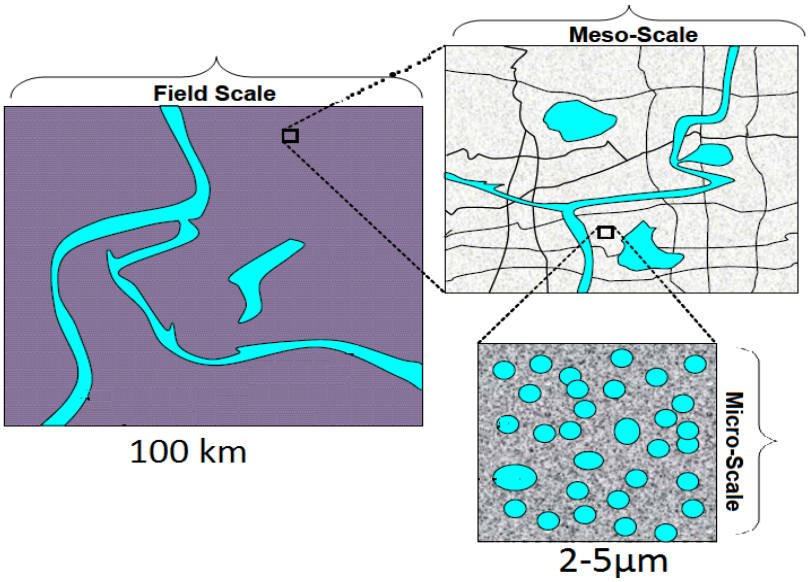

Figure 2.1: The multiscale nature of a reservoir has been depicted schematically. The left panel presents an entire reservoir, where only large fractures (region with the green color) may be realized. An overall understanding of the 'field scale' flow in this reservoir of length 100 km is desired. An intermediate or meso-scale (the dimension of the meso-scale is between kilo meter (km) and, micrometer (μm); here we consider meter (m)) is depicted in the top right panel, where the tiny pores are not realized. The bottom right pannel depicts the tiny pores of size $\mathcal{O}(\mu\text{m})$. Clearly, a numerical simulation may adopt any of these scales, depending on the aim of the simulation.

a meso-scale model which resolves more features of the flow compared to the field scale model, and use a relatively coarser mesh to simulate the flow. Another view of upscaling indicates that meso-scale models may be more appropriate for research and understanding the dynamics, and field scale models may be more appropriate for a real time or faster than real time prediction of the overall reservoir life cycle (see, Whitaker, 1996). Upscaling is done through an averaging process. Both the field scale and the meso-scale upscaling model can be developed through the volume averaging approach.

2.3 Volume averaging technique (VAT)

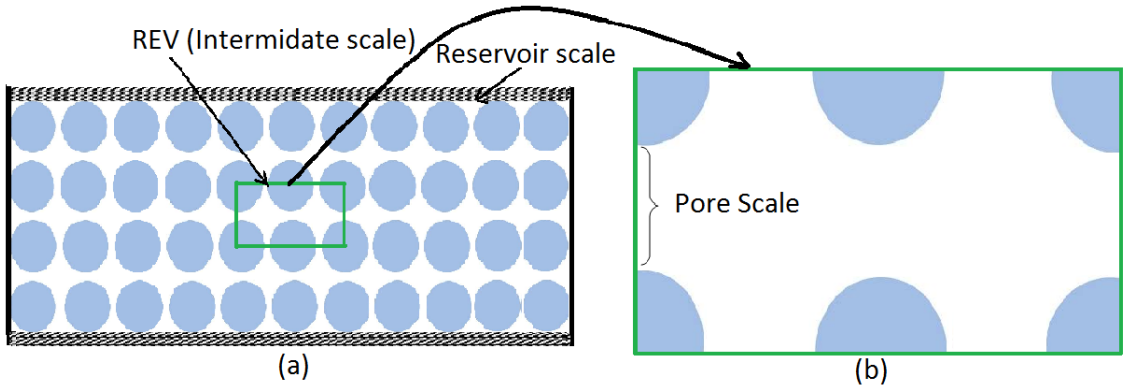

Figure 2.2: Schematic diagram of an isotropic porous medium where dark shapes are solids (rocks). (a) An idealized reservoir, and (b) Representative elementary volume (REV).

Let us consider an idealized oil reservoir, which is an isotropic porous medium as shown in Fig 2.2(a). In this figure, the circular dark shapes represent solids (rocks) and the void space is filled with a fluid such as crude oil. Fig 2.2(b) is a representative elementary volume (REV), which contains both the void and the solid phases. Let V

and V_f denote the entire volume of an REV and the volume of fluid within an REV, respectively. The porosity or the void fraction is given by $\phi = \frac{V_f}{V}$. In an REV, any flow property is an average, which is an approximation to the actual flow through pores, and has the same value everywhere within the REV, regardless of the rock or the fluid (deLemos, 2006). In a numerical model, an REV may be considered the smallest computational unit.

The volume average of any flow property $\widetilde{\psi}$ is defined by

$$\psi^D \equiv \langle \widetilde{\psi} \rangle^v = \frac{1}{V} \int_V \widetilde{\psi} dV,$$

which is called the volume average (deLemos, 2006). For simplicity we denote the volume average, $\langle \widetilde{\psi} \rangle^v$ by ψ^D. Since the average ψ^D does not vary within the REV, we can place a grid point anywhere within the REV (generally at the center). In practice, a reservoir model does not distinguish whether the grid point is on the solid phase or on the fluid phase. Clearly, the volume average is more effective, when the actual flow does not have a significant variation within the REV. The volume average may also be considered as a field scale realization of the true flow when the size of the REV represents the characteristic of the field scale.

However, if the volume of the REV is reduced, spatio-temporal variation of the flow in the REV may become important, and a modified averaging process is needed. For example, both experiments and numerical simulations exhibited sharp changes of streamlines for a slowly moving fluid past an obstacle at low Reynolds number ($0 < Re < 100$). These fluctuations may not propagate far from the obstacle. To model this effect, an intrinsic average is defined by

$$\psi \equiv \langle \psi \rangle^i = \frac{1}{V_f} \int_V \widetilde{\psi} dV.$$

One finds that $\psi^D = \phi\psi$; *i.e.* a fraction of ψ is captured by the volume average ψ^D,

where porosity, $\phi = V_f/V$. In other words, $\psi = \psi^D + \psi'$, where ψ' is the missing information in ψ^D. Furthermore, $\tilde{\psi} = \psi^D + \psi' + \psi''$, where $\langle\psi''\rangle^v = \langle\psi''\rangle^i = 0$.

Some properties of the volume averaging process have been listed below, where $\rho(\boldsymbol{x}, t)$ and $\boldsymbol{u}(\boldsymbol{x}, t)$ denote density and velocity, respectively. (see, Whitaker, 1969; Slattery, 1967; Gray & Lee, 1977; deLemos, 2006)

$$(\nabla\rho)^D = \nabla(\phi\rho) + \frac{1}{V}\int_{A_i} \boldsymbol{n}\widetilde{\rho}dS, \tag{2.1}$$

$$(\nabla\cdot\boldsymbol{u})^D = \nabla\cdot(\phi\boldsymbol{u}) + \frac{1}{V}\int_{A_i} \boldsymbol{n}\cdot\widetilde{\boldsymbol{u}}dS, \tag{2.2}$$

$$\left(\frac{\partial\boldsymbol{u}}{\partial t}\right)^D = \frac{\partial}{\partial t}(\phi\boldsymbol{u}) - \frac{1}{V}\int_{A_i} \boldsymbol{n}\cdot(\boldsymbol{u}_i\widetilde{\boldsymbol{u}})dS, \tag{2.3}$$

where A_i, $\boldsymbol{n}$, and $\boldsymbol{u}_i$ are interfacial area, unit normal vector to A_i, and velocity of the fluid phase within an REV, respectively.

2.4 Field scale upscaling

Let us consider the vector form of momentum conservation equation within an REV

$$\rho\left(\frac{\partial\boldsymbol{u}^D}{\partial t} + \boldsymbol{u}^D\cdot\nabla\boldsymbol{u}^D\right) = -\nabla P^D + \mu\nabla\cdot\nabla\boldsymbol{u}^D + \boldsymbol{F},$$

where $\boldsymbol{u}^D$, P^D, ρ, μ and F are the average velocity, average pressure within an REV, the density, viscosity of the fluid and the pressure drag and skin friction exerted by the porous medium, respectively. Now we integrate the above equation over the control volume, V of an REV,

$$\int_V \rho\left(\frac{\partial\boldsymbol{u}^D}{\partial t} + \boldsymbol{u}^D\cdot\nabla\boldsymbol{u}^D\right)dV = \int_V \left(-\nabla P^D + \mu\nabla\cdot\nabla\boldsymbol{u}^D + \boldsymbol{F}\right)dV,$$

Applying the divergence theorem to the right-hand side and Gauss's theorem to the second term of the left-hand side, yields

$$\frac{\partial}{\partial t}\int_V \rho \boldsymbol{u}^D dV + \iint_S \rho(\boldsymbol{u}^D\boldsymbol{u}^D)\cdot\boldsymbol{n}dS = \iint_S \left[-P^D + \mu(\nabla\boldsymbol{u}^D + (\nabla\boldsymbol{u}^D)^T)\right]\boldsymbol{n}dS + \int_V \boldsymbol{F}dV, \tag{2.4}$$

where the superscript T denotes transpose. Here we have used $\boldsymbol{u}^D\cdot\nabla\boldsymbol{u}^D = \nabla\cdot(\boldsymbol{u}^D\boldsymbol{u}^D)$ (which follows from the divergence-free condition) in order to obtain a form to which Gauss's theorem applies.

According to Darcy's experiment on water flow through a sand column, the total drag is proportional to the average velocity in a way that it depends on the viscosity, μ, of the fluid and permeability, κ, of the medium. Thus, a widely accepted model for the drag force is given by

$$\boldsymbol{F} = -\frac{\mu}{\kappa}\boldsymbol{u}^D. \tag{2.5}$$

Since the average flow, $\boldsymbol{u}^D$, does not vary in the REV, thus eq (2.4) may be simplified to get

$$\nabla P^D = -\frac{\mu}{\kappa}\boldsymbol{u}^D. \tag{2.6}$$

The Darcy's model (2.6) is an upscaling of the flow from pore scale to a typically resolved scale. This model has neglected the effects of both inertia and viscous terms. Bear (1972) suggested that the onset of inertia effect begins at the pore scale based Reynolds number, Re_d, between 3 to 10. Fancher & Lewis (1933) reported that $0.03 \leq Re_d \leq 1000$ is the range of the pore scale based Reynolds number for the onset of inertia effect. Also a number of research works reported the deviation from Darcy's model (Hubbert, 1956; Gavin, 2004; Yu *et al.*, 2012). Jenny *et al.* (2006) proposed to solve (2.6) at sufficiently high resolution to minimize large errors. However, a high resolution simulation violets the fundamental assumption behind Darcy's model (Ma & Ruth, 1993). Thus a generalized upscaling model is needed for the high resolution

simulations in reservoir flow.

2.4.1 A field scale model for the miscible flow of CO_2 and oil

Peaceman & Rachford (1962) proposed a mathematical model for the simulation of miscible flow of CO_2 and oil in a porous medium. In terms of volume averaged quantities, the model of Peaceman & Rachford (1962) takes the form (e.g., Booth, 2008)

$$\nabla \cdot \boldsymbol{u}^D = 0, \tag{2.7}$$

$$\nabla P^D = -\frac{\mu}{\kappa}\boldsymbol{u}^D, \tag{2.8}$$

$$\phi\frac{\partial C^D}{\partial t} + \boldsymbol{u}^D \cdot \nabla C^D = D\nabla^2 C^D, \tag{2.9}$$

where $C(\boldsymbol{x}, t)$ is the volume fraction or dimensionless concentration of CO_2 in oil, and μ is the viscosity of the binary mixture. In general, there is no standard relationship for the viscosity of a mixture of two fluids (Booth, 2008). However, commonly used relationships are $\mu(C) = [C\mu_s^{-1/4} + (1-C)\mu_0^{-1/4}]^{-4}$ (Koval, 1963), Lorenz-Bray-Clark mode (Lorenz *et al.*, 1964), and $\mu(C) = \exp(C\ \ln(\mu_0/\mu_s)$ (Sahu *et al.*, 2009), where μ_0 and μ_s are viscosity of the oil and the CO_2, respectively. In Fig 2.3, normalized $\mu(C) = [C\mu_s^{-1/4} + (1-C)\mu_0^{-1/4}]^{-4}$ has been presented, where we see that the mixture viscosity is nonlinearly dependent on the concentration of the solvent, and when the ratio μ_o/μ_s increases, the viscosity of the binary mixture falls off quickly at low values of C. However, a true relationship between the viscosity and concentration is a subject of ongoing research (Jha *et al.*, 2013; Homsy, 1987). In addition, the field scale model based on the Darcy's experiment was questioned by a number of researchers.

The verification of eq (2.8) for representing the conservation of momentum was challenged by a number of researchers. In 1901, Forchheimer argued that inertial

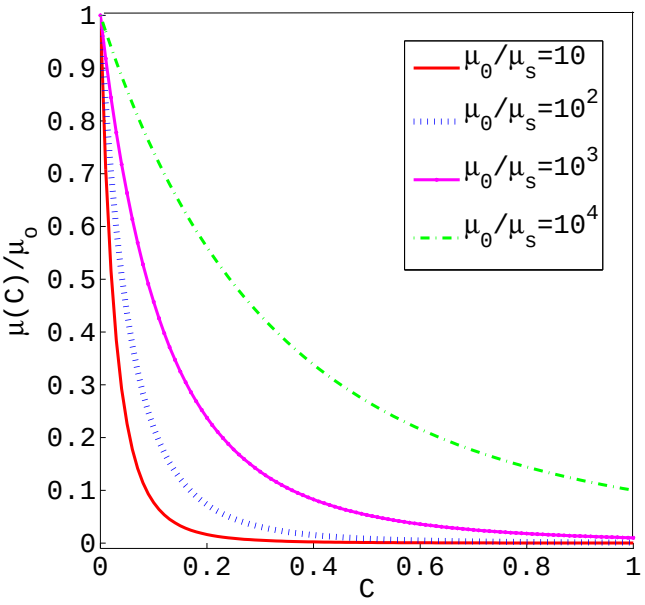

Figure 2.3: The dependence of mixture viscosity, $\mu(C) = \left[C\mu_s^{-1/4} + (1-c)\mu_0^{-1/4}\right]^{-4}$ on the concentration, C. Mixture viscosity is normalized by the oil viscosity, μ_0. The graphs are plotted for the various mobility ratio, μ_0/μ_s, where μ_s is solvent viscosity.

effects cannot be neglected if the Reynolds number exceeds a value about 10. Ergun (1952) performed experiments with fluid flow through packed columns and found the range of the critical value of the Reynolds number is 3 to 10. Brinkman (1947) studied the importance of viscous stress, which has been neglected in eq (2.8). As a result, eq (2.8) may be extened to Darcy-Brinkman-Forchheimer model by including suggested corrections. The extended model is also supported by many other scientists (e.g., Yu *et al.*, 2012; Islam *et al.*, 2010; Garibotti & Peszyǹska, 2009; Nguyen, 1986; Soni *et al.*, 1978). Nguyen (1986) found that the prediction of productivity performance by (2.8) in some circumstances was over-predicted.

Without going to further detailed review on the field scale model, which is also given by Yu *et al.* (2012), let us present a meso-scale model based on the intrinsic averaging process.

2.5 A meso-scale upscaling model

The conservation laws for mass and momentum for the 'true' incompressible flow at pore-scale are given by

$$\rho\left(\frac{\partial\widetilde{\boldsymbol{u}}}{\partial t}+\widetilde{\boldsymbol{u}}\cdot\nabla\widetilde{\boldsymbol{u}}\right)=-\nabla\widetilde{P}+\mu\nabla^2\widetilde{\boldsymbol{u}},\quad \nabla\cdot\widetilde{\boldsymbol{u}}=0,$$

where $\widetilde{\boldsymbol{u}}$, $\widetilde{P}$, ρ, and μ are velocity of the fluid flow, pressure, density of the fluid, and viscosity of the fluid, respectively.

Taking the volume average of these equations, and using the properties listed in the previous section, we get (deLemos, 2006; Guo & Zhao, 2002; Hsu & Cheng, 1990)

$$\nabla\cdot\boldsymbol{u}^D=0, \tag{2.10}$$

$$\rho\left(\frac{\partial\boldsymbol{u}^D}{\partial t}+\boldsymbol{u}^D\cdot\nabla(\boldsymbol{u}^D/\phi)\right)=-\nabla(\phi P)+\mu\nabla^2\boldsymbol{u}^D+\boldsymbol{R}, \tag{2.11}$$

where $\boldsymbol{R} = -\frac{1}{V}\int_{A_f} \boldsymbol{n}\widetilde{P}dS + \frac{\mu}{V}\int_{A_f} \boldsymbol{n}\cdot(\nabla\widetilde{\boldsymbol{u}})dS$ is the total drag force per unit volume due to the presence of the porous matrix. See Chapter 4 of deLemos (2006) for a detailed derivation of this averaged form of the equations. In order to obtain (2.8) when variation of $\boldsymbol{u}^D$ is neglected in (2.11), one would take $\boldsymbol{R} = \phi\boldsymbol{F}$, where $\boldsymbol{F}$ is given by (2.5).

Using $\boldsymbol{u}^D = \phi\boldsymbol{u}$, where $\boldsymbol{u}^D$ and $\boldsymbol{u}$ are volume average and intrinsic average, respectively, and assuming that ϕ is a constant, we obtain

$$\nabla\cdot\boldsymbol{u} = 0, \tag{2.12}$$

$$\rho\left(\frac{\partial\boldsymbol{u}}{\partial t} + \boldsymbol{u}\cdot\nabla\boldsymbol{u}\right) = -\nabla P + \mu\nabla^2\boldsymbol{u} + \boldsymbol{F}, \tag{2.13}$$

where $\boldsymbol{F}$ represents the total force which accounts for the pressure and skin friction. We need to parametrized this $\boldsymbol{F}$.

2.5.1 A simple model of $\boldsymbol{F}$ for a miscible flow in a porous medium

We consider that the solvent induced mixture viscosity is given by $\mu(C) = \mu_0(1 + \mu^c(x,y))$, where μ_0 is the oil viscosity, and the spatially dependent component $\mu^c(x,y)$ is an 'induced' viscosity due to the presence of the solvent molecules. Therefore, accepting the effect of viscosity due to concentration, eq (2.5) takes the form

$$\boldsymbol{F} = -\frac{\phi\mu_0}{\kappa}\boldsymbol{u} + \boldsymbol{F}^s, \tag{2.14}$$

where $\boldsymbol{F}^s$ represents the drag force per unit volume due to the presence of the solvent and the porous matrix, and may be modelled by using a statistical mechanical theory.

The statistical mechanical theory of viscosity assumes that the activated collision of molecules from one equilibrium state to another state induces a potential barrier,

and the molecules have to overcome this potential barrier in response to a shearing stress (see, Alam & Ahammad, 2013). For a Newtonian flow of a solvent-oil model, the ratio of the shearing stress to the rate of deformation is proportional to the potential barrier, μ^c. Therefore, μ^c can be related to the solvent density through the Maxwell's equation, which leads to

$$\nabla^2 \mu^c = \frac{\mu^c}{\lambda^2}, \tag{2.15}$$

where λ is a dimensionless distance from the solid phase measuring a viscous boundary layer (for details see, Alam & Ahammad, 2013). Note, a solution of the eqn.(2.15) for μ^c can be found by using Dirichlet boundary condition in the x direction and Neumann boundary condition in the y direction in a rectangular domain. Following Alam & Ahammad (2013), we obtain $\boldsymbol{F}^s = \frac{Q}{\kappa}\frac{\mu_0 \mu^c}{\lambda^2}$, where Q is the volume flow rate of the solvent-oil mixtures. Note that, the solvent is used to increase the flow rate of the solvent-oil mixtures.

2.6 The model equations for miscible flow in porous media

The final set of model equations are,

$$\nabla \cdot \boldsymbol{u} = 0, \tag{2.16}$$

$$\rho\left(\frac{\partial \boldsymbol{u}}{\partial t} + \boldsymbol{u}\cdot\nabla\boldsymbol{u}\right) = -\nabla P + \mu\nabla^2\boldsymbol{u} + \boldsymbol{F}, \tag{2.17}$$

$$\frac{\partial C}{\partial t} + \boldsymbol{u}\cdot(\nabla C) = D\nabla^2 C, \tag{2.18}$$

where $\boldsymbol{F} = -\frac{\phi\mu_0}{\kappa}\boldsymbol{u} + \frac{Q}{\kappa}\frac{\mu_0\mu^c}{\lambda^2}$.

2.6.1 Dimensionless form of the model equations

Let us make the model equations dimensionless by introducing

$$\tilde{x} = \frac{x}{H}, \quad \tilde{\boldsymbol{u}} = \frac{\boldsymbol{u}}{U}, \quad \tilde{t} = \frac{Ut}{H} \quad \text{and} \quad \tilde{P} = \frac{P}{\rho U^2}.$$

Using these dimensionless variables, the model eqns.(2.16 - 2.18) become

$$\tilde{\nabla} \cdot \tilde{\boldsymbol{u}} = 0,$$

$$\frac{\partial \tilde{\boldsymbol{u}}}{\partial \tilde{t}} + \tilde{\boldsymbol{u}} \cdot \tilde{\nabla} \tilde{\boldsymbol{u}} = -\tilde{\nabla} \tilde{P} + \frac{\alpha}{Re} \tilde{\nabla}^2 \tilde{\boldsymbol{u}} - \frac{\phi}{ReDa} \tilde{\boldsymbol{u}} + \frac{c_\varphi}{\lambda^2 ReDa} \tilde{\mu}^c \nabla \tilde{\varphi},$$

$$\text{and} \quad \frac{\partial C}{\partial t} + \tilde{\boldsymbol{u}} \cdot \tilde{\nabla} C = \frac{1}{ReSc} \tilde{\nabla}^2 C,$$

Here Q, representing a steady state, incompressible, and irrotational component of the velocity, has been written in terms of a velocity potential, φ, and c_φ is an arbitrary constant, considered as a model parameter and $\alpha = \frac{\mu_{\text{eff}}}{\mu_0}$ is viscosity ratio. For simplification, one may omit 'tilde' notation from dimensionless quantities because the rest of the thesis will use only dimensionless quantities unless otherwise mentioned. Thus, the dimensionless form of the model equations are

$$\nabla \cdot \boldsymbol{u} = 0, \tag{2.19}$$

$$\frac{\partial \boldsymbol{u}}{\partial t} + \boldsymbol{u} \cdot \nabla \boldsymbol{u} = -\nabla P + \frac{\alpha}{Re} \nabla^2 \boldsymbol{u} + \boldsymbol{F}, \tag{2.20}$$

$$\frac{\partial C}{\partial t} + \boldsymbol{u} \cdot \nabla C = \frac{1}{ReSc} \nabla^2 C, \tag{2.21}$$

where

$$\boldsymbol{F} = -\frac{\phi}{ReDa} \boldsymbol{u} + \frac{c_\varphi}{\lambda^2 ReDa} \mu^c \nabla \varphi.$$

The dimensionless numbers are defined as follows: Reynolds number, $Re = \frac{UH}{\nu}$; Darcy number, $Da = \frac{\kappa}{H^2}$; Schmidt number, $Sc = \frac{\nu}{D}$. The eqns.(2.19, 2.20, and 2.21) constitute the model equations.

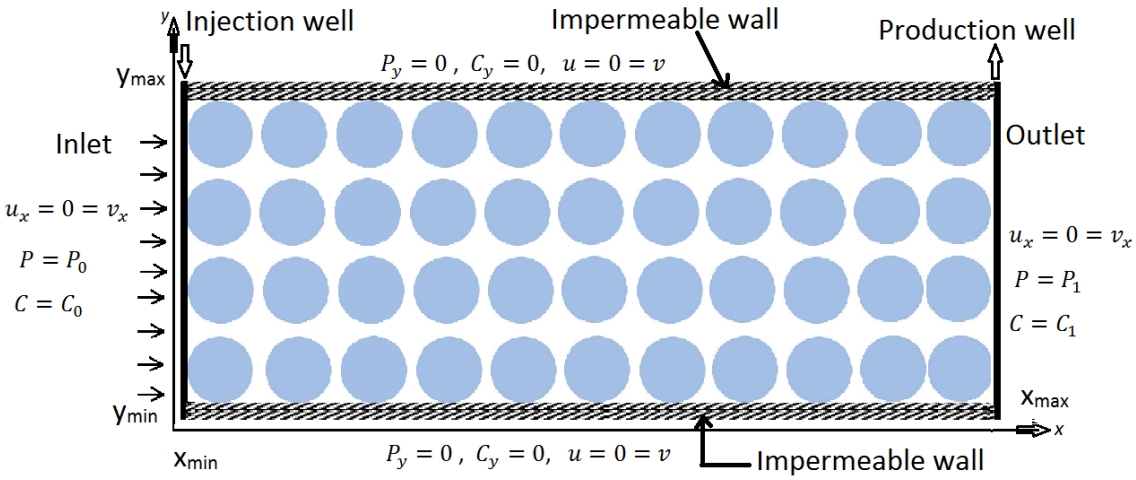

Figure 2.4: Schematic diagram of the flow region with boundary conditions. Dark shapes are solid (rock), white spaces are void spaces.

2.6.2 Boundary conditions

The mathematical models to study fluid flows are not complete unless necessary boundary and initial conditions are specified. We consider a rectangular idealized oil reservoir to study flow in porous media. Usually, oil reservoirs are horizontally long and, top and bottom boundaries are attached with an impermeable wall. We assume an injection well (inlet) at one end and a production well (outlet) at the other end. Thus, there will be no flow along the top and bottom boundaries, and fluid will move horizontally. The computational domain for a two-dimensional incompressible flow through porous media is depicted schematically in Fig 2.4 with boundary conditions, where dark shapes represent solids (rocks). We assume that the porous media is homogeneous and isotropic, thus the permeability and porosity remain uniform over the flow domain. The computational domain can be expressed as

$$\mathcal{D} = \{(x, y) : x_{\min} \leq x \leq x_{\max},\ y_{\min} \leq y \leq y_{\max}\},$$

which is considered as the flow simulation domain. We divide the domain into discrete points known as grid points as $(x_i, y_j) = (i\Delta x, j\Delta y)$ for $i = 1,\ 2,\ 3,\ ...\ n_x$, and $j = 1,\ 2,\ 3,\ ...\ n_y$, where Δx, Δy, n_x and n_x are grid space along x-axis, grid space along y-axis, number of grid cells along x-axis and number of grid cells along y-axis, respectively. We consider no-slip boundary condition on the top and bottom walls and Neumann boundary condition at the inlet and outlet boundaries for the velocity field. We adopt Dirichlet boundary condition at input and output boundaries and Neumann boundary condition on the top and bottom walls for the concentration field. Pressure is prescribed at inlet and outlet, while zero-pressure gradients are prescribed on walls. This means we use Dirichlet type boundary condition at inlet and outlet boundaries, and a Neumann type boundary condition at the top and bottom walls for pressure. For the velocity potential we use Dirichlet type boundary condition at inlet and outlet boundaries, and a Neumann type boundary condition at the top and bottom walls. The boundary conditions can be expressed mathematically as:

$$P(x_{\min}, y) = P_0 \text{ and } P(x_{\max}, y) = P_1,$$

$$0 = \Big(P_y\Big)_{(x,y_{\min})} \text{ and } 0 = \Big(P_y\Big)_{(x,y_{\max})},$$

for a pressure field,

$$u(x, y_{\min}) = 0 = v(x, y_{\min}) \text{ and } u(x, y_{\max}) = 0 = v(x, y_{\max}),$$

$$0 = \Big(u_x\Big)_{(x_{\min},y)} = \Big(v_x\Big)_{(x_{\min},y)} \text{ and } 0 = \Big(u_x\Big)_{(x_{\max},y)} = \Big(v_x\Big)_{(x_{\max},y)},$$

for a velocity field,

$$C(x_{\min}, y) = C_0 \text{ and } C(x_{\max}, y) = C_1,$$

$$0 = \Big(C_y\Big)_{(x,y_{\min})} \text{ and } 0 = \Big(C_y\Big)_{(x,y_{\max})},$$

for a concentration field,

$$\varphi(x_{\min}, y) = 1 \text{ and } \varphi(x_{\max}, y) = 0,$$

$$0 = \Big(\varphi_y\Big)_{(x,y_{\min})} \text{ and } 0 = \Big(\varphi_y\Big)_{(x,y_{\max})},$$

for a velocity potential,

where P_y, C_y, u_x, v_x, and φ_y define the differentiation as, $P_y = \frac{\partial P}{\partial y}$, $C_y = \frac{\partial C}{\partial y}$, $u_x = \frac{\partial u}{\partial x}$, $v_x = \frac{\partial v}{\partial x}$, and $\varphi_y = \frac{\partial \varphi}{\partial y}$, respectively.

2.7 Summary

We have developed a mathematical model to approximate the miscible displacement flows in porous media at the meso-scale. A statistical mechanical theory of binary fluids has been applied to address skin friction exerted by the porous media so that oil viscosity can be reduced if a solvent is added. This model is a generalization of the Darcy-Peaceman model, because Darcy's law can be retained from the momentum equation of this model when flow is incompressible, steady state and viscous force is balance by inertia force. The dimensionless form of the model equations with proper boundary conditions have been presented. In the next chapter, we will discuss computational methodology for the approximate solutions of the model equations for miscible flow.

Chapter 3

A multiscale computational methodology for miscible flow

The numerical simulation of miscible flow and transport in a subsurface porous media is a challenging endeavor because an extremely large number of the computational degrees of freedom (DOF) is necessary in order to resolve the flow from the pore scale to the reservoir scale. A rigorous upscaling approximation of the true flow truncates the number of DOFs, as well as captures the most important physical features which interact from pore-scale to field-scale. The upscaling methodology developed in this thesis features transient behaviour in a range of length scales, and, as a result, a fast numerical solution technique needs to be developed (e.g. see Ewing, 1983). This thesis employs a streamline based Lagrangian method and a multilevel method for studying miscible mass transfer mechanisms, and the present chapter outlines the development of a multilevel solution methodology for a miscible flow in porous media so that the overall computational workload remains asymptotically optimal. In other words, if the total number of grid points, $\mathcal{N}$, increased due to the need of resolving fine scale features of the flow, the CPU time would remain approximately $\mathcal{O}(\mathcal{N})$.

3.1 Computational methodology

3.1.1 Treatment of velocity and pressure calculation

Harlow & Welch (1965) developed a method to solve the incompressible Navier-Stokes equations for studying free surface flow. This method is often known as MAC method (Pletcher *et al.*, 2013). In this method, the scheme was based on a staggered grid to calculate the velocity and pressure. This method had the advantage of a more compact finite difference stencil and decoupling between the velocity and pressure fields(Johnson, 1996). In addition, the convergence of the pressure Poisson equation is satisfied automatically (Pletcher *et al.*, 2013). In this method, first a velocity field is to be known at the beginning of the cycle either as initial condition or calculated from previous time step. However, it is necessary to ensure conservation of mass by satisfying the incompressibility condition (2.20). Harlow & Welch (1965) showed that this requirement can be fulfilled by staggering the velocity and pressure. In this staggered grid, pressure is stored at the cell centre and velocity on the cell interface. In contrast, a collocated or nonstaggered grid stores the velocity and pressure at each collocation mesh.

We use the MAC method on a virtual staggered grid to calculate pressure. This grid is displayed in Fig 3.1. In this figure, the solid lines represent a virtual staggered grid on a collocated grid which is represented by the dashed lines. Here the symbols '►', '▲' and '○' represent locations of the stream wise velocity, span velocity, and pressure, respectively. The 5-point stencil for the MAC method to solve the pressure equation is exhibited in Fig 3.1, and the boundary conditions are described symbolically in Fig 3.1(a) only for the limited spaces on the other figures. In the collocated grid, we have velocity and pressure on each grid point. In order to ensure a staggered

grid we are considering a cell marked with solid line where pressure is at the center and velocity on the interface of the cell as shown in Fig 3.1. After calculating pressure on a staggered grid with the MAC scheme, then we consider another cell to calculate pressure on each grid point. Following this algorithm we are calculating pressure on each grid cell using a virtual staggered grid in the multilevel grid, whereas in the original MAC method, pressure was not calculated on each grid point. Next we discuss the multilevel grid generation.

3.1.2 Multilevel grid generation

For $x \in [0,1]$, we can define a dyadic grid at level $l \geq 0$ by

$$\mathcal{G}_x^l = \{x_i^l \in [0,1] : x_i^l = 2^{-l}i,\ i = 0, \ldots, 2^l,\ l < \infty\}.$$

A two-dimensional grid of the unit square $[0,1] \times [0,1]$ is obtained by taking the tensor product of two one-dimensional grids $\mathcal{G}_x^l$ and $\mathcal{G}_y^l$; *i.e.*

$$\mathcal{G}^l = \mathcal{G}_x^l \times \mathcal{G}_y^l.$$

This dyadic grid generation is simple, and can be applied to any rectangle. Fig 3.1 presents an example of a multilevel grid of a rectangle at 3 different levels. Clearly, $\mathcal{G}^l \subset \mathcal{G}^{l+1}$.

In order to approximately satisfy the conservation of mass, we want to arrange the velocity and pressure on a staggered grid, which adds a further challenge to implement a multilevel solver. Harlow & Welch (1965) provides further details of the staggered grid approach. We have implemented a staggered arrangement which is discussed in the previous section. The sequence of staggered grids obtained this way is automatically nested, and does not require an interpolation of velocity (see, Harlow & Welch, 1965). Note that the approach of Harlow & Welch (1965) interpolates velocity

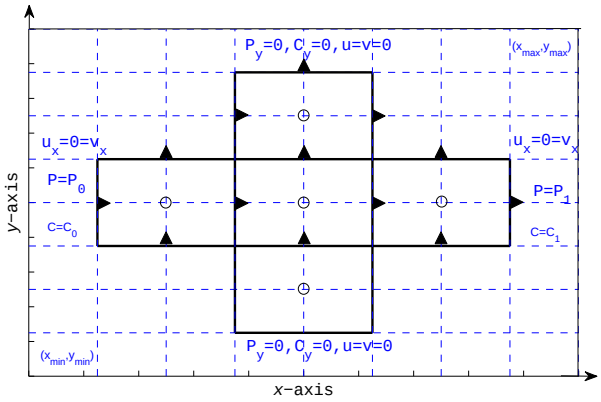

(a) $l = 0$

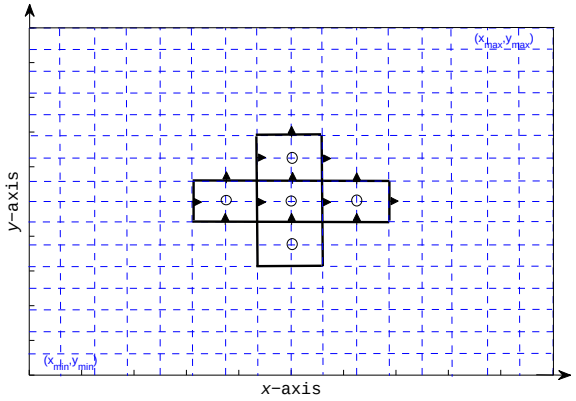

(b) $l = 1$

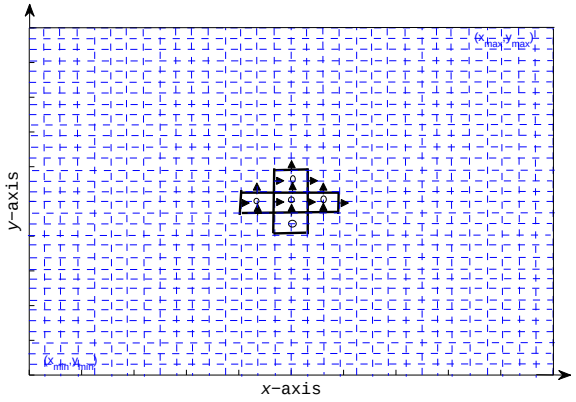

(c) $l = 2$

Figure 3.1: An example of 2D multilevel grids at levels, $l = 0$, 1, 2. The intersections of the dashed lines represent grid points, where velocity and pressure are collocated. A staggered arrangement has been demonstrated at each level. To show clearly, the boundary conditions are presented symbolically only in figure (a), where suffix with variables denote the derivative with respect to that variables.

at 4 corners of each cell, but the present approach solves for velocity on each grid point, where the staggered arrangement satisfies conservation of mass.

In this thesis, uniformly refined multilevel grids are considered, and a second order accurate finite difference method has been applied to approximate all spatial derivatives, unless otherwise stated. For the simplicity of presentation, we have used one-dimensional notation. More specifically, the numerical derivatives of $u(x)$ at i-th grid point of $\mathcal{G}_x^l$ may be denoted by $\frac{\partial u}{\partial x}\big|_i$ and $\frac{\partial^2 u}{\partial x^2}\Big|_i$, respectively, for first and second order derivatives with respect to x. In the rest of this thesis, we will use u_i^n to denote the evaluation of a time dependent quantity, $u(x,t)$, on the i-th location of the grid $\mathcal{G}_x^l$ at n-th time step; *i.e.* $u_i^n = u(x_i^l, n\Delta t)$. Two-dimensional notations are equivalent.

3.1.3 Temporal evolution on multilevel grids

A principal challenge of resolving a fine scale flow is that if the grid is refined by a factor of two, the time step Δt must be refined by at least a factor of four when explicit Euler method is used for the viscous term (Pletcher *et al.*, 2013). To address this challenge, we have adopted an implicit second order Crank-Nicolson method for the treatment of viscous/diffusion terms. All other terms have been treated explicitly. Note, the nonlinear advection term has been discretized with a second order scheme instead of the classical upwind method.

The principal motivation, as studied by Alam & Bowman (2002), of this development is to design a near optimal computational methodology so that the physics of the flow is resolved sufficiently accurately. The explicit-implicit scheme adopted in this work resides at the wake behind capturing the physics of the flow more accurately. Note, a second order accurate stable scheme implies that the local truncation error is reduced by a factor of four if the grid is refined by a factor of two. This does not

guarantee that the discrepancies on the resolved physics will be improved at the same rate. In the numerical analysis, this is called global accuracy. Note that, controlling global error is an independent and challenging topic of Computational Mathematics, and is out of the scope of this thesis.

In order to present our development, it is useful to consider a one-dimensional model equation

$$\frac{\partial u}{\partial t} + u\frac{\partial u}{\partial x} = \nu\frac{\partial^2 u}{\partial x^2} - \frac{\partial P}{\partial x} + G, \quad \frac{\partial u}{\partial x} = 0, \tag{3.1}$$

where u and P are two unknown quantities, ν is a parameter, and $G(x)$ is a known source term. Note, eqn. (3.1) is considered to represent the Navier-Stokes equation, for a presentation purpose of the scheme, and does not have a full mathematical meaning. There is no independent pressure equation and pressure is coupled with the velocity field. To decouple pressure from the velocity field, we can take divergence to the eqn. (3.1). Now from (3.1), we get a pressure Poisson equation

$$\frac{\partial^2 P}{\partial x^2} = \frac{\partial}{\partial x}\left(G - u\frac{\partial u}{\partial x}\right).$$

The forward in time and centered in space scheme can be presented considering only the advection part of eqn. (3.1).

3.1.3.1 Explicit scheme for the advection term

The following scheme,

$$\frac{u_i^{n+1} - u_i^n}{\Delta t} + u_i^n\left(\frac{u_{i+1}^n - u_{i-1}^n}{2\Delta x}\right) = 0, \tag{3.2}$$

is explicit because we can evaluate u_i^{n+1} directly from (3.2) using the known values of u_{i-1}^n, u_i^n, and u_{i+1}^n. In other words, the solution at the present time step explicitly predicts the solution at the next time step. The leading order error term of the scheme (3.2) is $(-\frac{u^2\Delta t}{2})\frac{\partial^2 u}{\partial x^2}$, which is the second order derivative with a negative coefficient.

Thus, the scheme (3.2) is unconditionally unstable (Pletcher *et al.*, 2013; Chung, 2010) for solving a pure advection equation. However, the viscous term in (3.1) balances the artificial diffusion occurred by the leading order error, thereby making the scheme conditionally stable. The condition of stability is $(\nu - \frac{u^2\Delta t}{2}) > 0$ *i.e.* $\Delta t < \frac{2\nu}{u^2}$.

3.1.3.2 Implicit scheme for the viscous term

The Crank-Nicolson method is a second order in both time and space, and is implicit, which can be written for the viscous term of eqn.(3.1); *i.e.*

$$\frac{u_i^{n+1} - u_i^n}{\Delta t} = \frac{\nu[(u_{i+1}^{n+1} - 2u_i^{n+1} + u_{i-1}^{n+1}) + (u_{i+1}^n - 2u_i^n + u_{i-1}^n)]}{2(\Delta x)^2}, \tag{3.3}$$

where $0 \leq i \leq 2^{-l}$ for a fixed l. This method requires the solution of the linear system

$$\frac{u_i^{n+1}}{\Delta t} - \frac{\nu(u_{i+1}^{n+1} - 2u_i^{n+1} + u_{i-1}^{n+1})}{2(\Delta x)^2} = \frac{u_i^n}{\Delta t} + \frac{(u_{i+1}^n - 2u_i^n + u_{i-1}^n)}{2(\Delta x)^2}.$$

The implicit scheme (3.3) is unconditionally stable (Pletcher *et al.*, 2013), and has a leading order truncation error, $\mathcal{O}((\Delta t)^2, (\Delta x)^2)$. When the scheme (3.3) is extended in a 2D grid, the multilevel solution method optimizes the computational cost.

3.2 Combined explicit and implicit scheme

Applying an explicit scheme for advection terms and an implicit scheme for diffusion terms, and an explicit scheme for the pressure and the other external force terms of the eqn.(3.1), the discretized form of the eqn.(3.1) yields

$$\begin{aligned}\frac{u_i^{n+1} - u_i^n}{\Delta t} + u_i^n \left(\frac{u_{i+1}^n - u_{i-1}^n}{2\Delta x}\right) = &\frac{\nu}{2(\Delta x)^2}(u_{i+1}^{n+1} - 2u_i^{n+1} + u_{i-1}^{n+1}) \\ &+ \frac{\nu}{2(\Delta x)^2}(u_{i+1}^n - 2u_i^n + u_{i-1}^n) \\ &+ \left(\frac{P_{i+1}^n - P_{i-1}^n}{2\Delta x}\right) + G_i^n. \end{aligned} \tag{3.4}$$

Using $\gamma = \frac{\nu \Delta t}{2(\Delta x)^2}$, the eqn.(3.4) can be re-written as

$$\begin{aligned} -\gamma u_{i+1}^{n+1} + (1+2\gamma)u_i^{n+1} - \gamma u_{i-1}^{n+1} = \gamma u_{i+1}^n + (1-2\gamma)u_i^n + \gamma u_{i-1}^n \\ - \frac{\Delta t}{2\Delta x} u_i^n \left(u_{i+1}^n - u_{i-1}^n\right) \\ + \frac{\Delta t}{2\Delta x}\left(P_{i+1}^n - P_{i-1}^n\right) + \Delta t G_i^n, \end{aligned} \tag{3.5}$$

which has the following symbolic form

$$\mathcal{L}u = f. \tag{3.6}$$

Note, $\mathcal{L}$ denotes the discretization operator, u denotes the discrete solution vector, and f denotes the discrete right hand side vector. The eqn.(3.6) expresses a system of linear algebraic equations, where the right hand side is a known quantity. For the present model, in order to approximate the solution of the PDE (3.1), the system of algebraic eqn. (3.6) needs to be solved at each time step.

The pressure variable, P_i^n, has been incorporated in the right hand side of (3.6), which is obtained from the following equation. For the discrete pressure equation

$$\left.\frac{\partial^2 P}{\partial x^2}\right|_i^n = \left.\frac{\partial}{\partial x}\left(G - u\frac{\partial u}{\partial x}\right)\right|_i^n, \tag{3.7}$$

the i-th grid point is the center of the central cell in the staggered grid as shown in Fig 3.1, where the discretization stencil corresponds to the velocity and pressure points as demonstrated in Fig 3.1. According to a brief literature review, Chorin (1968) developed a method often termed as projection method or the method of fractional steps for solving the Navier-Stokes equations of incompressible flow. In this method a collocated or nonstaggered grid was used. We employ a staggered grid between the pressure and velocity similar to the MAC method of Harlow & Welch (1965) so that we can easily implement a multilevel methodology. In other words, the pressure and velocity are staggered with respect to a staggered virtual cell on the

collocated computation grid. Note that the rotational form of the advection term is more accurate for conserving mass with the present multilevel algorithm. This is an important contribution of this thesis. The results are verified in Chapter five. Finally, the benefits of the multilevel method have been examined for miscible flow in a porous medium.

3.3 Semi-discrete form of the model equation

In order to simplify the notation, let us present the above discretization for the momentum equation (2.20) in the semi-discrete form

$$\overbrace{\left(I - \frac{\alpha\Delta t}{2Re}\nabla^2\right)\boldsymbol{u}^{n+1}}^{\mathcal{L}u} = \underbrace{\left(I + \frac{\alpha\Delta t}{2Re}\nabla^2\right)\boldsymbol{u}^{n} + \Delta t S^n}_{f}, \tag{3.8}$$

where

$$S^n = -\nabla P^n - \boldsymbol{u}^n \cdot \nabla \boldsymbol{u}^n + \boldsymbol{F}^n,$$

and other symbols are defined in the Chapter two.

Taking divergence of the eqn.(2.20) leads to the pressure equation

$$\nabla^2 P^n = \nabla \cdot \left(\boldsymbol{F}^n - \boldsymbol{u}^n \cdot \nabla \boldsymbol{u}^n\right), \tag{3.9}$$

at each time step, which replaces the incompressibility condition, $\nabla \cdot \boldsymbol{u}^n = 0$ in the numerical model.

After spatial discretization with a center in space finite difference method, eqns.(3.8, 3.9) take the form of a linear system of equations; *i.e.*

$$\mathcal{L}u = f. \tag{3.10}$$

and

$$\mathcal{L}^{\nabla} P = h, \tag{3.11}$$

where $\mathcal{L}$ and $\mathcal{L}^{\nabla}$ denote spatial discretization operators for the momentum and pressure equations (3.8, 3.9), respectively.

Note, choosing a solution methodology for these linear systems (3.10, 3.11), it is a vital point so that one can get a desired result with a minimum computational complexity.

3.4 Computational difficulties in mass transport equation

The concentration equation represents mass transport phenomena of fluid flows, also this equation is an advection dominant equation; *i.e.* advection is the dominant mechanisms compared to the diffusion. If one uses the scheme (3.2) for the advection terms and (3.3) for diffusion terms to solve the concentration equation, then a numerical artifact in the form of negative diffusion occurs. As a result, the scheme becomes conditionally stable with the condition $(D - \frac{1}{2}|u|^2\Delta t) > 0$, where D is the diffusion coefficient (Pletcher *et al.*, 2013). We need extra care to discretize the concentration equation. Thus, for a stable solution, the time step, Δt, must be smaller than $\frac{2D}{|u|^2}$. Since the diffusion coefficient, D, is typically $\mathcal{O}(10^{-5})$ for most of the fluids, such as CO_2 (Cussler, 1997), an extremely small Δt, is needed. Thus, this scheme will require a significant amount of computational cost. However, if one uses an implicit scheme for the advection and the diffusion terms of the concentration equation, then the scheme will produce a nonlinear system of equations, which also requires an additional difficulty in handling these issues. Thus, we need a more sophisticated method with greater capability to overcome these issues. A well-known treatment to address the difficulties encountered is the upwind scheme that is commonly used by

scientists (Patankar, 1980). Using upwind scheme for the advection term, we get

$$\frac{u_i^{n+1} - u_i^n}{\Delta t} + u_i^n \left(\frac{u_i^n - u_{i-1}^n}{\Delta x} \right) = 0. \tag{3.12}$$

According to the von-Neumann stability analysis this scheme is conditionally stable with the condition, $0 \leq |\frac{u\Delta t}{\Delta x}| \leq 1$ (Courant *et al.*, 1928). In spite of, conditional stability, the upwind scheme introduces numerical diffusion *i.e.* numerical solution will deviate from analytical solution after long time simulations (Pletcher *et al.*, 2013; Fletcher, 1990). Since flows in porous media are low speed flow, integration time is long.

Under this theoretical discussion, the numerical diffusion in Eulerian frame is a scientific challenge when one studies a mass transport problem. A Lagrangian method has been developed (which will be described in next chapter) to handle this numerical diffusion successfully. We will employ this Lagrangian method for the advection part of the concentration equation, where advection and diffusion terms have been treated using an operator splitting method (Holden, 2010). For comparison with the Lagrangian method, the advection part is discretized using an upwind method on an Eulerian reference. The diffusion term of the concentration equation is discretized with Crank-Nicolson scheme. Using the aforementioned schemes the discretized form of the concentration equation (2.21) in Eulerian reference yields

$$\left(I - \frac{\Delta t}{2ReSc} \nabla^2 \right) C^{n+1} = \left(I + \frac{\Delta t}{2ReSc} \nabla^2 \right) C^n + \Delta t S^n \tag{3.13}$$

with $S^n = -\boldsymbol{u}^n \cdot \nabla C^n$. Eqn.(3.13) can be expressed as

$$\mathcal{L}u = f. \tag{3.14}$$

Each of the discrete eqns.(3.8) and (3.13) leads to a large system of linear algebraic equations. Depending upon the size of the problem, most of the computation time

may be spent behind solving this system of equations. For instance, about 80% to 90% of the total simulation time goes into solving a linear system of equations for a petroleum reservoir simulator with a number of gridblocks of order $\mathcal{O}(10^5)$ (Chen *et al.*, 2006). Therefore, we need an appropriate and computationally optimal method to solve these systems of equations. We will apply a multilevel method to address this issue.

3.5 Multilevel method

An efficient technique for solving a system of linear algebraic equations is one of the main challenges currently facing most of the simulator developers in the oil industries. The oil industries also desire to get the actual picture of the fluid flow from the reservoir simulations. Unfortunately, the task is computationally very expensive. Using a direct solution method such as the Gauss elimination method for solving a system of linear equations, the required computational cost is $\mathcal{O}(N^3)$ (Bhogeswara & Killough, 1992; Behie & Forsyth, 1983; Mekeon & Chu, 1987). Iterative methods, such as Gauss-Seidel method, converge very slowly for a large system of linear equations, and convergence rate depends on the number of grid points. A multigrid method is efficient to handle this issue. Fedorenko (1962, 1964) first introduced the multigrid method to solve elliptic equations. After the pioneer work of Brandt (1977, 1972), it was possible to apply the multigrid method in fluid dynamics. The basic idea of multigrid methods is to perform the calculation on multiple grids - finer grid to coarser grid, and then interpolate solution from coarser to finer grids, in such a way that the rate of convergence is improved, and this algorithm is termed as $V-$cycle (see, for details, Pletcher *et al.*, 2013; Bhogeswara & Killough, 1992). Pletcher *et al.* (2013) showed that a standard Gauss-Seidel method for solving Laplace's equation with Dirichlet

boundary conditions required 6826 iterations for a square domain with 129×129 resolutions, whereas only 21 iterations are needed for the multigrid method. Clees & Ganzer (2007) proposed an adaptive algebraic multigrid solver strategy to solve the discrete systems of partial differential equations that arises from structured and unstructured grid models in the reservoir simulations. Bhogeswara & Killough (1992) developed a multigrid method for the simulation in porous media. They mentioned that their method is ten times faster than widely used sequential solvers on 32-processors. They also showed that the use of line corrections and line Jacobi was essential for a good convergence rate using their method. Mekeon & Chu (1987) developed a multigrid method for solving partially saturated flows in porous media. They showed that their multigrid method is about 22 times faster than the LSOR (line successive over relaxation) method in terms of CPU time. Behie & Forsyth (1983) described a multigrid technique to solve pressure equations for the oil reservoir simulations. Recently, MacLachlan *et al.* (2008) investigated the simulations of bubbly flow using a robust multilevel solver. They found that using this technique the amount of work is reduced extensively for solving the pressure-correction system. In the present study, we are using a multilevel methodology which is implemented by Alam & Bowman (2002) for the simulation of incompressible Electro-Osmotic and pressure-driven flow. The computational complexity of this V-cycle algorithm is linearly proportional to the number of grid points.

3.6 Summary

An accurate and reliable approximation method for solving model equations is a challenging issue. We use an explicit-implicit combined method to discretize the momentum equation, where pressure is calculated on a staggered grid. In addition,

implementing a staggered arrangement between velocity and pressure on a multilevel collocated grid and its verification with a miscible flow in porous media may shed further light into the computational challenges of the reservoir modeling. We use a computationally optimal multilevel method for efficiently solving algebraic system of linear equations resulting from the discetization of the model equations. A streamline based Lagrangian method has been developed which is described in the next chapter.

Chapter 4

Streamline based Lagrangian methodology

Nowadays the streamline method is getting more popularity with several research groups of computational fluid dynamics such as reservoir simulations (Thiele *et al.*, 2010; Nourozieh *et al.*, 2008; Batycky *et al.*, 1997; Thiele *et al.*, 1996), electro-osmotic flow study (Alam & Penney, 2012). Particularly, reservoir simulation groups feel more inclined to use streamline based simulators, because the streamline method offers more accurate solutions, reduced numerical dispersion compared to the traditional finite difference methods, and also it takes less CPU time for computation. Thus, it is possible to predict reservoir performance more accurately than existing finite difference method based simulators (see, Islam *et al.*, 2010; Crane & Blunt, 1999; Batycky *et al.*, 1997). The streamline method also does not have the time step restriction as finite difference methods do (Obi & Blunt, 2004). In spite of these advantages, the streamline method has some drawbacks, such as more computational cost (Thiele *et al.*, 2010) and satisfying mass conservation law.

The present streamline method has been implemented on a Lagrangian frame

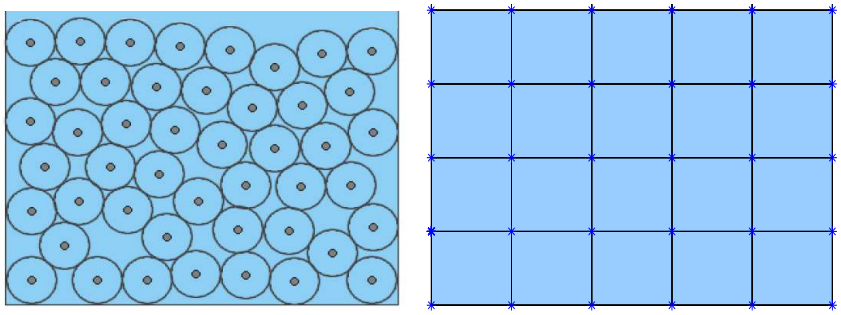

(a) (b)

Figure 4.1: Representation of the flow description. (a) Lagrangian particle-based fluid structure in 2D. The particles are represented by the dots. The circles represent the volume of each particle, (b) Eulerian grid-based fluid structure in 2D. The fluid properties such as velocity and pressure are represented by '$*$' on the discrete grid points.

work. Note, there are two fundamental approaches to describe fluid flow. One is a grid-based method which is known as the Eulerian method (*i.e.* finite difference methods), and the other one is a particle-based method, known as the Lagrangian method (Kundu *et al.*, 2012).

4.1 Description of fluid motion

To study the fluid motion in a Lagrangian frame, the individual fluid particles are tracked. On the other hand, in an Eulerian frame a control volume is defined, in which fluid flow properties of interest are expressed as fields (Kundu *et al.*, 2012).

Let us briefly explain the Lagrangian description of fluid flow. Consider any property of fluid, Ψ, for example the concentration or temperature. Then, we can describe Ψ as $\Psi(\boldsymbol{x}, t)$, where $\boldsymbol{x}$ is the position and t is time, that is know the property

of flow at each location and time, but we do not know which fluid particle occupies that position at that time. If each particle is given an identity, and with this identity the fluid particle can be identified at all subsequent times, then we can keep track of individual fluid particles along their flow paths. Suppose we mark the position $\boldsymbol{x}_k$ of the k^{th} fluid particle at some initial instant, $t = t_0$, then each fluid particle changes its position as they move but the identity will remain fixed. The flow description in this manner is known as the Lagrangian approach. In contrast, in the Eulerian description, fluid properties are prescribed on the discrete grid points of the flow domain (see, for detail, Kundu *et al.*, 2012). The Lagrangian and Eulerian description of fluid flows is depicted schematically in the Figs 4.1(a) and 4.1(b), respectively. In Fig 4.1(a) the fluid particles are denoted by small circles and the particles are tagged with the fluid properties. In Fig 4.1(b), the fluid properties are denoted by '$*$' on the discrete grid points. In some specific fields of fluid flow, such as flow in porous media, heat island circulation or weather modeling, some obstacles exist along the flow or flow domain. These types of study may not be appropriate with the Eulerian description because some grid points may be on the obstacles where fluid properties such as velocity will be zero. Note that fluid flow is a continuum phenomenon, so infinite numbers of fluid particles exist, thus it is difficult to apply the streamline based Lagrangian method to study fluid flow. The main idea of this method is to study the flow of fluid along the streamlines without discretizing the advective derivative. Here we develop a streamline based Lagrangian method.

4.2 Lagrangian algorithm

Traditional finite difference methods have some sort of difficulties while studying mass transport problems (Pletcher *et al.*, 2013). These difficulties include artificial mass

diffusion, artificial oscillations, time step limitations to satisfy stability condition, and grid orientation effects (Obi & Blunt, 2004; Chen *et al.*, 2006). In the Eulerian description of flows, the fluid properties are stored on the gird points and after any time step all the fluid particles may not reach the grid points. Then the accuracy of storing fluid properties on the grid points is questionable. In Fig 4.2 we see that, all the streamlines do not reach the grid points. An appropriate streamline based Lagrangian method may apply to address these issues. Here we extend the streamline based Lagrangian method developed by Alam & Penney (2012).

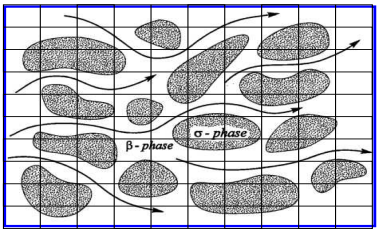

Figure 4.2: Schematic diagram shows fluid flow through porous media. The dark spaces with irregular shapes are solid bodies (sands or rocks). The curves with arrow represent the streamlines of fluid flow. The vertical and horizontal solid lines represent the grid lines in Eulerian frame.

4.2.1 Mathematical formulation of the streamline based Lagrangian method

A streamline is a continuous line within a fluid which is tangent to the velocity field at each instant. The streamlines in a flow do not intersect each other, because a fluid particle does not have two different velocities at the same point at the same instant. Therefore, any particle of fluid starting on one streamline must stay on the same streamline throughout the fluid flow (Kundu *et al.*, 2012).

Let us consider an elementary length of a streamline to be dS, and the streamline is tangent to the local velocity vector, then the mathematical form of the streamlines can be expressed as

$$\frac{ds_1}{u} = \frac{ds_2}{v}, \tag{4.1}$$

where the velocity field, $\boldsymbol{u} = (u, v)$, and the streamlines as $\boldsymbol{S} = (s_1, s_2)$, where s_1 and s_2 are streamline position along the x-axis and y-axis, respectively. The streamlines $\boldsymbol{S}$ can be parametrized as $\boldsymbol{S}(\xi) = (s_1(\xi), s_2(\xi))$ such that

$$\boldsymbol{u} = \frac{d\boldsymbol{S}}{d\xi}. \tag{4.2}$$

Since the velocity field is tangent to the streamlines, thus the velocity can be found by taking the directional derivative of any streamline, $\boldsymbol{S}$, in the direction of the velocity field, $\boldsymbol{u}$, such that $\boldsymbol{u} = \boldsymbol{u} \cdot \nabla \boldsymbol{S}$. Then the eqn.(4.2) leads to

$$\frac{d}{d\xi} = \boldsymbol{u} \cdot \nabla. \tag{4.3}$$

Now applying the operator expressed in eqn.(4.3) to the advection part of the eqn.(2.18) of chapter two, we get

$$\frac{dC}{dt} + \frac{dC}{d\xi} = 0. \tag{4.4}$$

Thus, a multidimensional advection equation becomes a one dimensional linear advection equation. The eqn.(4.4) can be solved analytically. The unique solution of eqn.(4.4) can be obtained with an initial condition $C = C_0(\boldsymbol{S}(\xi, 0))$ as $C(\boldsymbol{S}(\xi, t)) = C^n(\boldsymbol{S}(\xi - t))$.

Therefore, after the first fraction of time, we can compute $C(x, t)$ such that

$$C^{n+\frac{1}{2}}(\boldsymbol{S}(\xi), \Delta t) = C^n(\boldsymbol{S}(\xi - \Delta t)).$$

During the second fraction of time step, the solution of the diffusion part of the eqn.(2.18) will be used as an initial condition.

Note that for each value of the parameter, ξ, there will be a point on the streamlines $\boldsymbol{S}$, thus the quantity, $C(\xi, t)$ must be on a streamline. In Fig 4.2, we see that all the streamlines may not pass through the grid points. In this situation, we need to find a sophisticated way to calculate and store the fluid properties such as velocities, concentration, etc., on the grid points.

4.2.2 Calculation of concentration field and velocity field

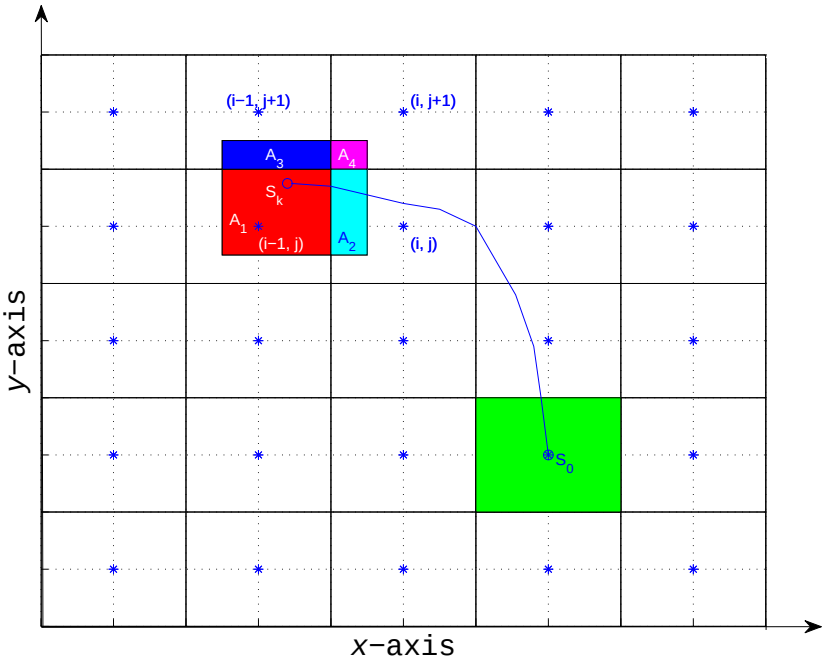

Figure 4.3: Representation of Lagrangian algorithm. Here '$*$'s represent the fluid properties on the grid points. The cell marked with 'green' color represents the initial concentration at the cell S_0. The rectangles represented by red, blue, purple and sky color express the distribution of the initial concentration.

Suppose we have total of $n_x \times n_y = K$ cells within the domain, where n_x and n_y are the number of cells along the x-axis and y-axis, respectively, and K is any integer. Also (x_i, y_j) is the position of the center of the cell (i, j), and $C_{ij}^n(\boldsymbol{x}, t)$ represents the

concentration at the cell (i, j) at time t^n with cell position (x_i, y_j). Equivalently, we can say that at the streamline position S_l , $l \epsilon K$, the concentration is $C(S_l, t^n)$, i.e., $C^n_{ij}(\boldsymbol{x}, t) = C(S_l, t^n)$. Note that we will refer to each cell as a fluid particle. Now we want to compute the concentration after one time step, i.e., $C^{n+1}_{ij}(\boldsymbol{x}, t)$, by tracing the streamline.

Let us start with any fluid particle which is marked by green color in Fig 4.3, with the streamline position at S_0. For a given velocity, let us begin by tracing a streamline from this position and suppose the streamline arrives anywhere within the cell $(i-1, j)$. The new position of the streamline is denoted by S_k, which may not be on a grid point. According to the mass conservation law, we should get the same size of fluid particle with the same concentration at the new position of the streamline, *i.e.*, at S_k. This concentration will be distributed among the neighbouring cells. A similar situation will happen to the other cells and concentration of all cells will be re-distributed. This circumstance is depicted in the Fig 4.3. Here we schematically exhibit that the initial concentration, $C(S_0, t^n)$ which is staring from the initial position of the streamline will take place in the four cells *i.e* $(i-1, j), (i, j), (i, j+1)$ and $(i-1, j+1)$ at the new streamline position, S_k after fraction of time step. The concentration, $C(S_0, t^n)$, will be distributed among these cells according to $A_1 C(S_0, t^n)$, $A_2 C(S_0, t^n)$, $A_3 C(S_0, t^n)$ and $A_4 C(S_0, t^n)$, where A_i's are portions of the area fluid particle.

Then, for the next time step, we have to trace the streamline that will again start from S_k using the velocity $\boldsymbol{u}(S_k)$ at S_k. Since S_k is not on a grid point, we can not measure $\boldsymbol{u}(S_k)$. Then we may redistribute the velocity within the neighbouring cells as in the concentration distribution. We complete this procedure by interpolating the data.

Therefore, following this procedure velocity will be updated at each time step

through streamline position, also concentration for each cell will be updated as well, as soon as streamlines have been traced at each time step. Note that the accuracy and efficiency depend on the interpolation of the velocity.

4.3 Accuracy of the velocity interpolation

We have discussed the streamline based Lagrangian method in detail in the last section. In this method, for a given velocity field on the grid points, we are tracing the streamline to compute concentration field. After one time step, the position of the traced streamlines may not be on the grid points. Thus, we can store neither the concentration field nor the velocity field on the grid points, also we will not be able to use velocity to trace next the streamline. Here we use the algorithm that is described above to interpolate the velocity field.

Infinite norm is used for the error calculation during the velocity interpolation on the grid points, and the errors of six grid levels are plotted on a log-log scale. Fig 4.4(a) depicts that the error decreases when grid size, *i. e.* Δx or Δy decreases. Also a slope fitted curve with a slope $\mathcal{O}(1)$ is fitted well. Fig 4.4(b) shows that when the number of grid points increases, then the error decreases and a linear curve fits well with the error curve. This means error is linearly decreasing with an increasing number of grid points, $\mathcal{N}$. This test confirms that the Lagrangian algorithm offers an optimal numerical technique.

4.4 Summary

We have developed a streamline based Lagrangian methodology to study mass transport phenomena in miscible fluid flow through porous media. In this methodology a

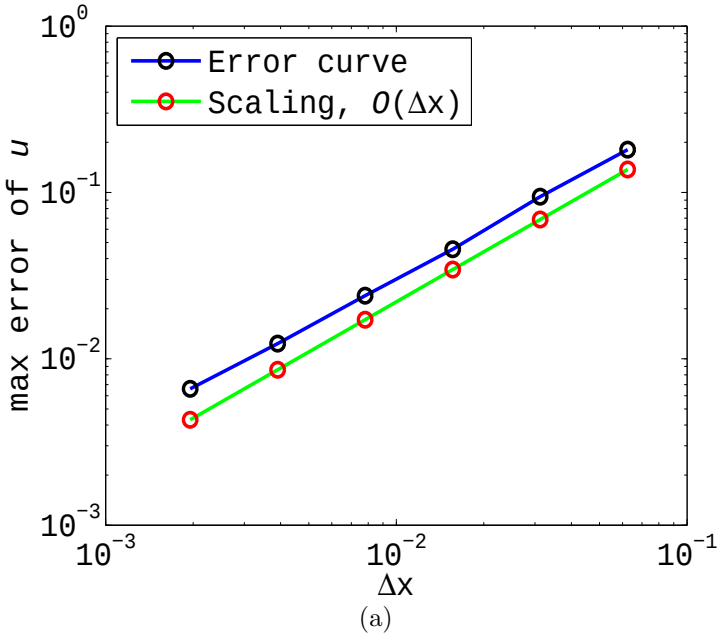

Figure 4.4: Estimation of error during velocity interpolation in Lagrangian method: (a) Error decreases linearly for finer grid size, (b) Error is inversely proportional to the number of grid points, $\mathcal{N}$.

multi-dimensional advection equation can be converted into a one dimensional equation in streamline coordinates. Furthermore, an optimal interpolation technique is used to transfer data between streamlines and Eulerian grid points. In this technique, the order of accuracy depends linearly on the number of grid points. The newly developed Lagrangian method will be able to overcome some of the drawbacks of existing numerical methods. In the next chapter, we will observe the performance of this streamline based Lagrangian method.

Chapter 5

Performance of the proposed Lagrangian method

This chapter presents the performance of the proposed Lagrangian method. A computational code is verified with a closed-form solution of two-dimensional incompressible Navier-Stokes equations. A pressure driven channel flow is studied with the Lagrangian method and compared with the Eulerian method. The newly developed method is verified with existing an exact solution of a one dimensional advection-diffusion equation.

5.1 Objective of this chapter

When a CFD model is developed, potential sources of errors have to be identified. These include mathematical modelling of the underlying physical phenomena and numerical discretization. In the Lagrangian model, we aim to simulate an advection dominated two miscible fluids flow without artificial dissipation. The verification of the proposed Lagrangian CFD model includes two sets of results. First, the numer-

ical simulation of two representative flows have been considered, for which both the velocity and the pressure can be expressed in a closed mathematical form. Note that the present model employs an Eulerian mesh for computing the velocity field. Second, a simplified mathematical model and a reference numerical model have been used to verify the Lagrangian simulation.

5.2 An incompressible flow in a doubly periodic domain

5.2.1 A brief outline of the simulation

A two-dimensional incompressible flow in a unit domain, $[0,1] \times [0,1]$, with a doubly periodic boundary condition, is a representative test case in the field of CFD modelling (e.g. Zhou *et al.*, 2003). The governing equations for this flow are given by eqns.(2.19 - 2.20) along with $\boldsymbol{F} = 0$. We can derive a closed-form solution for u, v and P of the eqn.(2.20) for $\boldsymbol{F} = 0$, which is given by (e.g. Zhou *et al.*, 2003)

$$u(x,y,t) = -\cos(2\pi x)\sin(2\pi y)\exp(-8\pi^2 t/Re), \tag{5.1}$$

$$v(x,y,t) = \sin(2\pi x)\cos(2\pi y)\exp(-8\pi^2 t/Re), \tag{5.2}$$

$$P(x,y,t) = -\frac{1}{4}(\cos(4\pi x) + \cos(4\pi y))\exp(-16\pi^2 t/Re). \tag{5.3}$$

The numerical resolution for the present simulation is given by $n_x \times n_y$, where $\Delta x = 1/(n_x - 1)$ and $\Delta y = 1/(n_y - 1)$. A resolution is obtained with $\Delta x = \Delta y = 3.9 \times 10^{-3}$. For this resolution a time step, $\Delta t = 5 \times 10^{-5}$, and a Reynolds number, $Re = 100$, have been adopted. Since all spatial derivatives have been approximated with a second order scheme, the adopted value of Δt is approximately $O(\Delta x^2)$. Clearly, these parameters satisfy the stability condition, $\Delta t \leq 2/Re$, discussed in chapter

three. The results for velocity and pressure fields are discussed in the following subsections.

5.2.2 Results for the velocity field

We have calculated the numerical solution of $\boldsymbol{u} = (u, v)$ of the eqns. (2.19 - 2.20) for which the exact solution is given by the expressions (5.1) and (5.2). In order to present a qualitative comparison, the contour plots of numerical and exact velocity fields are presented in Fig 5.1, after 2000 time steps. In this contour plot, the numerical and exact solutions for both velocity components are indistinguishable. In order to investigate a quantitative comparison between the numerical and exact solutions of the velocity fields, we have computed the profiles along the center lines for numerical solutions and those are compared with the line plots of their corresponding exact solutions. Here two representative cases are presented in Fig 5.2. One is a line plot of the u-velocity component at $x = 0.5$, *i.e.,* $u(0.5, y, 1)$, (Fig 5.2(a)), and the other one is v-velocity component at $y = 0.5$, *i.e.,* $v(x, 0.5, 1)$, (Fig 5.2(b)). From these line plots we see that the numerical and exact solutions have an excellent agreement. Next we discuss pressure field computation.

5.2.3 Results for the pressure field

We have calculated the numerical solution of $P(x, y, t)$ of the eqn. (2.20) for which the exact solution is given by the expression (5.3). The contour plots of both the numerical and exact solutions of the pressure field are exhibited in Fig 5.3. In these contour plots, the numerical and exact solutions are nearly indistinguishable. For a quantitative investigation we have calculated a number of line plots of the pressure field (for both the numerical and exact) at various position of the domain to investigate the

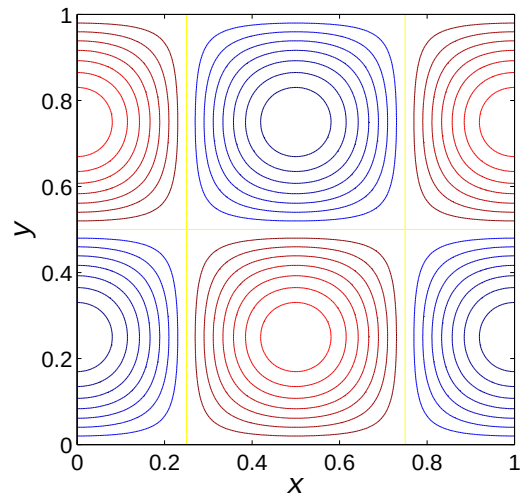

Exact solutions, $u(x, y, 1)$

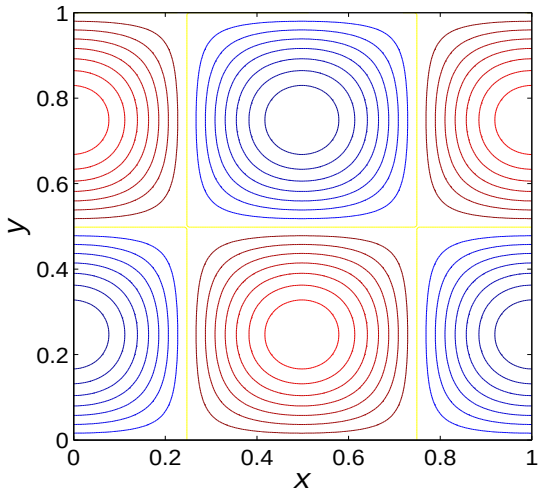

Numerical solutions, $u(x, y, 1)$

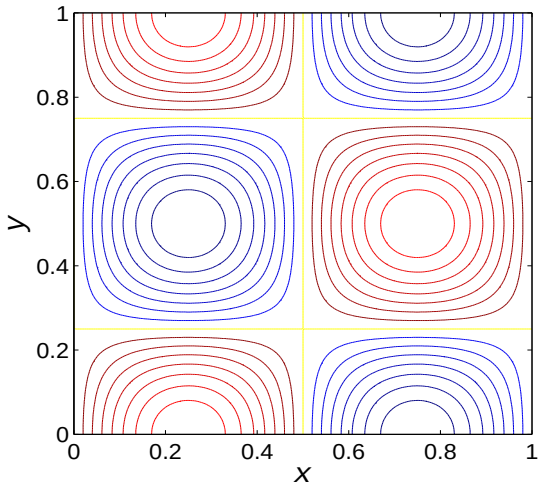

Exact solutions, $v(x, y, 1)$

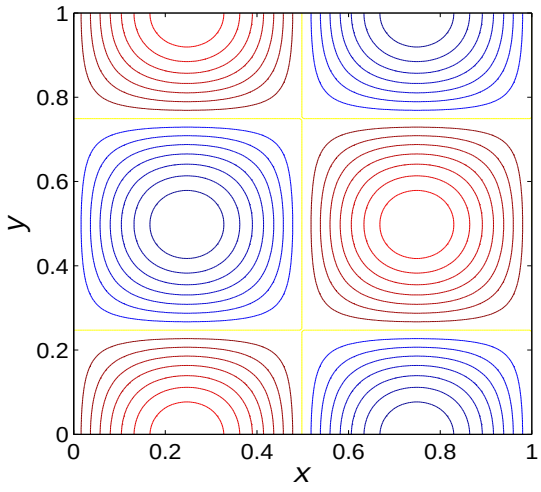

Numerical solutions, $v(x, y, 1)$

Figure 5.1: Comparison of the exact and numerical results of both velocity components $u(x, y, t)$ and $v(x, y, t)$ at $t = 1$.

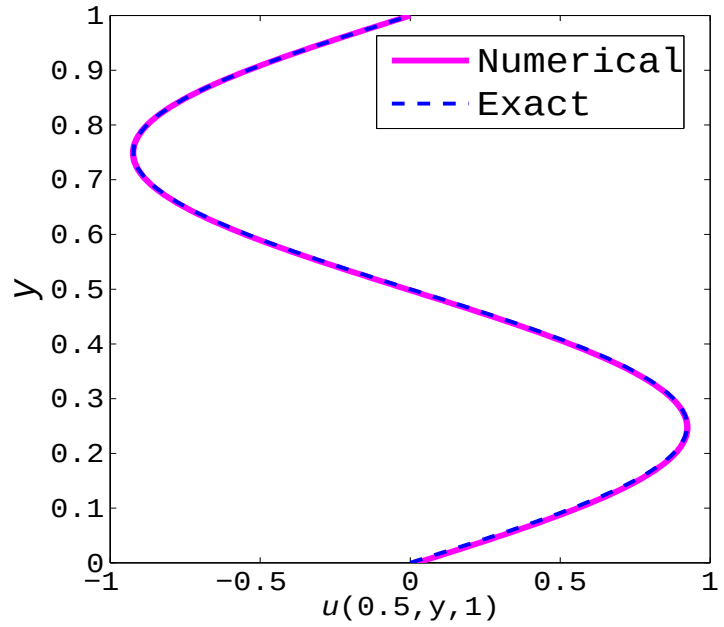

(a)

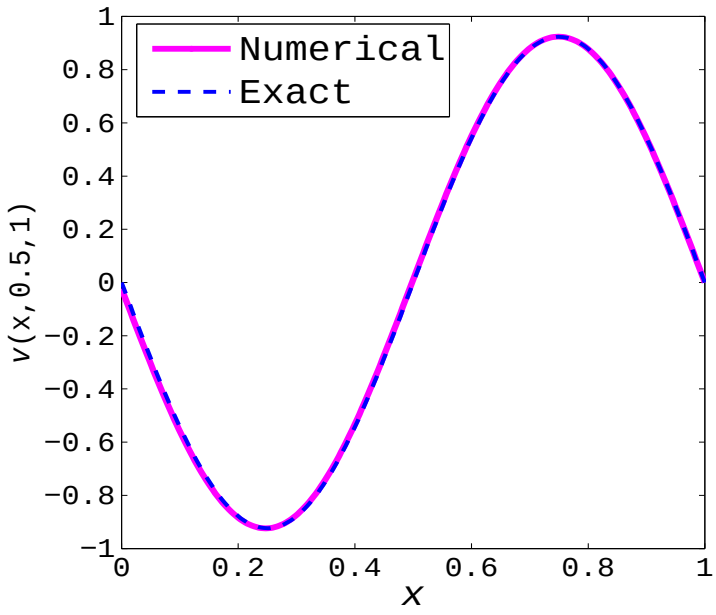

(b)

Figure 5.2: Velocity profiles along the center line: (a) $u(0.5, y, 1)$ along the line $x = 0.5$ and (b) $v(x, 0.5, 1)$ along the line $y = 0.5$.

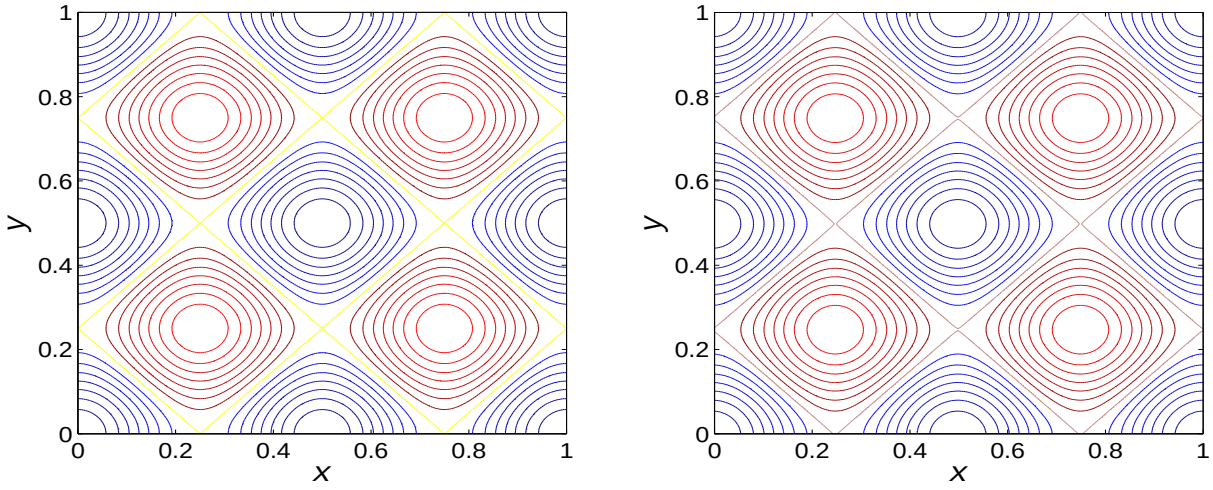

Exact pressure field, $P(x, y, 1)$ Numerical pressure field, $P(x, y, 1)$

Figure 5.3: Comparison of the exact and numerical pressure fields, $P(x, y, t)$ at $t = 1$.

differences between numerical and exact solutions. Among them, the line plots at $x = 0.75$ and $y = 0.75$ are presented in Fig 5.4 as representatives. We notice both the numerical and exact solutions have a good agreement except a slight deviation near the boundary.

5.3 Pressure-driven flow of two miscible fluids

5.3.1 Model description

Let us consider the flows of two miscible fluids which are driven by a constant pressure gradient. Suppose, initially, the reservoir is filled with a highly viscous fluid such as oil (resident fluid). We present a computational model to explain a phenomenon where oil is displaced by injecting a lower viscous fluid compared to oil. This injected fluid can be CO_2 which is the choice for most industrial applications for economical

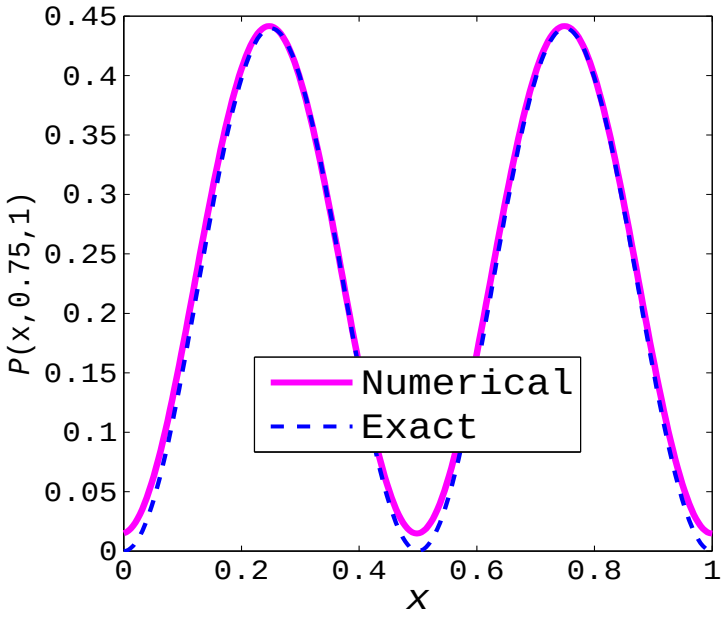

(a)

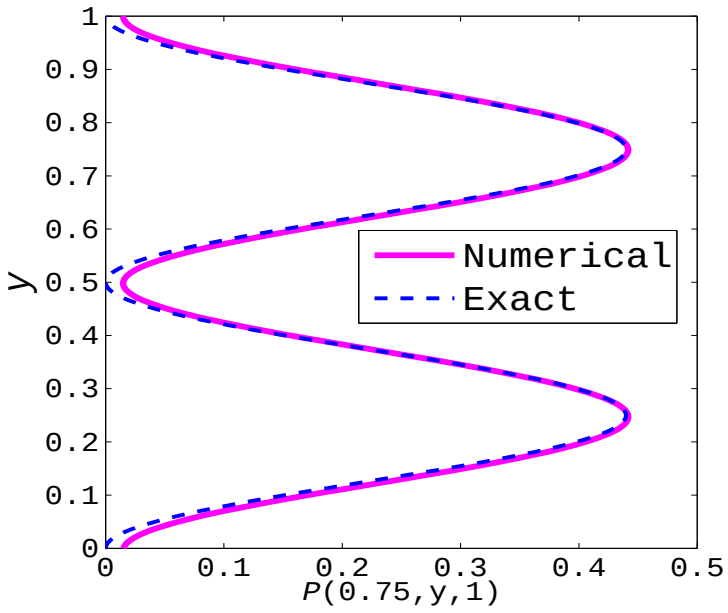

(b)

Figure 5.4: Comparison of the profiles of numerical and exact pressure field, $P(x, y, t)$ presented in Fig 5.3. The profiles are calculated along a fixed line: (a) $P(x, 0.75, 1)$ along the line $y = 0.75$, and (b) $P(0.75, y, 1)$ along the line $x = 0.75$.

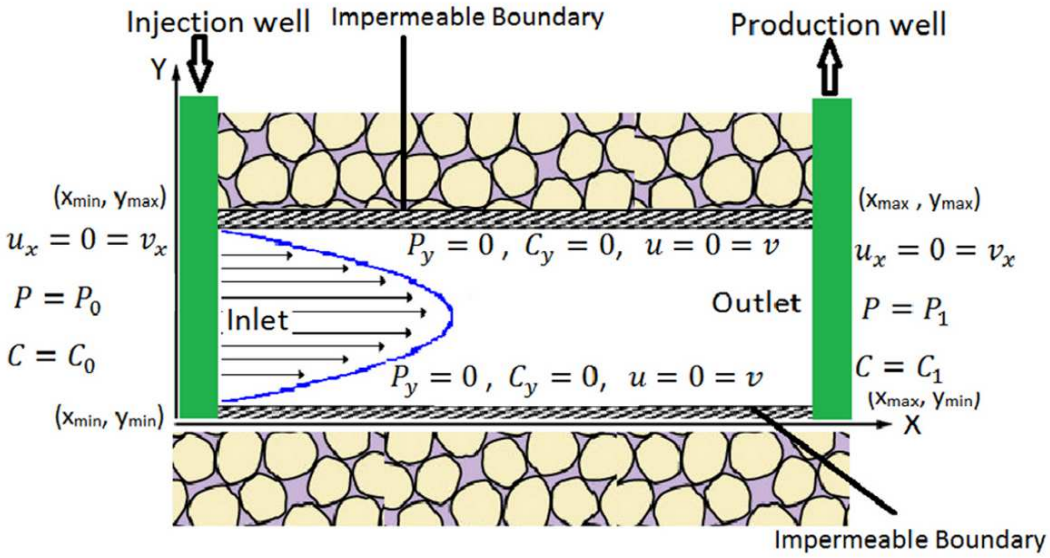

Figure 5.5: Schematic diagram of the pressure driven flow with boundary conditions.

and environmental benefit (Gozalpour *et al.*, 2005; Holtz *et al.*, 2001; Gerritsen & Durlofsky, 2005). In order to investigate the computational performance of the proposed model, let us assume a reservoir with high permeability, and the gravitational force is neglected, also the flow domain is confined between two impermeable regions as depicted schematically in Fig 5.5. Since the permeability is assumed to be high and the flow is driven by a pressure drop, thus the velocity would decrease from the highest value near the center of the reservoir, to zero near impermeable boundaries (see Fig 5.5). In order to simulate this type of flow, we consider eqns.(2.19 to 2.21) as governing equations with $\boldsymbol{F} = 0$. The necessary boundary conditions are described in chapter two, and also shown in Fig 5.5, symbolically.

We study the numerical simulations of this model using a newly developed Lagrangian method which is described in chapter four, and the Eulerian method as a numerical experiment.

5.3.2 Numerical simulations of mass transport phenomena

The mass transfer methodology analysis is studied theoretically in chapter three to understand the source of numerical mass diffusion and dispersion. We follow the performance of the Lagrangian method by comparing the simulations with the Eulerian method.

We start the simulations with 16,384 grid points for the both methods Lagrangian and Eulerian. In addition, we use time step, $\Delta t = 5 \times 10^{-2}$ for the Lagrangian method, and $\Delta t = 5 \times 10^{-4}$ for the Eulerian method to maintain numerical stability condition (CFL condition). It has been found that both methods work fine with this resolution and time step. Since we are interested in finding the solution in a finer grid, thus we are able to increase the resolution for the Lagrangian method keeping the same time step which is hundred times larger than the Eulerian method. On the other hand, if we increase the resolution in the Eulerian method, it is necessary to decrease the time step to maintain the stability condition which leads to more computational cost. Therefore, in the present simulations, we use 65,536 grid points in the Lagrangian method and 16,384 grid points in the Eulerian method. Note that in all relevant simulated figures throughout the thesis from here, yellow represents resident fluids, such as oil, and red represents interface of the miscible zone of the concentration field after injection of another fluid like CO_2.

Viscosity has an important role in the EOR process from production to transportation (Homayuni *et al.*, 2011). We consider two types of simulations: one for the flow at a low Reynolds number, *i.e.*, $Re = 1$, and other one for the flow at a high Reynolds number, *i.e.*, $Re = 100$. Note, $Re = 1$ means the viscous force is balanced by the inertia force and $Re = 100$ means viscosity is reduced by a factor of 100.

Parameters	Lagrangian	Eulerian
$L_x \times L_y$	3×1	3×1
$n_x \times n_y$	512×128	256×64
Δt	5×10^{-2}	5×10^{-4}
∇P	2	2
Re	1	1

Table 5.1: List of parameters for corresponding Fig 5.6.

5.3.2.1 Numerical simulations when viscosity is high

First, we study the simulations of a mass transport phenomena for $Re = 1$. Fig 5.6 depicts the mass transport phenomena of the concentration for the various values of $ReSc$. Here, we clearly follow a visual comparison between the left and the right columns in Fig 5.6 that exhibits that the Eulerian method has been plagued with the numerical artifact of mass dispersion. The streamline based Lagrangian method is able to minimize the impact of numerical dispersion. The mass dispersion is significantly reduces when the value of $ReSc$ is increasing, *i.e.*, the diffusion coefficient is decreasing. In Lagrangian method, the interface of the miscible zone of two fluids becomes steeper with increasing $ReSc$ values. On the other hand, the interface remains stretched in the Eulerian simulations compared to the Lagrangian simulations. Next we study the simulations of the fluid flows at low viscosity.

5.3.2.2 Numerical simulations when viscosity is low

Here we study the mass transport phenomena when viscosity is reduced by a factor of 100 and all other parameters remain the same as for high viscosity *i.e.* $Re = 1$. The simulations are presented in Fig 5.7. In this case, we also observe exactly the same

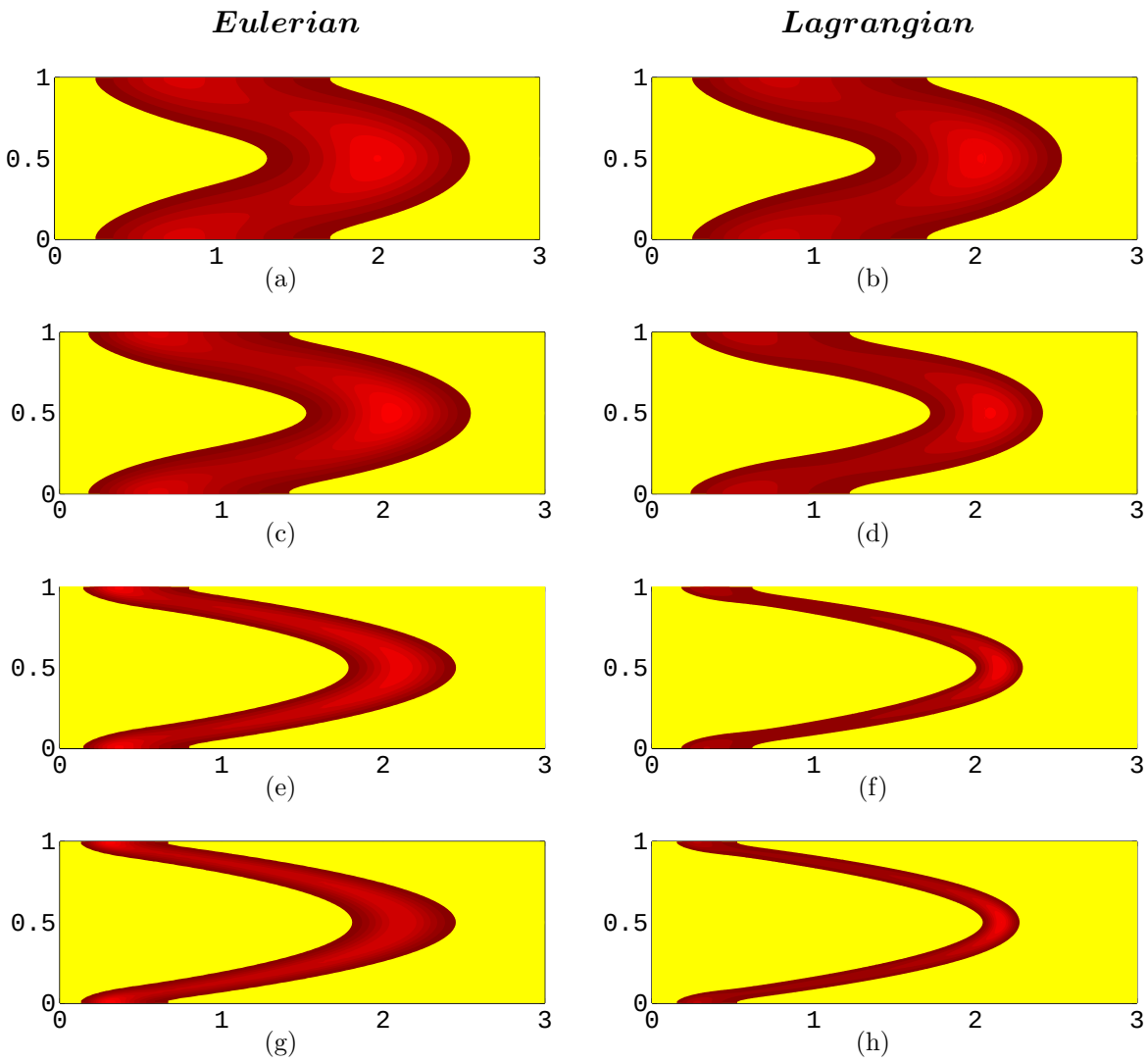

Figure 5.6: The effect $ReSc$ on the concentration field, $C(x, y, t)$, at time $t = 24.5$ for $Re = 1$. The left column of simulations is done by Eulerian method, and the right column by the proposed Lagrangian method. (a) and (b) $ReSc = 1000$, (c) and (d) $ReSc = 2000$, (e) and (f) $ReSc = 10000$, (g) and (h) $ReSc = 20000$.

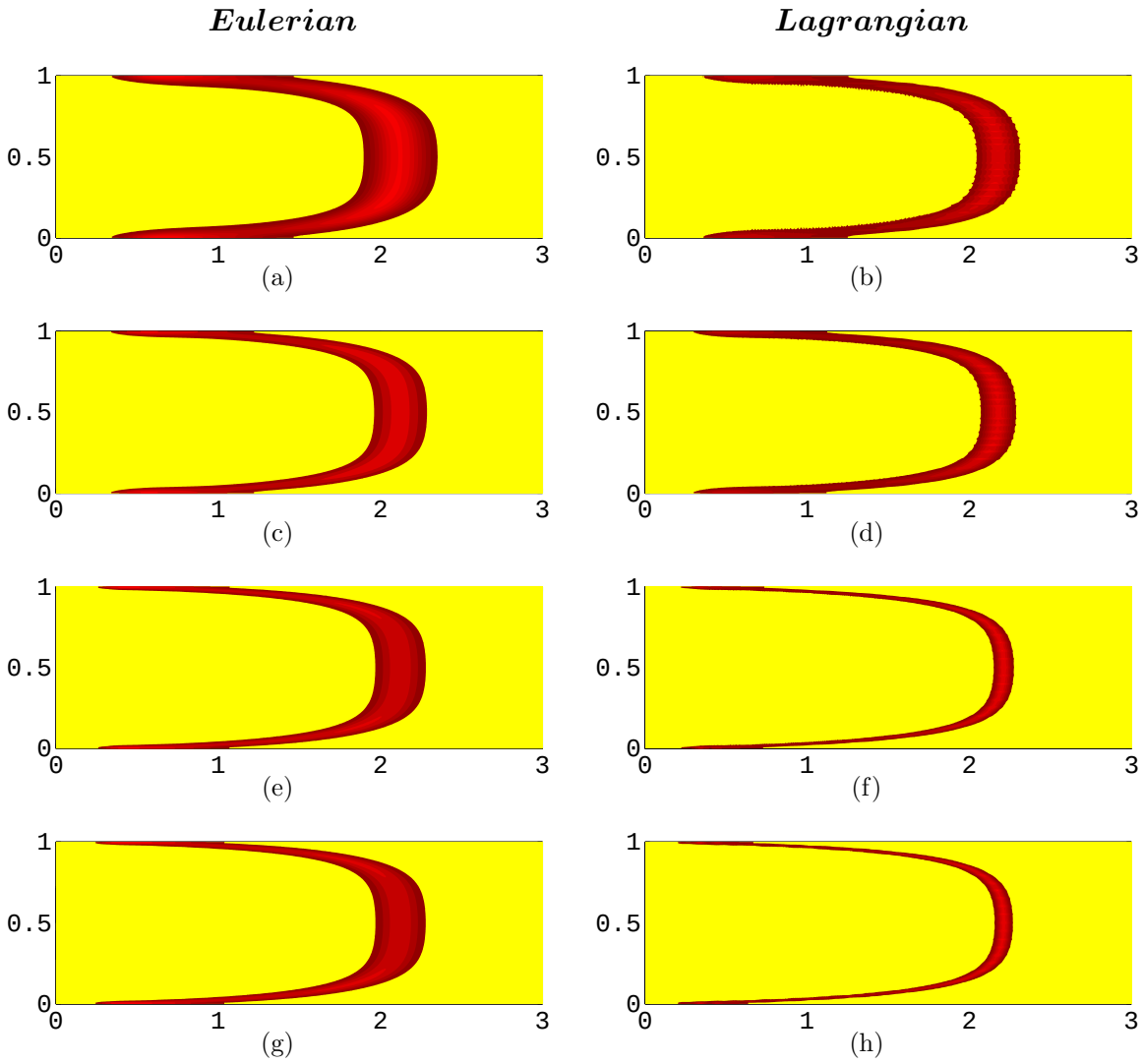

Figure 5.7: The effect $ReSc$ on the concentration field, $C(x, y, t)$ at time, $t = 2.55$ for $Re = 100$. Left column is done by Eulerian (Upwind) method, and right column by the proposed Lagrangian method. (a) and (b) $ReSc = 1000$, (c) and (d) $ReSc = 2000$, (e) and (f) $ReSc = 10000$, (g) and (h) $ReSc = 20000$.

Parameters	Lagrangian	Eulerian
$L_x \times L_y$	3×1	3×1
$n_x \times n_y$	512×128	256×64
Δt	5×10^{-2}	5×10^{-4}
∇P	2	2
Re	100	100

Table 5.2: List of parameters for corresponding Fig 5.7.

behavior of the flow that was experienced in the flow at high viscosity. This means that the Lagrangian method has no numerical artifact compared to the Eulerian method. Furthermore, we see that when viscosity is reduced, then the flow gets speeds up and the flow at $Re = 100$ is near by ten times faster than the flow at $Re = 1$. Thus, we see that viscosity has an important role in the fluid flow.

We use a grid size, $\Delta x = 3/512$, and time step, $\Delta t = 5 \times 10^{-2}$, in the Lagrangian method, whereas a grid size, $\Delta x = 3/256$, and time step, $\Delta t = 5 \times 10^{-4}$ have to be used for the Eulerian method to maintain a numerical stability condition. We observe from the simulations that the proposed streamline based Lagrangian method does not suffer from minimal numerical dispersion, and also has no limitation on time-step for numerical stability to capture small scale physics. In addition, the proposed Lagrangian method is computationally inexpensive. Note that, this method is one hundred times faster in time step and a finer resolution than the Eulerian method can be used .

5.4 A simplified two fluids model

In this section we develop a simple model so that a closed form solution can be found. It can therefore be used as a quick approximation for the flow profiles. Let us consider a particular flow of the flow configuration described in subsection 5.3.1. To make definite our mathematical formulation, we simplify the model with the following assumptions: the flow direction is along the x-axis and flow is driven by a constant external pressure gradient. Under these assumptions mass conservation eqn. (2.19) reduces to $\frac{\partial v}{\partial y} = 0$, which implies v is constant. Since $v = 0$ at $y_{\min} = 0$ and $y_{\max} = H$, thus, $v = 0$ everywhere. We also consider constant permeability and porosity is equal to one, then according to Darcy's law the mean velocity along the flow direction will be constant. The initial concentration is also invariant along the y-axis, *i.e.*, $\frac{\partial C}{\partial y} = 0$. When flow is fully developed, it becomes a steady state. Applying all these conditions to the x-momentum, y-momentum and concentration equations of the model eqns. (2.19 - 2.21) with $\boldsymbol{F} = 0$, we get,

$$0 = -\frac{1}{\rho}\frac{\partial P}{\partial x} + \nu\frac{\partial^2 u}{\partial y^2}, \tag{5.4}$$

$$0 = -\frac{1}{\rho}\frac{\partial P}{\partial y}, \tag{5.5}$$

$$\frac{\partial C}{\partial t} + u\frac{\partial C}{\partial x} = D\frac{\partial^2 C}{\partial x^2}. \tag{5.6}$$

The eqn. (5.5) implies that P is independent of y. Again in eqn. (5.4), P can be a function of x, and u can be a function of y, but to satisfy eqn. (5.4) with these two functions simultaneously, both terms must be a constant. Thus, the pressure gradient is constant along the flow direction of the reservoir. Now integrating twice with respect to y, the eqn. (5.4) yields,

$$-\frac{y^2}{2}\frac{dP}{dx} + \mu u + Ay + B = 0, \text{with } \mu = \nu\rho. \tag{5.7}$$

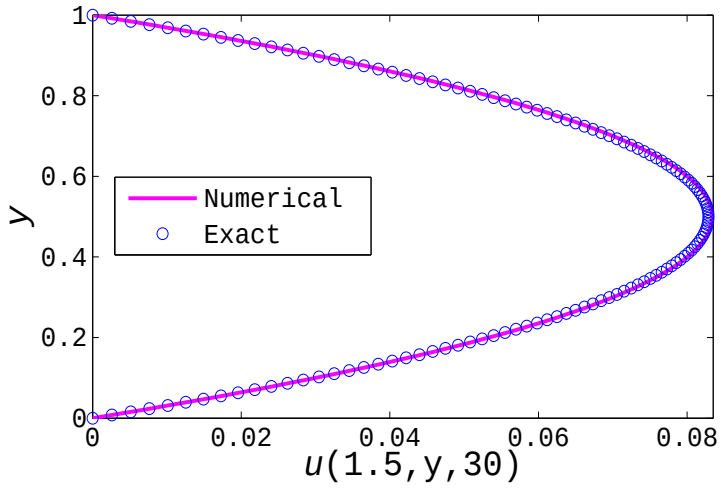

Figure 5.8: Comparison of exact velocity profile and model velocity profile at the stage of fully developed flow, when $Re = 1$.

By using the boundary conditions $u = 0$ at $y_{\min} = 0$ and $y_{\max} = H$ (H is the width of the channel) then, eqn. (5.7) becomes

$$u(y) = -\frac{1}{2\mu}\frac{dP}{dx}y(H - y). \tag{5.8}$$

The mean average velocity can be derive as

$$\tilde{u} = -\frac{H^2}{12\mu}\frac{dP}{dx}. \tag{5.9}$$

Note that the eqn. (5.8) is Poiseuille flow velocity (Kundu *et al.*, 2012).

5.4.1 Comparison of horizontal velocity profile

The velocity defined in eqn.(5.8) is considered as an exact velocity along the flow direction. The exact velocity is computed using parameter values: $\mu = 1$, $H = 1$ and $\frac{dP}{dx} = -0.66$ in eqn.(5.8) in the case of the simplified model. The numerical velocity profile is calculated when flow is fully developed. The exact and numerical velocity

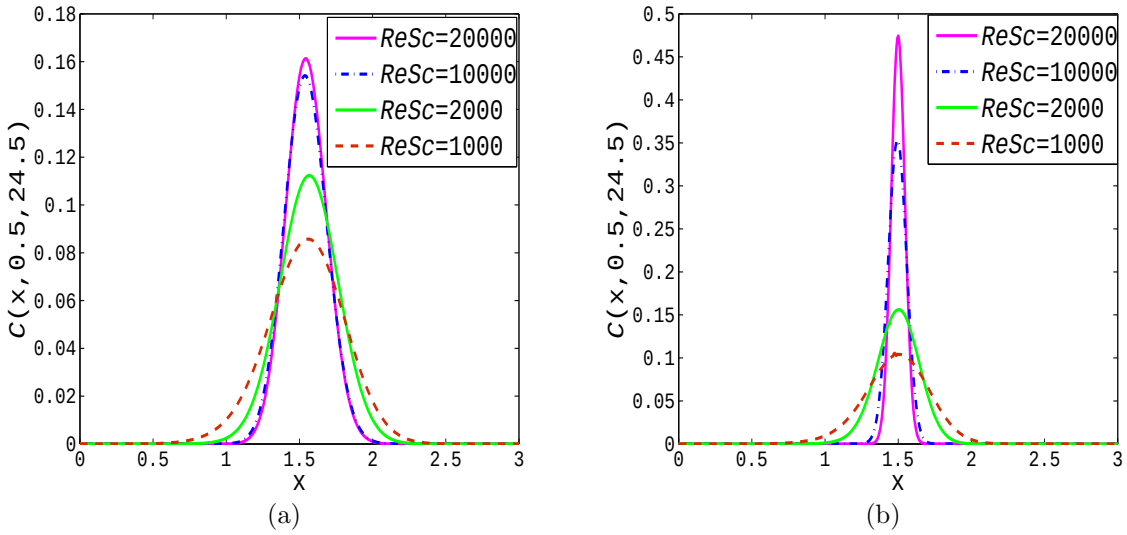

Figure 5.9: Concentration profiles, $C(x, 0.5, 24.5)$ of the simulations presented in Fig 5.6 at the center line of y-axis, for several values of $ReSc$ when $Re = 1$: (a) Eulerian method, (b) Lagrangian method.

profiles are presented in Fig 5.8. We see that the model velocity profile has a strong agreement with the exact velocity profile. This experiment was used to validate the results by many authors, such as Zhang & Prosperetti (2009) used it to validate their velocity estimation for pressure-driven flow with porous walls and Nathan & Niall (2006) used it while they were studying pressure driven flows in porous microfluidic devices.

5.4.2 Study of mass diffusion

Concentration is a fundamental quantity of interest in transportation of miscible fluid flows. The term concentration expresses the amount of mass diffusion of a substance within the mixing region. Mass diffusion is one of the important factors in such fluid flows. When miscible flow moves forward, according to the advection equation, the

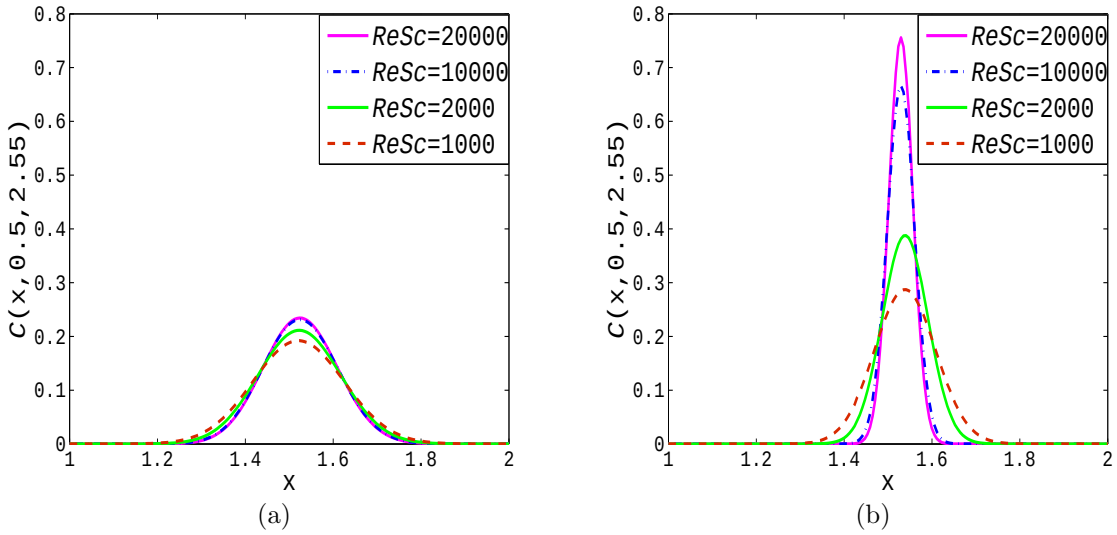

Figure 5.10: Concentration profiles, $C(x, 0.5, 2.55)$, of the simulations presented in Fig 5.7 at the center line of y-axis, for several values of $ReSc$ when $Re = 100$: (a) Eulerian method, (b) Lagrangian method.

flow faces dispersion during the progress (Udey & Spanos, 1993). We would like to examine the nature of this diffusion, and compare this between the Lagrangian and Eulerian methods. In Fig 5.6 and Fig 5.7 of the subsection 5.3.2, we have observed how the flow is experiencing numerical diffusion in both the Lagrangian and Eulerian methods. To analyze this mass diffusion, we compute a profile of the concentration field along the line $y = 0.5$ for each simulation presented in Fig 5.6 and Fig 5.7. For the Eulerian method the concentration profiles are presented in Fig 5.9(a) and Fig 5.10(a) when $Re = 1$ and $Re = 100$, respectively. Fig 5.9(b) and Fig 5.10(b) show the concentration profiles of the simulations presented in Fig 5.6 and Fig 5.7 by using the Lagrangian method for $Re = 1$ and $Re = 100$, respectively. We notice that in the Eulerian method the profiles become more smeared out. On the other hand, the profiles remain steeper in the Lagrangian method. This means that the Eulerian method has significant numerical diffusion and the diffusion is negligible

in Lagrangian method. Therefore, the newly developed Lagrangian method has the ability to eliminate the numerical mass diffusion that appears in the Eulerian method. The concentration profiles of the Lagrangian method approach very closely to the exact solution rather than spreading out, that is the Lagrangian method is free from numerical diffusion. We will compare the numerical solutions with the exact solution in the next subsection.

5.4.3 Comparing with an exact solution of one dimensional advection-diffusion equation

In this subsection, we compare a numerical solution with an exact solution of a one dimensional advection-diffusion equation (5.6). A closed form solution of advection-diffusion equation (5.6) with the initial condition, $C(x,0) = \exp(-x^2/D)$ is

$$C(x,t) = \frac{1}{\sqrt{(4Dt+1)}} \exp\Big[- \frac{(x-ut)^2}{D(4t+1)} \Big], \tag{5.10}$$

where u is the average mean velocity along the x-axis, defined in eqn.(5.9). This type of exact solution was used by Noye & Tan (1988) to validate their numerical method. Celia *et al.* (1990) used this type of solution while studying the Eulerian - Lagrangian localized adjoint method (ELLAM). Sankaranarayanan *et al.* (1998) took this type of solution to validate their model for studying the transport of conservative pollutants, and Dehghan (2004) used it to validate the method for studying numerical diffusion. We examine the numerical results with the exact solutions for two cases: one is Reynolds number, $Re = 1$ and the other one is Reynolds number, $Re = 100$.

First, we discuss the case when the Reynolds number is $Re = 1$. In Figs 5.11(a) to 5.11(d), the exact solution is plotted with the numerical solutions computed by the Lagrangian and Eulerian methods for each value of $ReSc$. The results show that the Lagrangian solutions have a good agreement with the exact solution for each

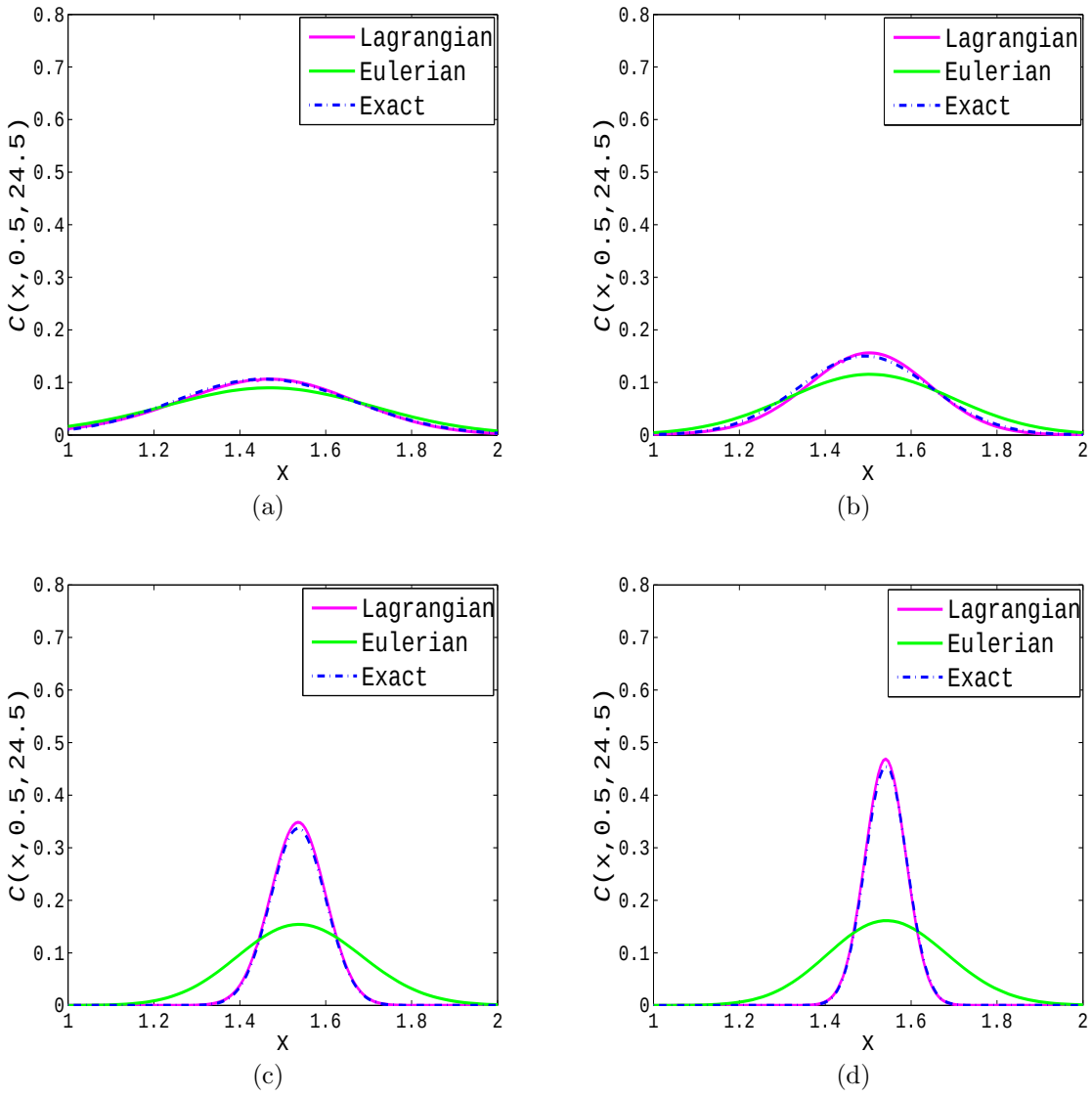

Figure 5.11: Comparison of concentration profiles of Lagrangian results with Eulerian and exact results for the simulations presented in Fig 5.6 when $Re = 1$ and various values of $ReSc$: (a) $ReSc = 1000$, (b) $ReSc = 2000$, (c) $ReSc = 10000$, (d) $ReSc = 20000$ at time $t = 24.5$.

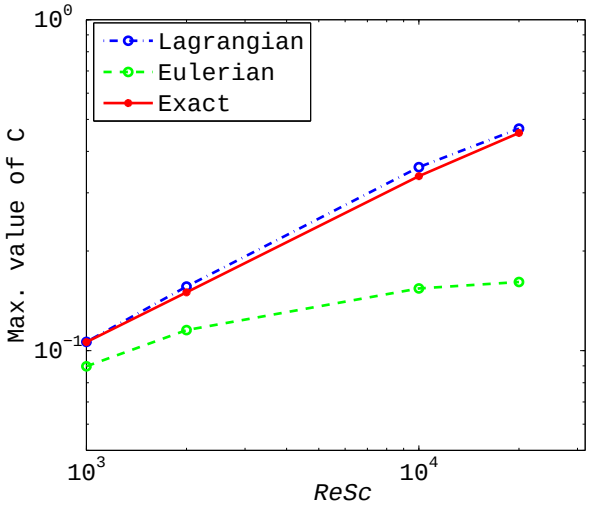

Figure 5.12: Comparison of the results of the Lagrangian method with Eulerian method, and exact solutions for the maximum concentration distribution, $C(\boldsymbol{x}, t)$ versus $ReSc$ for the corresponding results presented in Fig 5.11.

value of $ReSc$. To quantify this argument we perform the following experiment. The maximum values of each concentration distribution for the simulations presented in Fig 5.11 are calculated and compared with the exact value using a log-log plot which is displayed in Fig 5.12 when $Re = 1$. We notice that the Eulerian solutions have a significant deviation from the exact solution, whereas the Lagrangian solutions converge to the exact solution.

Second, we discuss the case when the Reynolds number, $Re = 100$. In this case, we also plot the exact solution along with numerical solutions computed by the Lagrangian and Eulerian methods for each value of $ReSc$ in Figs: 5.13(a) to 5.13(d). The Lagrangian solutions have a good agreement with the exact solution for each value of $ReSc$. We clearly notice that Eulerian results decline from the exact solution, and the declination appears more significant when the value of $ReSc$ increases,

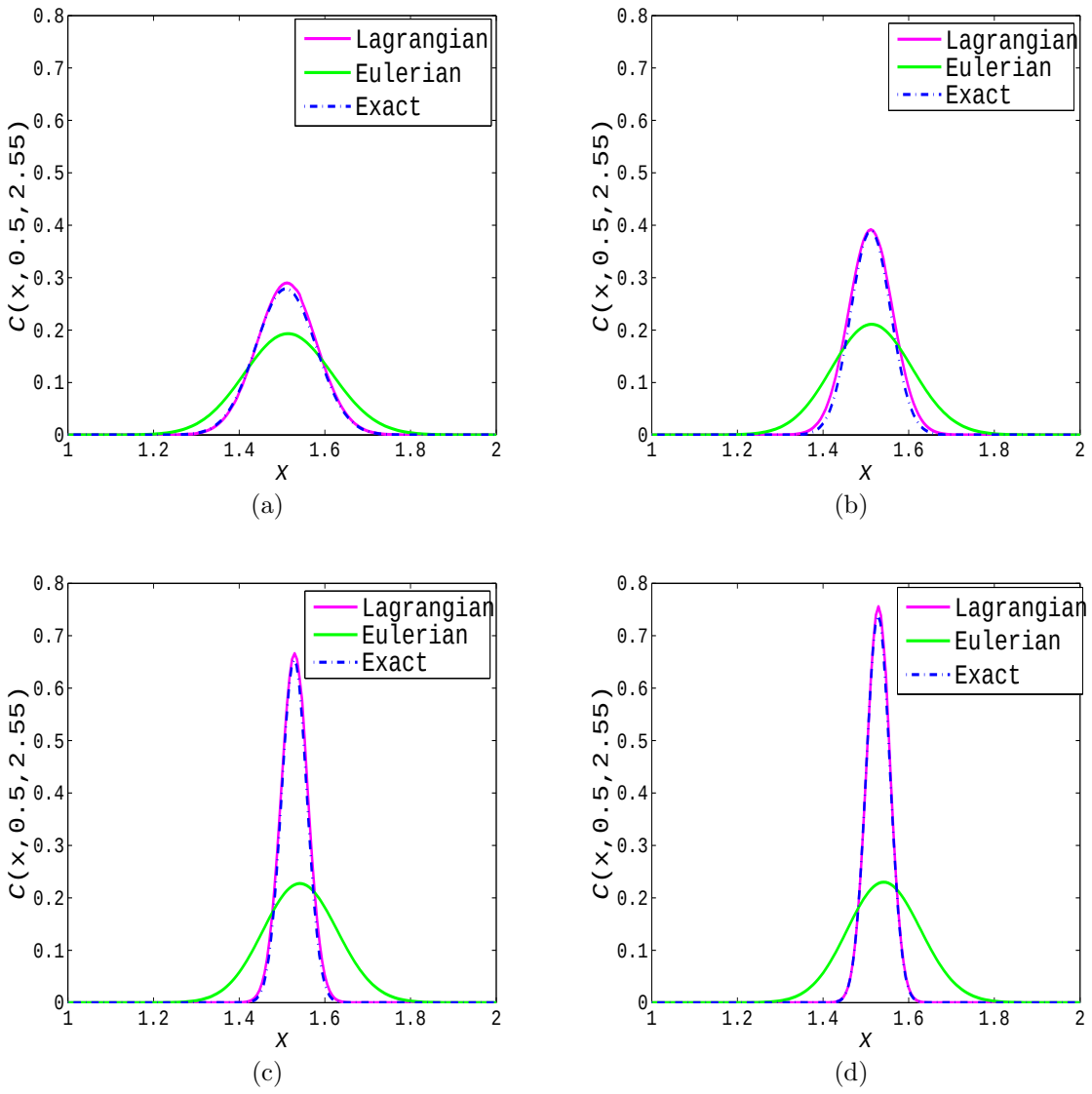

Figure 5.13: Comparison of concentration profiles of Lagrangian results with Eulerian and exact results for the simulations presented in Fig 5.7 when $Re = 100$ and various values of $ReSc$: (a) $ReSc = 1000$, (b) $ReSc = 2000$, (c) $ReSc = 10000$, (d) $ReSc = 20000$ at time $t = 2.55$.

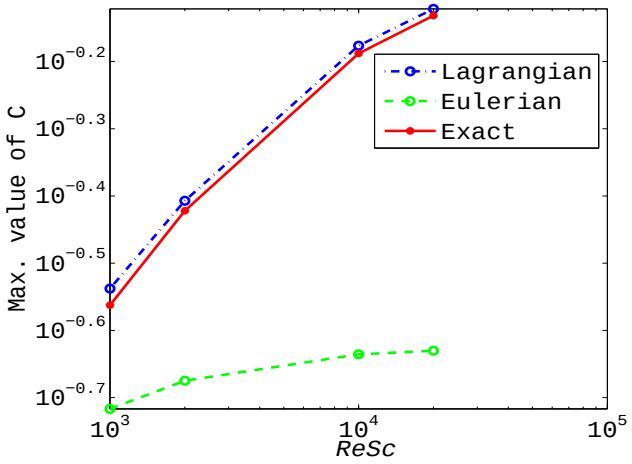

Figure 5.14: Comparison of the results of Lagrangian method with Eulerian method, and exact solutions for the maximum value of the concentration distribution, $C(\boldsymbol{x}, t)$ which are calculated from the Fig 5.13 where $ReSc = 1000, 2000, 10000$, and 20000 with $Re = 100$.

i.e., the diffusion coefficient of the concentration field decreases. To quantify this argument we also perform the same experiment as we did for the $Re = 1$ case. The results are presented in Fig 5.14. We observe that the Lagrangian solutions converge to the exact solution, and the Eulerian solutions diverge from the exact solution.

5.4.4 Verification of mass conservation law

The mass conservation law states that, in an isolated system, mass is neither created nor destroyed; it might be transferred from one phase to another. Thus, in the study of fluid dynamics, it is important to verify the mass conservation law. Out of sixteen simulations presented in Fig 5.6 and Fig 5.7, we consider one simulation as a representative case with $ReSc = 20000$ and $Re = 100$ for both the Lagrangian and Eulerian methods (Figs: 5.7(g) and 5.7(h)). Note that the amount of the initial

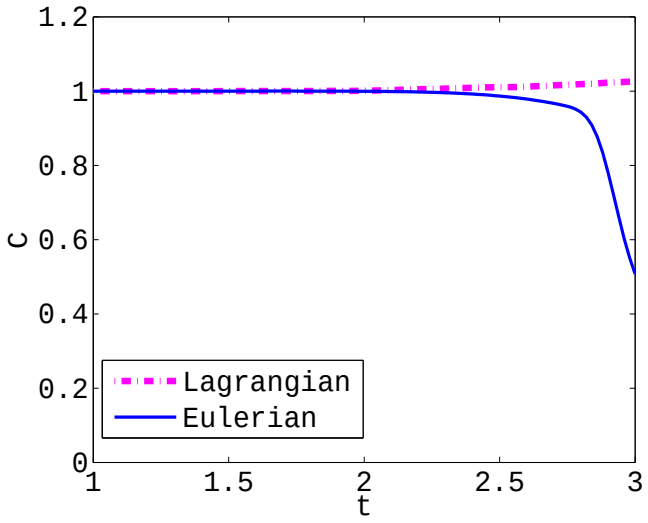

Figure 5.15: Verification of mass conservation law for the simulations produced by the Lagrangian and Eulerian methods. A representative case is considered when $ReSc = 20000$ and $Re = 100$.

concentration is $C_0 = 1$. After the initial stage fluid moves forward and we expect this initial value of the concentration to remain the same within the flow region until the time it takes to reach the other boundary. We have used the formula, $\int_V C(\boldsymbol{x}, t)dV$ to calculate the total amount of the concentration at time t. Employing this formula we calculate the total amount of the concentration after time t in both the Lagrangian and Eulerian methods. The results are plotted in Fig 5.15. In Fig 5.15, the curve denoted by $(\cdot - \cdot - \cdot)$ represents the amount of concentration in the Lagrangian method and the curve denoted by $(-)$ represents the amount of concentration in the Eulerian method. We understand that in the Lagrangian method the curve remains approximately very close to initial value 1 until final time, but in the Eulerian method the curve declines from the initial value 1. Note that in Fig 5.15, there is a negligible increase of mass in the Lagrangian method at the end of the simulations. The one

of the probable reasons behind this increased mass could be the implementation of the boundary conditions. Another reason could be the production rate, *i.e.,* when oil reaches near the boundary of the production well, all the oil may not come out through the production well, therefore a few masses gain near the boundary of production well. However, the proposed Lagrangian method conserves mass. Therefore, the study of fluid flow using the Lagrangian method satisfies the mass conservation law but the Eulerian method does not satisfy the mass conservation law.

5.5 Effect of viscosity

Viscosity reduction is one of the important challenging issues for the oil industry from the production to the consumption stage (Abdurahman *et al.*, 2012; Homayuni *et al.*, 2011; Tao & Xu, 2006; Saniere *et al.*, 2004). We notice that in the Figs 5.6 and 5.7 there is a significant difference between the shape of the flow and the flow movement (speed of the flow). The only difference among the parameter values between these two simulations is the Reynolds number, *i.e.,* in Fig 5.6, the Reynolds number $Re = 1$, and in Fig 5.7, the Reynolds number $Re = 100$. We choose two representative cases: one from Fig 5.6 and another one from Fig 5.7, and both cases are displayed in Fig 5.16. We notice that when viscosity is reduced by a factor of 100, the parabolic shape of the concentration field is changing toward the flat shape (see Fig 5.16(c)) and also the flow rate increases. From this observation we realize that viscosity reduction may help the EOR process. We will discuss this issue elaborately in the next chapter.

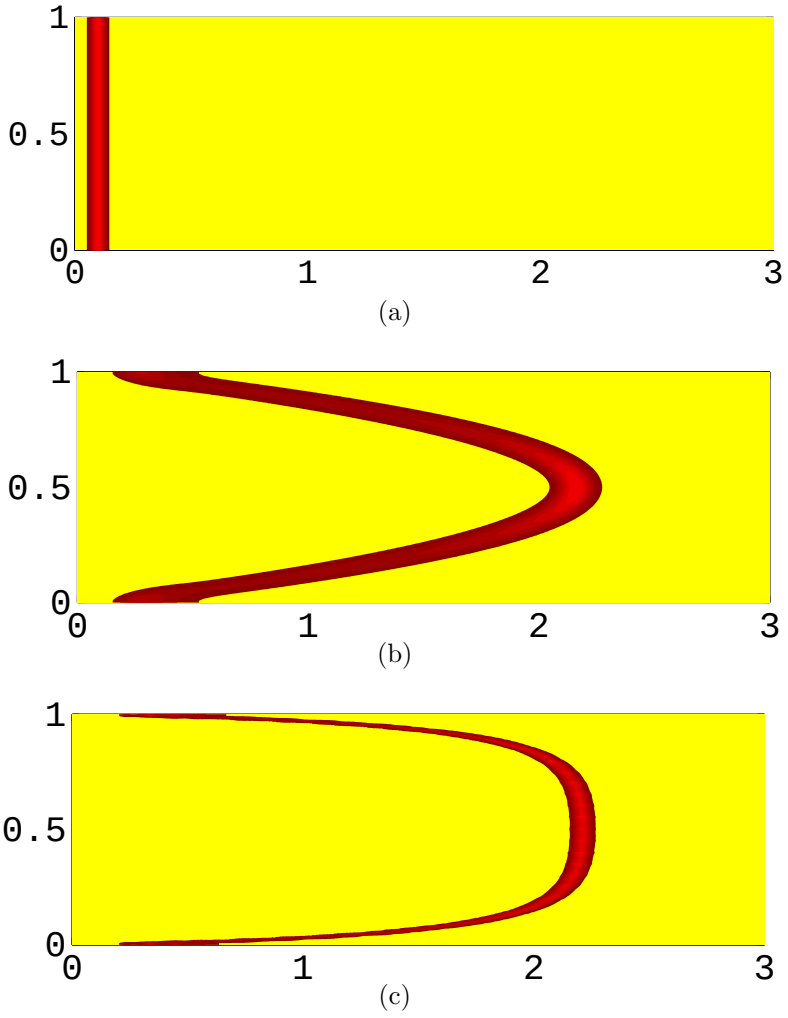

Figure 5.16: Effect of viscosity on the flow field when $ReSc = 20000$: (a) initial stage, (b) Flow at high viscosity, *i.e.*$Re = 1$ at time, $t = 24.5$, and (c) Flow at low viscosity, $Re = 100$ at time, $t = 2.55$.

5.6 Summary

Finally, we conclude with the following comments:

- The Numerical diffusion is not dominant over physical diffusion in the proposed Lagrangian method, whereas the Eulerian method has the significant numerical diffusion. Thus, the proposed Lagrangian method is able to minimize the impact of numerical diffusion and also it has no time step restriction for numerical stability.

- Obi & Blunt (2004) articulated that Batycky *et al.* (1997) designed a three dimensional streamline based method which is $10 - 1000$ times faster than the traditional finite difference method. Our proposed Lagrangian method is about 100 times faster in time step.

- When viscosity of fluid is reduced, then fluid moves faster. For instance, in Fig 5.6, fluid reaches this position at time $t = 24.5$ when viscosity is higher, *i.e.,* the Reynolds number $Re = 1$, whereas fluid reaches almost the same position at time $t = 2.55$ when viscosity lower, *i.e.,* the Reynolds number $Re = 100$ (Fig 5.7).

The present streamline based Lagrangian method permits reasonable large time steps and is free from much numerical diffusion. This method holds the mass conservation law and is computationally inexpensive. Therefore, the efficiency of the streamline based Lagrangian method offers a unique opportunity to study the simulations in the oil reservoir.

Chapter 6

Viscous effects on miscible fluid flow in porous media

The viscosity of crude oil plays a pivotal role in the oil industry. Oil viscosity influences the flow of oil through porous media (Ghosh & Shalabi, 2011). If the viscous force can be reduced then the EOR process will help to sweep out more oil to the production well. Depending on the method and reservoir condition, viscosity of oil can be reduced by 10 to 90% and the recovery incremental goes up to 25% (Kumar *et al.*, 2008; McGuire *et al.*, 2005; Nobakht *et al.*, 2007). According to scientific literature, the specific effects of viscous forces still remain fully unstudied or not well understood (Nobakht *et al.*, 2007). Therefore, it is a challenging and interesting topic to study the viscous effect in the EOR precess.

6.1 Objective of the chapter

In this chapter, we aim to investigate the viscous effect on the flow of two miscible fluids through an idealized model with porous media, and the influences of permeability on the flow field. We study the effect of CO_2-oil dissolution on the overall pressure drag and skin friction experienced by the porous media by using statistical-mechanical theory of viscosity.

6.2 Idealized model for the flow in porous media

The field of reservoir simulation in the oil industry has been developed more in the last few decades. To simulate the reservoir flow, an idealized model is needed so that field data can be used. A list of the pertinent parameters are listed in table 6.1 from relevant references. Ghosh & Shalabi (2011) used the data to study viscosity reduction in the EOR process. Chaudhary (2011) simulated the flow by considering the reservoir thickness of 200 ft of the *Eagle Ford Shale* reservoir, Texas, USA. Kumar *et al.* (2008) articulated a large number of field and simulation data that are summarized in table 6.1 while they were studying high mobility ratio of water flooding and performance of prediction of the reservoir. Chen *et al.* (2006) described an ideal reservoir domain with different thickness of the reservoir layer (30-50 ft) and permeability (20-150 mD). Christie *et al.* (2001) chose 50ft thickness for their gas-injection model in reservoir simulation and 170ft thickness of waterflood of a large geostatistical model in their study. Adams (1982) used the field data from the heavy-oil reservoirs in the Lloydminster area of western Canada to study the behavior of waterflood performance in this reservoir. We use the data mentioned in table 6.2 for an idealized reservoir model. First, we discuss the effects of viscosity on the flow in

Parameter	Ghosh & Salabi (2011)	Chaudhary (2011)	Kumar *et al* (2008)	Christie (2001)	Adams(1982) (Lloydminster oil reservoir, CANADA)
U	0.43-3.87 ft/day	—	—	1ft/day	—
H	—	200 ft	$100 - 600$ ft	50-170 ft	$500 - 600$ m
μ	4.3-53.6 mPas	—	70-1500 cP	—	400-1500 cP
ρ	.831-.895 g/cc	—	—	—	$0.95 - 0.98$ g/cm^3
ϕ	20.8-21.9 %	6 %	23-36%	—	29-35 %

Table 6.1: List of the parameters used by relevant references: Velocity (U), Reservoir thickness (H), Oil viscosity (μ), Permeability (κ), Porosity (ϕ), Density (ρ) and Kinematic viscosity ($\nu = \mu/\rho$).

Parameter	value used in the simulations
U	3.5×10^{-6}m/$s \sim$ 1ft/day (Christie, 2001)
H	500 m (Adams, 1982)
ν	1.75×10^{-3}m^2/s (Adams, 1982)
ϕ	18% (Elsayed, 1993)

Table 6.2: List of the parameters used in the present simulations for an idealized reservoir model.

porous media.

6.3 Viscous effects on the miscible displacement

There are some advantages of using a lower viscous fluid to displace higher viscous fluid in a miscible displacement process. First, the two fluids are free to mix with each other within the porous media. Second, injected fluid is less viscous than the oil. This leads to a mixture with a viscosity less than that of the oil. Thus, a

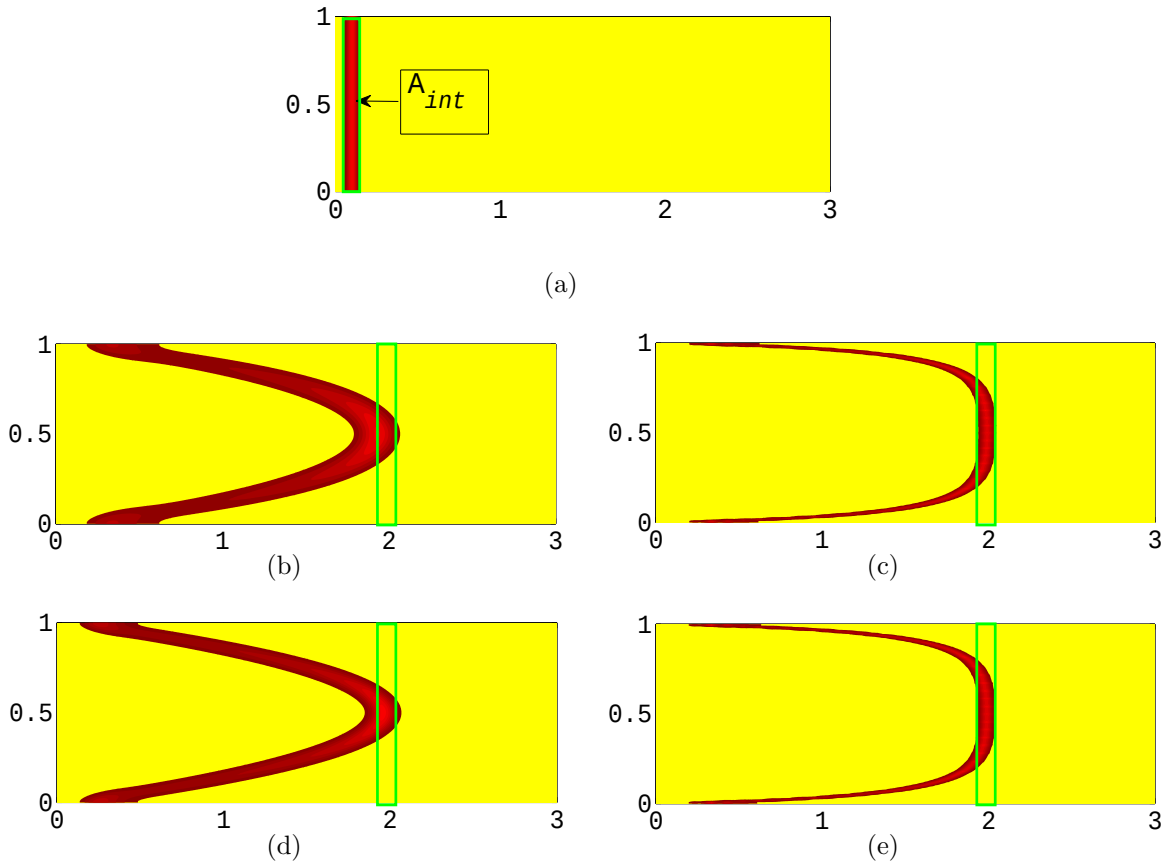

Figure 6.1: Effect of viscosity on the flow through porous media: (a) Initial concentration field after CO_2 injection is shown in red and the region in yellow represents crude oil for all cases, (b) Position of the concentration field at time, $t = 45.4$ when $Re = 1,\ Da = \phi \times 10^{-1}$, (c) Position of the concentration field at time, $t = 2.4$ when $Re = 100,\ Da = \phi \times 10^{-1}$, (d) Position of the concentration field at time, $t = 22.5$ when $Re = 1,\ Da = \phi \times 10^{6}$ and (e) Position of the concentration field at time, $t = 2.30$ when $Re = 100,\ Da = \phi \times 10^{6}$. All other parameter values are listed in table 6.3.

Parameters	Values for Fig 6.1(b)	Values for Fig 6.1(d)	Values for Fig 6.1(c)	Values for Fig 6.1(e)
$L_x \times L_y$	3×1	3×1	3×1	3×1
$n_x \times n_y$	512×128	512×128	512×128	512×128
Δt	10^{-2}	10^{-2}	10^{-2}	10^{-2}
∇P	2	2	2	2
α	1	1	1	1
c_φ	0	0	0	0
Da	10^{-1}	10^{6}	10^{-1}	10^{6}
Re	1	1	100	100
$ReSc$	2×10^4	2×10^4	2×10^4	2×10^4

Table 6.3: List of the parameters for corresponding Fig 6.1.

reduced pressure gradient is required to displace the oil, and this helps the EOR process (Booth, 2008). Modelling of miscible displacements is more difficult compared with immiscible displacements because the velocity field changes significantly as the more mobile fluid is carried into the production well (Thiele *et al.*, 1996). Nowadays, to displace higher viscous fluid by injecting a lower viscous fluid like CO_2 injection in the EOR process becomes more economical, environmentally friendly and a more effective technique. A large number of experiments and numerical simulations have been studied regarding gas or liquid injection in the EOR process.

The viscous effects play an important role during the miscible displacement of fluid. Kumar *et al.* (2005) and Ghosh & Shalabi (2011) mentioned oil viscosity is one of the common parameters in the oil industry and highly viscous oil strongly influences the flow through porous media and affects the EOR process. Ghosh & Shalabi (2011) and Mohsin & Anazi (2009) mentioned an artificial way to reduce viscosity by

using gas or solvent injection in miscible or semi-miscible fluids and the WAG (water altering gas) or SWAG (simultaneously water and gas) process. Nobakht *et al.* (2007) investigated the effects of viscosity by the injection rate and injection pressure of CO_2. McGuire *et al.* (2005) showed that when a viscosity reducing injectant (VRI) was injected, then viscosity was reduced up to 90% and oil recovery was improved by 15% - 20%. Thus, it is important to study the effects of the viscous force when a high viscous fluid is displaced by a less viscous fluid , like CO_2 injection in the EOR processes.

The present investigation is mainly concerned with the study of viscous effects on the mechanisms of miscible displacement flows in a porous media. In the case of a low Reynolds number, the flow is dominated by the pressure gradient and viscous forces. In contrast, the dominant terms for a high Reynolds number flow are the inertia and pressure gradient forces (Kundu & Cohen, 2004). Note, viscosity describes internal resistance of fluid to flow and may be thought of as a measure of fluid friction.

We see how viscous stress affects the flow pattern through the porous media. Fig 6.1 represents the effects of the viscosity on the flow field. The values of the parameter used in the present simulations are listed in table 6.3. For high viscous fluid (*i.e.* $Re = 1$), the front of the displacing fluid region has reached the position about 2 of the domain at time $t = 45.4$ (Fig 6.1(b)), whereas for a low viscous case (*i.e.* $Re = 100$), the front of the displacing fluid region has reached the same position at time $t = 2.4$ (Fig 6.1(c)) with the same Darcy number, $Da = \phi \times 10^{-1}$. Thus the flow speed of lower viscous fluid is about 19 times faster than that of a higher viscous fluid. Further, when the Darcy number increases from 10^{-1} to 10^{6}, we notice that the flow moves faster. If we compare the speed of the simulations for $Re = 1$ (Fig 6.1(d)) and $Re = 100$ (Fig 6.1(e)) by keeping all other parameters same, still we see that the flow at a lower viscosity is about 10 times faster than that of the higher viscosity. All

the simulations displayed in Fig 6.1 are at the same position of the domain, but at a different time. This indicates that if the viscosity of resident fluid (oil) is reduced, then the EOR efficiency will increase.

In addition, we clearly see that in the case of higher viscosity (*i.e.* $Re = 1$), the region of displacing fluid takes parabolic shape (Fig 6.1(b), 6.1(d)). On the other hand, the parabolic shape is tending to a relatively flat shape when viscosity is reduced by a factor of 100 (Fig 6.1(c), 6.1(e)). The shape of the flow pattern does not change but the speed of the flow does by increasing the Darcy number by a factor of 10^7, *i.e.,* allowing more permeability (Figs 6.1(c) and 6.1(d)). Thus, the distortion of CO_2 strongly depends on viscous stress (Figs 6.1(b) and 6.1(c)) or (Figs 6.1(d) and 6.1(e)).

Furthermore, to study a qualitative and quantitative measure of the distortion of the initial shape of CO_2, a rectangle has been drawn in each of the plots in Fig 6.1 and placed at the front of the displaced region by CO_2. In Fig 6.1(a) initially injected CO_2 is marked by A_{int}. The EOR process will be successful if this shape remains the same until near the production well boundary. Unfortunately, we notice that the displacing region is about half of A_{int} for $Re = 100$ cases and one-fourth of A_{int} for $Re = 1$ cases.

Therefore, the results in Fig 6.1 indicate that reducing the damping force of the porous media, *i.e.* the drag, by factor of 10^7 has no effect on the shape of the moving sample of CO_2. Since an upscaling model ignores the details of the flow in the pores of the porous matrix, the role of the viscous stress is more likely the shearing effect rather than the effect of the porous media. However, more studies of miscible flow in porous media put emphasis on determining $\mu(c)$, ignoring the viscous stress, where $\mu(c)$ appears only in the term that models the drag force. Moreover, to improve the EOR process through a miscible displacement, it is also important to

understand the necessary conditions for which a rectangular sample of CO_2 would migrate without much distortion of its initial shape. In Darcy's model, reducing $\mu(c)$ by a factor of 10 is equivalent to increasing the permeability by the same factor. An increased permeability would enhance the rate of momentum transfer, thereby requiring a balance by the shearing stress. Mixing and dissolution occurs at the molecular level. The slowly moving CO_2 molecules near a solid body will have more chance to be dissolved. This dissolution effect is neither resolved by Darcy's model nor resolved by the shearing stress.

Therefore, viscosity has a significant effect on the progress of flow of miscible fluids. In the next section we investigate the effect of permeability on the flow.

6.4 Effect of permeability

The Darcy number is a dimensionless number, which measures the permeability of the porous medium. It is important to understand how energy, heat or mass transfer are influenced by the change of the permeability of the system for a fixed length scale. Here, we define the Darcy number as $Da = \kappa/H^2$, where κ is permeability and H is the length scale of the domain. This definition of the Darcy number depends on the system under consideration, and does not express a suitable pore scale for the porous media. Thus, the Darcy number needs to be redefined based on a different length scale, which can be derived directly from the current definition of Da. For instance, a Darcy number based on the pore diameter, d, can be defined as $Da_p = d^2/H^2$ with $\kappa \sim d^2$ or ($Da_p = \kappa/d^2$) where Da_p is the Darcy number based on the pore diameter and d is the diameter of the pore. Thus, this definition of the Darcy number is more applicable for the actual flow field.

As before, we study two cases: one is the Reynolds number, $Re = 1$, and the other

Parameter	value for Figs 6.2 & 6.3	value for Figs 6.4 & 6.5
$L_x \times L_y$	3×1	3×1
$n_x \times n_y$	512×128	512×128
Δt	10^{-2}	10^{-2}
∇P	2	2
c_φ	0	0
Re	1	100
$ReSc$	2×10^4	2×10^4

Table 6.4: List of the parameters for the corresponding figures.

one is the Reynolds number, $Re = 100$, to see the effects of permeability.

6.4.1 Effect of permeability for the flow at low Reynolds number

In this study, four different Darcy numbers, $Da = \phi \times 10^{-2}, \phi \times 10^{-1}, \phi \times 10^{0}$, and $\phi \times 10^{6}$ are considered with porosity, $\phi = 18\%$. According to the definition of the Darcy number, a lower Darcy number offers higher resistance to the fluid motion, and hence allows lower flow rates. In a similar fashion, the higher Darcy number offers lower resistance to the fluid motion, and permits higher flow rates.

The influences of the Darcy number on the flow field is shown in the Fig 6.2. The parameter values used for these simulations are listed in table 6.4. In Figs 6.2(a) to 6.2(d), the fronts of the displaced fluid region by CO_2 reach different positions of the domain at the same time, $t = 30.0$. For the lowest Darcy number, $Da = \phi \times 10^{-2}$, we notice that the fluid region displaced by CO_2 moves slowly (Fig 6.2(a)). Accordingly,

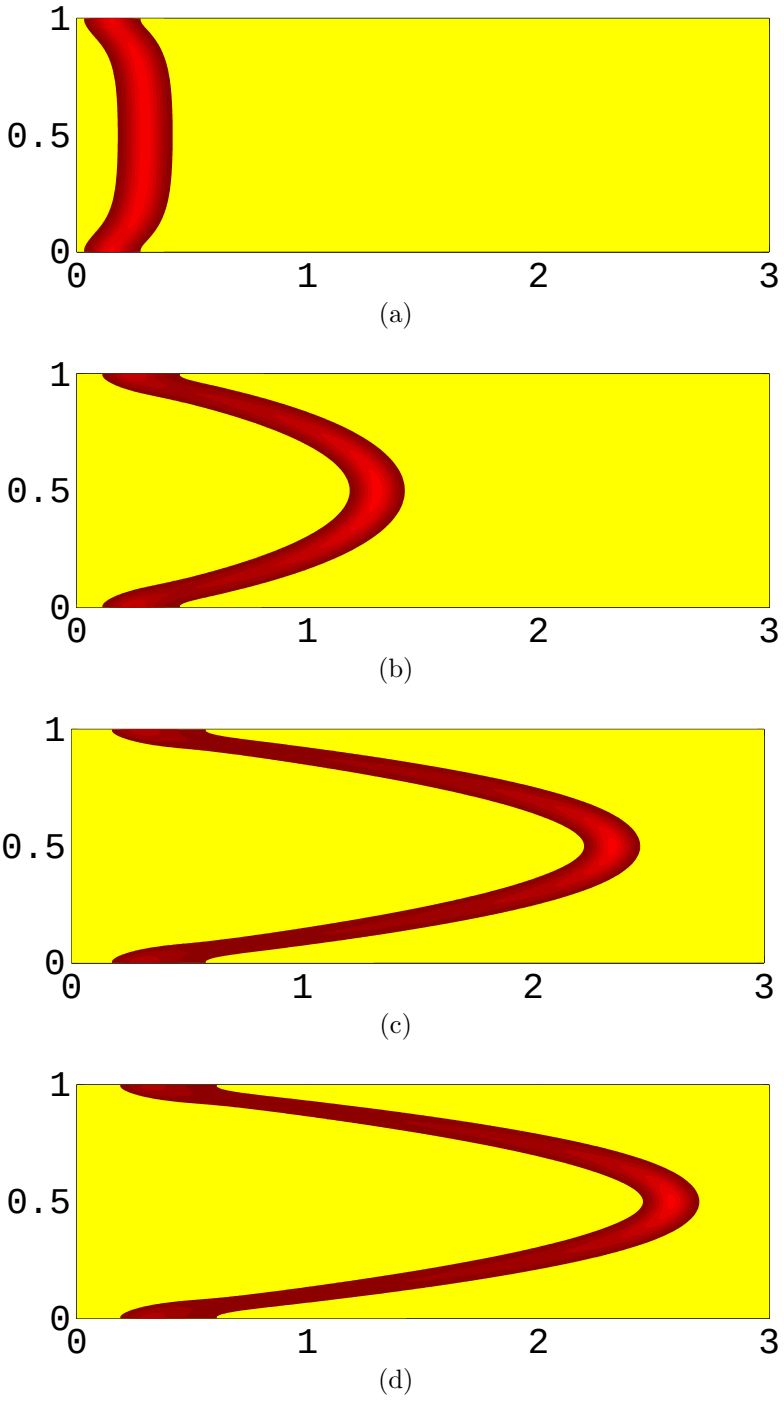

Figure 6.2: Temporal evolution of the flow under the influence of the Darcy number, when $Re = 1$ and $\phi = 18\%$: (a) $Da = \phi \times 10^{-2}$, (b) $Da = \phi \times 10^{-1}$, (c) $Da = \phi \times 10^{0}$, (d) $Da = \phi \times 10^{6}$, all the cases are at the same time, $t = 30$. The parameter values are listed in the table 6.4.

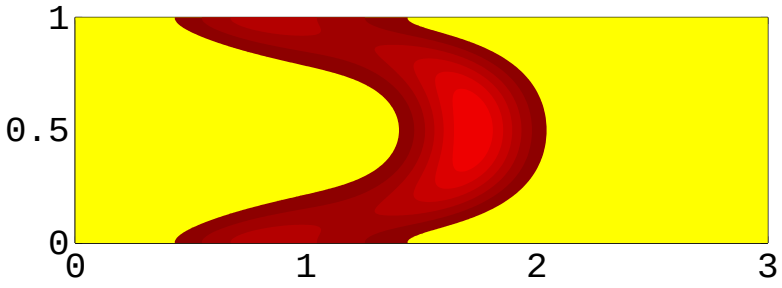

(a)

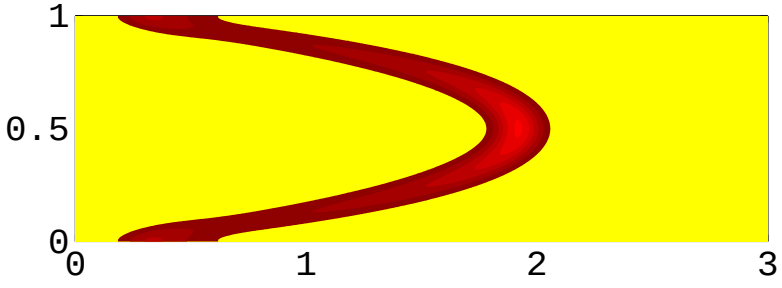

(b)

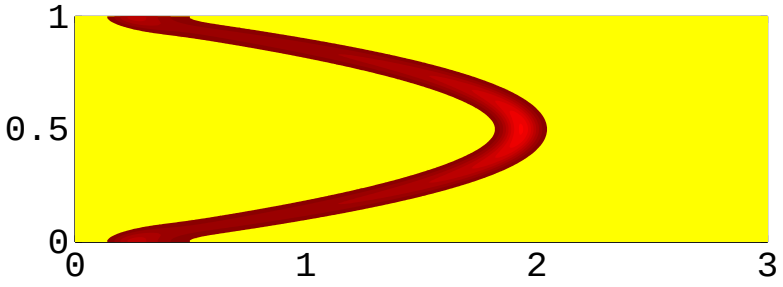

(c)

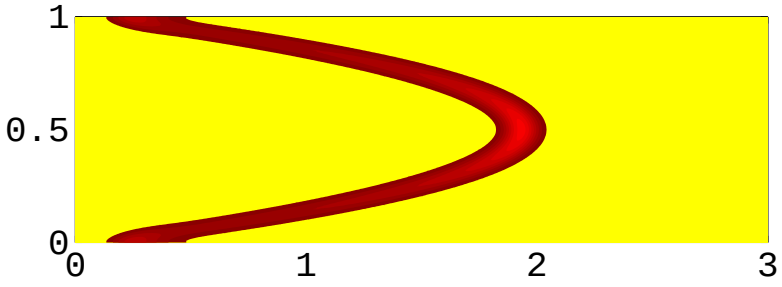

(d)

Figure 6.3: Influence of the Darcy number on the flow field when $Re = 1$: (a) $Da = \phi \times 10^{-2}$ at time, $t = 250$, (b) $Da = \phi \times 10^{-1}$ at time, $t = 45.4$, (c) $Da = \phi \times 10^{0}$ at time, $t = 24.4$, (d) $Da = \phi \times 10^{6}$ at time, $t = 22.5$. The parameter values are listed in the table 6.4.

we see that for the highest Darcy number, $Da = \phi \times 10^6$, the fluid region displaced by CO_2 moves quickly (Fig 6.2(d)). Thus, it is clear that the lower Darcy number has more resistance on the flow than the higher Darcy number. Another important observation is that the lower Darcy number cases have more mass dispersion than the higher Darcy number cases. In Fig 6.2, we see that mass dispersion is gradually decreasing when the Darcy number is increasing (Figs 6.2(a) to 6.2(d)).

Fig 6.3 represents the same simulations presented in Fig 6.2 but at the same position of the domain. Here we see that for the lowest Darcy number, $Da = \phi \times 10^{-2}$, the fluid region takes time, $t = 250$, to reach this position. The reach time is gradually decreasing with the increase of the Darcy number, Da, for example, the highest Darcy number, $Da = \phi \times 10^6$, the fluid region takes time, $t = 22.5$ to reach the same position. In addition, we see that mass dispersion increases significantly for the lower Darcy number than for the higher Darcy number. Note, we notice that for the highest Darcy number, $Da = \phi \times 10^6$, requires a reach time at the same position to be 11 times faster than the lowest Darcy number, $Da = \phi \times 10^{-2}$. In the neat subsection, we carry out a similar study for the lower viscous fluid.

6.4.2 Effects of permeability for the flow at high Reynolds number

In the high Reynolds number case, we also consider four Darcy numbers to investigate the effects of permeability. The parameter values used in the simulations are listed in table 6.4. All the simulations displayed in Fig 6.4 are plotted at the same time, $t = 2$, but at different positions of the domain. Again, all the simulations exhibited in Fig 6.5 are plotted at the same position of the domain, but at a different time. Note that all the parameter values for the simulations presented in Figs 6.4 and 6.5

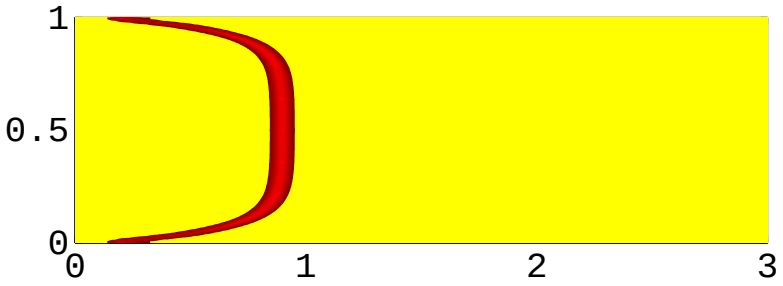

(a)

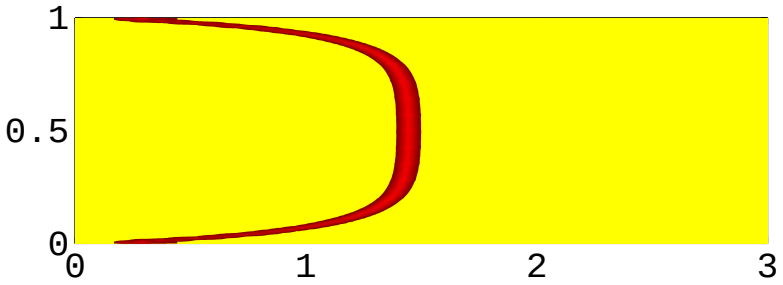

(b)

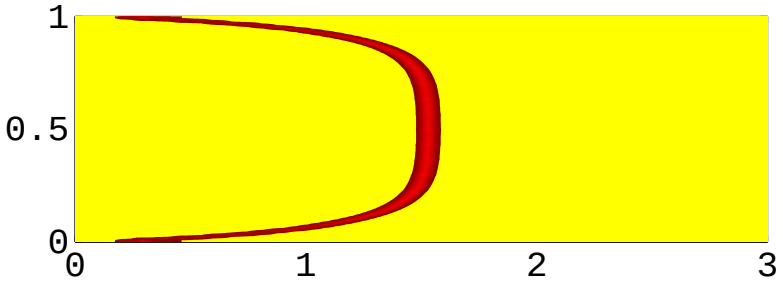

(c)

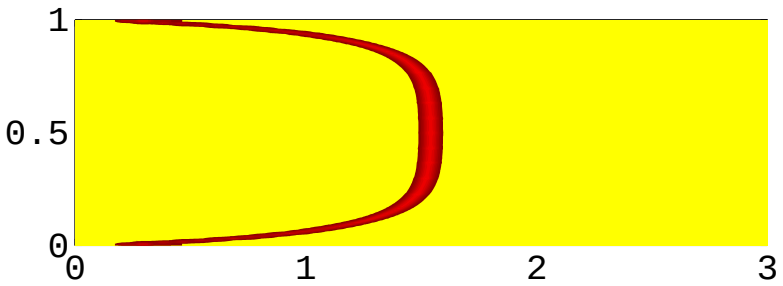

(d)

Figure 6.4: Influence of the Darcy number on the flow field when $Re = 100$ and at same time, $t = 2$: (a) $Da = \phi \times 10^{-2}$, (b) $Da = \phi \times 10^{-1}$, (c) $Da = \phi \times 10^{0}$, (d) $Da = \phi \times 10^{6}$. The parameter values are listed in the Table 6.4.

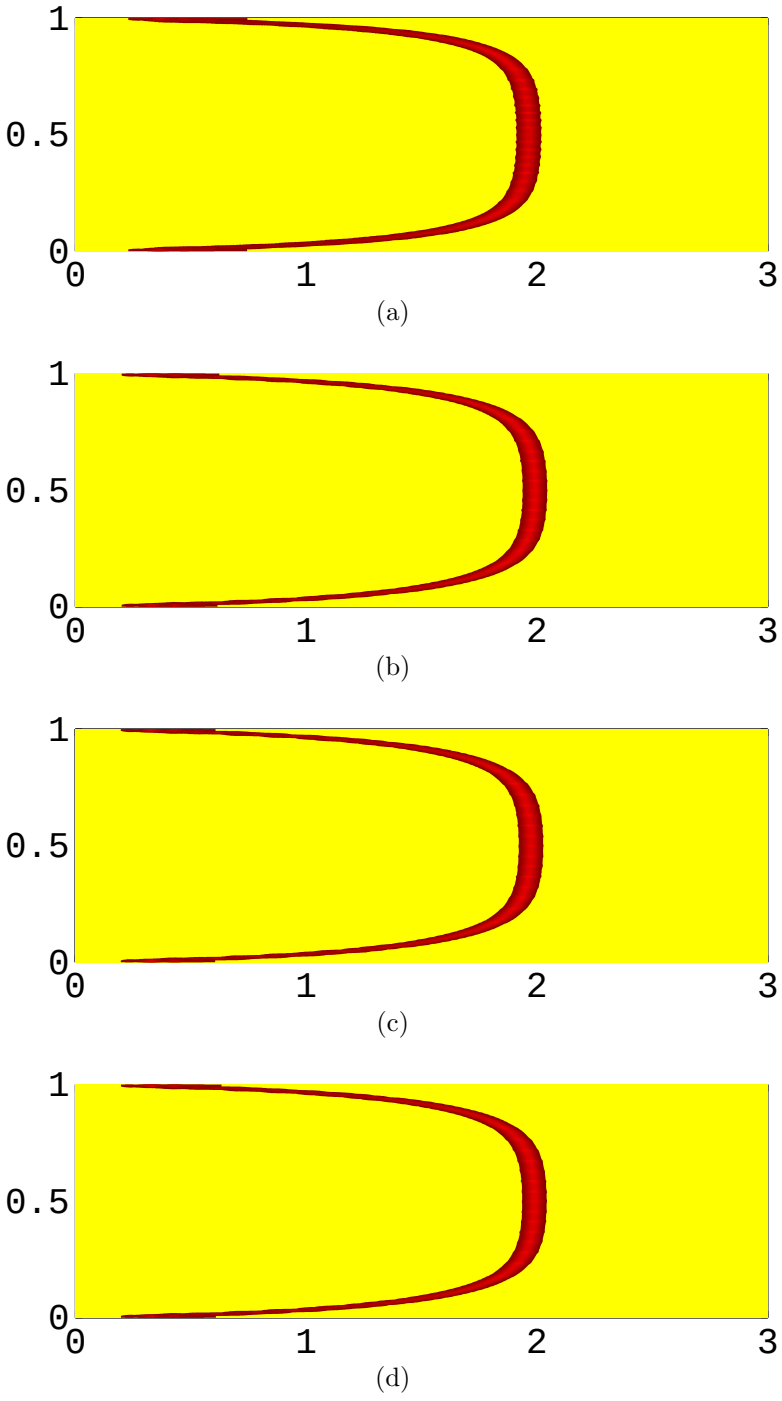

Figure 6.5: Influence of the Darcy number on the flow field when $Re = 100$: (a) $Da = \phi \times 10^{-2}$ at time, $t = 3.7$, (b) $Da = \phi \times 10^{-1}$ at time, $t = 2.4$, (c) $Da = \phi \times 10^{0}$ at time, $t = 2.31$, (d) $Da = \phi \times 10^{6}$ at time, $t = 2.30$. The parameter values are listed in the Table 6.4.

are the same. The same behaviors of the Darcy number as seen in the lower Reynolds number are also expected in the higher Reynolds number case. This means that the lower Darcy number offers the higher resistance to the fluid motion, and hence, allows lower flow. In other words, the higher Darcy number offers the lower resistance to the fluid motion and permits higher flow.

For each simulation we calculate the time for the front of the fluid region displaced by CO_2 to reach the same position of the domain. In the lowest Darcy number, $Da = \phi \times 10^{-2}$ case, we notice that the displaced fluid region moves slowly (Fig 6.4(a) or Fig 6.5(a)). Accordingly, for the highest Darcy number case, $Da = \phi \times 10^{6}$, the displaced fluid region moves faster (Fig 6.4(d) or Fig 6.5(d)) than for the lowest Darcy number (Fig 6.4(a) or Fig 6.5(a)). We see that for the Darcy number where $Da = \phi \times 10^{-2}$, the fluid region takes time, $t = 3.7$, (Fig 6.5(a)), whereas for the Darcy number, $Da = \phi \times 10^{6}$, it takes time, $t = 2.30$, (Fig 6.5(d)) to reach the same position of the domain. Thus, it is found that in the highest Darcy number, $Da = \phi \times 10^{6}$ case, the front of the fluid region moves at about 1.6 times faster than it does for the lowest Darcy number, $Da = \phi \times 10^{-2}$, in terms of the reach time at the same position.

Therefore, we notice that the region displaced by CO_2 moves faster with the increasing Darcy number. This acceleration is also influenced by the Reynolds number, Re. In addition, the shape of the region displaced by the CO_2 sample is not controlled by the Darcy numbers, but depends on the Reynolds number, Re. This indicates that the hydrodynamical dispersion is important.

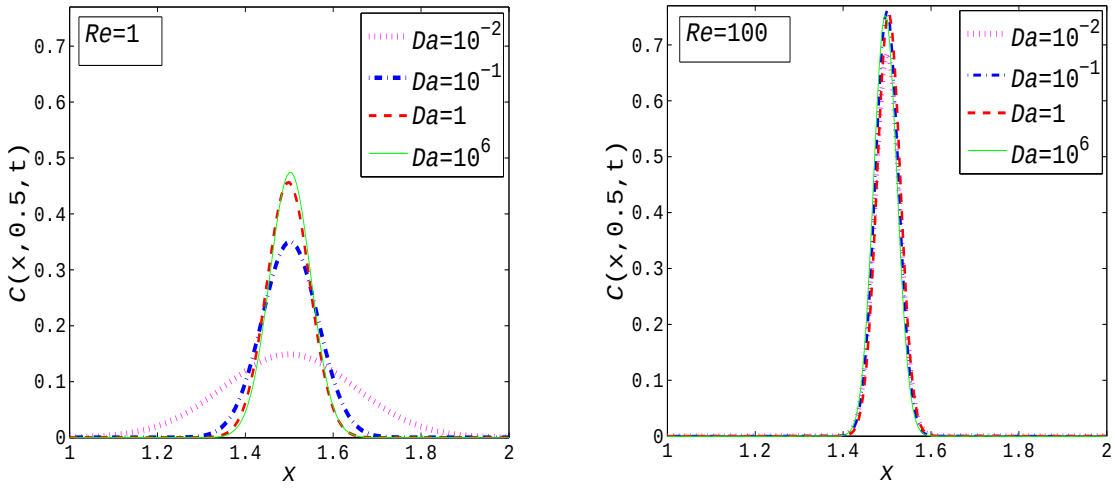

(a) (b)

Figure 6.6: Effects of Darcy number on mass diffusion. Concentration profiles, $C(x, 0.5, t)$, are calculated along a line at $y = 0.5$ and presented for various values of Da: ***(a)*** The profiles of the simulations presented in Fig 6.3 when $Re = 1$ and ***(b)*** The profiles of the simulations presented in Fig 6.5 when $Re = 100$. At different time evolution.

6.4.3 Effect of permeability on mass diffusion

To investigate the effects of the Darcy number on mass diffusion, we take the profiles of the concentration fields of simulations that are displayed in the Fig 6.3 (when $Re = 1$) and Fig 6.5 (when $Re = 100$) along the center line of the y-axis of the domain and presented in Fig 6.6(a) and Fig 6.6(b), respectively. We observe that for the flow at high viscosity, *i.e.,* $Re = 1$, mass diffusion is significant when the Darcy number is small and mass diffusion decreases with the increase of the Darcy number. For the flow at low viscosity, *i.e.,* $Re = 100$, mass diffusion is not significant and it remains almost the same with the variation of the Darcy number. This means that when viscosity is reduced, then mass diffusion is also reduced.

6.5 Dispersion phenomena in miscible displacement

For a fluid flow through an isotropic porous medium, the dispersion depends largely on the velocity field (Koch & Brady, 1985; Hsu & Cheng, 1990). To help the EOR process with a miscible displacement technique, both the shape of the region displaced by CO_2 and the arrival time at the production well are the most important factors. By keeping a flat band of the region displaced by CO_2 like the initial flat band, it would optimize the oil recovery. Also a positive vertical velocity near the upper boundary and a negative vertical velocity near the bottom boundary would prevent the parabolic bending of the shape of the region displaced by CO_2.

Fig 6.7 exhibits the horizontal and vertical velocity profiles along the center line of the x-axis of the domain for the flow at the Reynolds number, $Re = 1$, with various Darcy numbers. The flow becomes a steady state at time, $t = 0.8$, when $Da = \phi \times 10^0$. The horizontal velocity gradually increases when the Darcy number increases (Fig 6.7(a)). This type of behavior was mentioned by Alazmi & Vafai (2004) and Chen & Vafai (1996). We see that for the small Darcy number (Da is the order of 10^{-2} or less) vertical velocity is near zero. The vertical velocity increases with the increase of the Darcy number (Fig 6.7(b)). We see that vertical velocity has a positive magnitude on the upper half of the domain and a negative magnitude on the lower half of the domain. We also notice that the maximum values of the horizontal velocity components for the flow at the Reynolds number, $Re = 100$, are larger than the flow at the Reynolds number, $Re = 1$, for the same Darcy number in each case. The reason for this is the reduction of the viscosity by a factor of 100.

For $Re = 1$, the inertia effect is balanced by the viscous stress, and the pressure gradient force is balanced by the drag force exerted by the porous media if $Da/\phi = 1$. The drag force dominates if $Da/\phi < 1$ and the pressure gradient dominates if

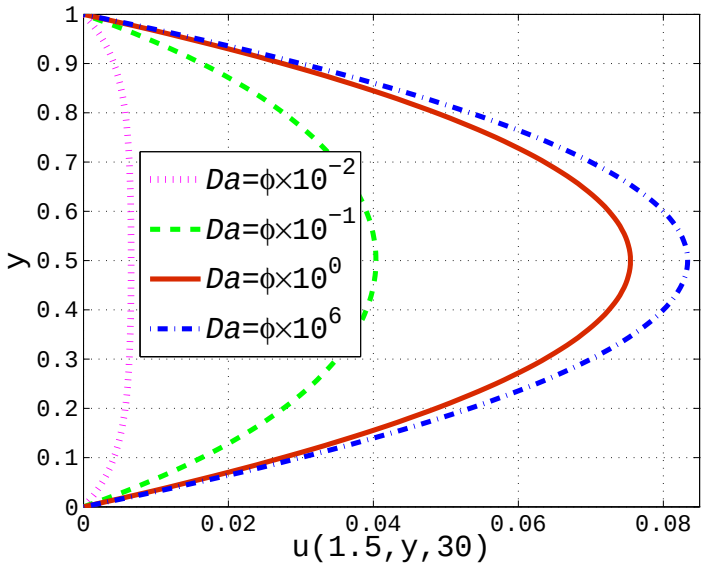

(a)

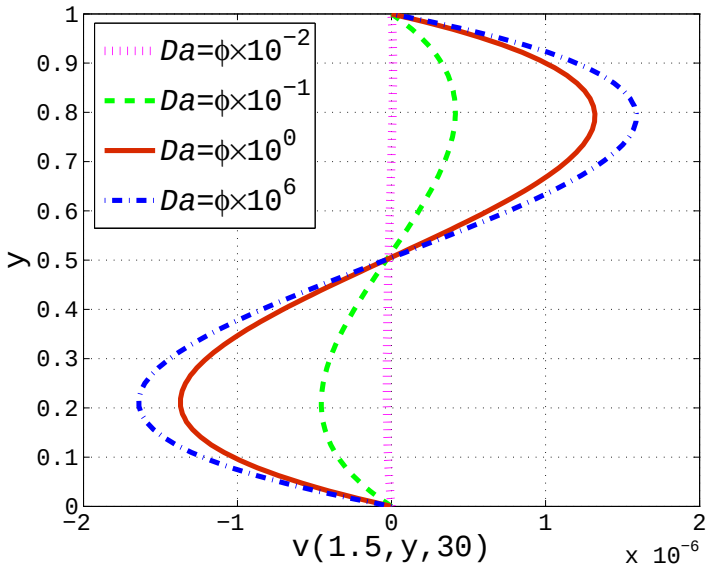

(b)

Figure 6.7: Effect of the Darcy number on velocity field, $\boldsymbol{u}$ at time, $t = 30$ for $Re = 1$. The profiles are calculated along the center line of x-axis at $x = 1.5$. (a) Horizontal velocity profile, $u(1.5, y, 30)$, (b) Vertical velocity profile, $v(1.5, y, 30)$. The parameter values are listed in table 6.4.

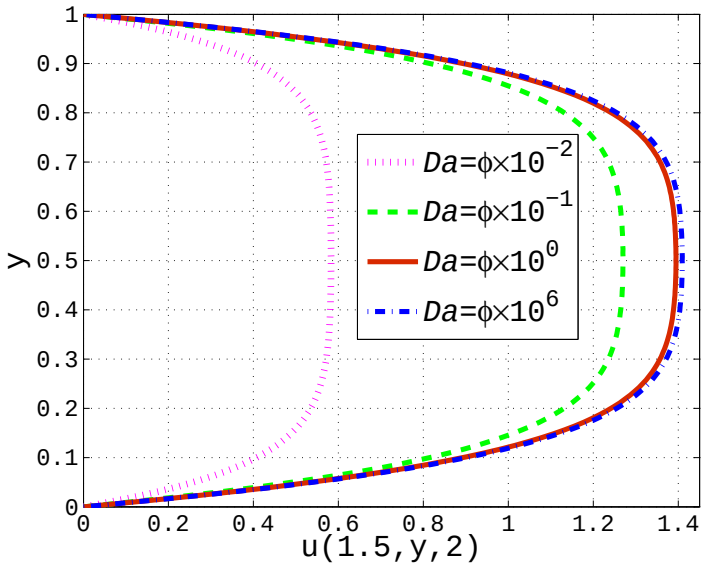

(a)

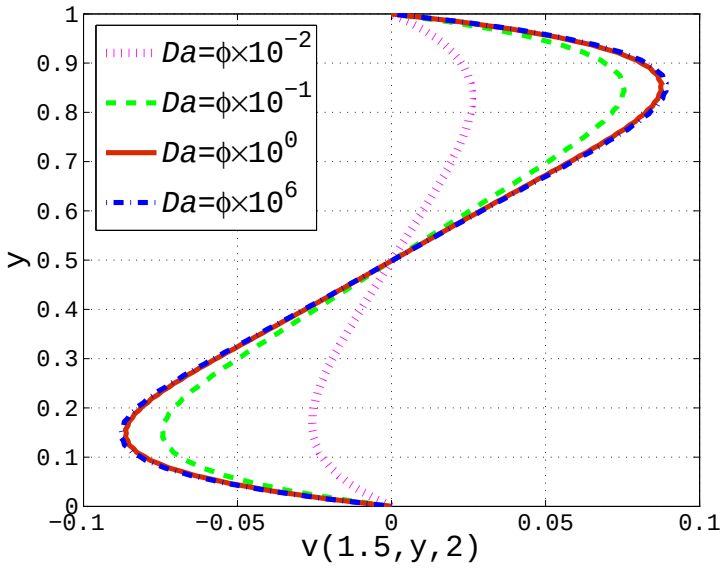

(b)

Figure 6.8: Effects of the Darcy number on velocity field, $\boldsymbol{u}$ at time, $t = 2$ for $Re = 100$. The profiles are calculated along the center line of x-axis at $x = 1.5$. (a) Horizontal velocity profile, $u(1.5, y, 2)$, (b) Vertical velocity profile, $v(1.5, y, 2)$. The parameter values are listed in table 6.4.

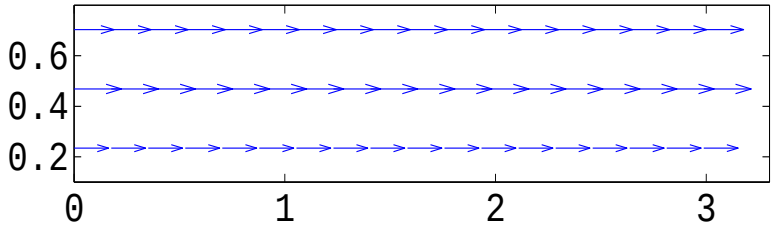

(a)

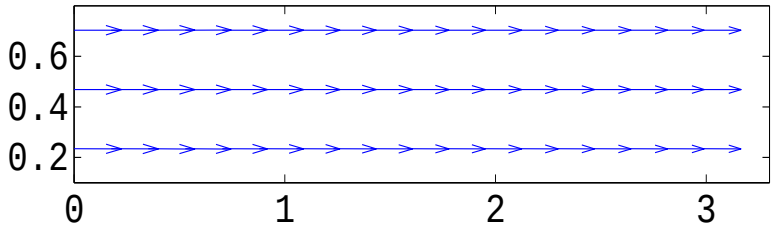

(b)

Figure 6.9: Flow direction of the velocity field. (a) when $Re = 1$, (b) when $Re = 100$.

$Da/\phi > 1$. Note that the flow remains unsteady for $Re = 100$, where inertia effects is dominant over the viscous stress, and the pressure gradient is balanced by the drag force of the porous media for $Da/\phi = 10^{-2}$. Figs 6.7(a) and 6.8(a) show that the parabolic shape of the horizontal velocity profiles takes on a relatively flat shape, when non-linear inertia effects in the porous media dominate, and the strength of the horizontal flow increases if the Darcy number, Da, increases. The vertical velocity profiles clearly indicate that the hydrodynamical transverse dispersion is influenced by the dominant inertia effects. Furthermore, the vertical velocity profiles in Figs 6.7(b) and 6.8(b) show that the region displaced by CO_2 as a flat band is enhanced by a factor of about 10^5, if the viscous stress is reduced by a factor of 10^2.

Further, Fig 6.9(a) indicates the direction of the velocity field for the flow at the Reynolds number, $Re = 1$. We see that the flow is in the horizontal direction and the shape is parabolic. In addition, the direction of the velocity field for the flow at the

Parameter	values for Fig 6.10	values for Fig 6.11
$L_x \times L_y$	3×1	3×1
$n_x \times n_y$	512×128	512×128
Δt	10^{-2}	10^{-2}
∇P	2	2
$\nabla \varphi$	1	1
Da	$\phi \times 10^{0}$	$\phi \times 10^{-2}$
Re	1	100
$ReSc$	2×10^{4}	2×10^{4}

Table 6.5: List of the parameters for corresponding figures.

Reynolds number, $Re = 100$, is plotted in Fig 6.9(b). We also notice that the flow is along the horizontal direction but the shape is not parabolic. This means that the changing of the shape of the flow depends on viscosity. Furthermore, we notice that for the high viscous flow the magnitude of the velocity near the impermeable walls is smaller then the magnitude at the center line of the domain (Fig 6.9(a)). Again, when viscosity is reduced, the magnitude of the velocity near the impermeable walls is almost the same as the magnitude of the center line (Fig 6.9(b)). This indicates that viscosity reduction may help the EOR processes.

6.6 Effects of the boundary layer width

In this section, we discuss the effects of a solvent dissolution depending on μ^c which is a function of space. We investigate the role of μ^c when λ changes but the overall strength of the drag force associated with dissolution of the solvent F^S remains the same.

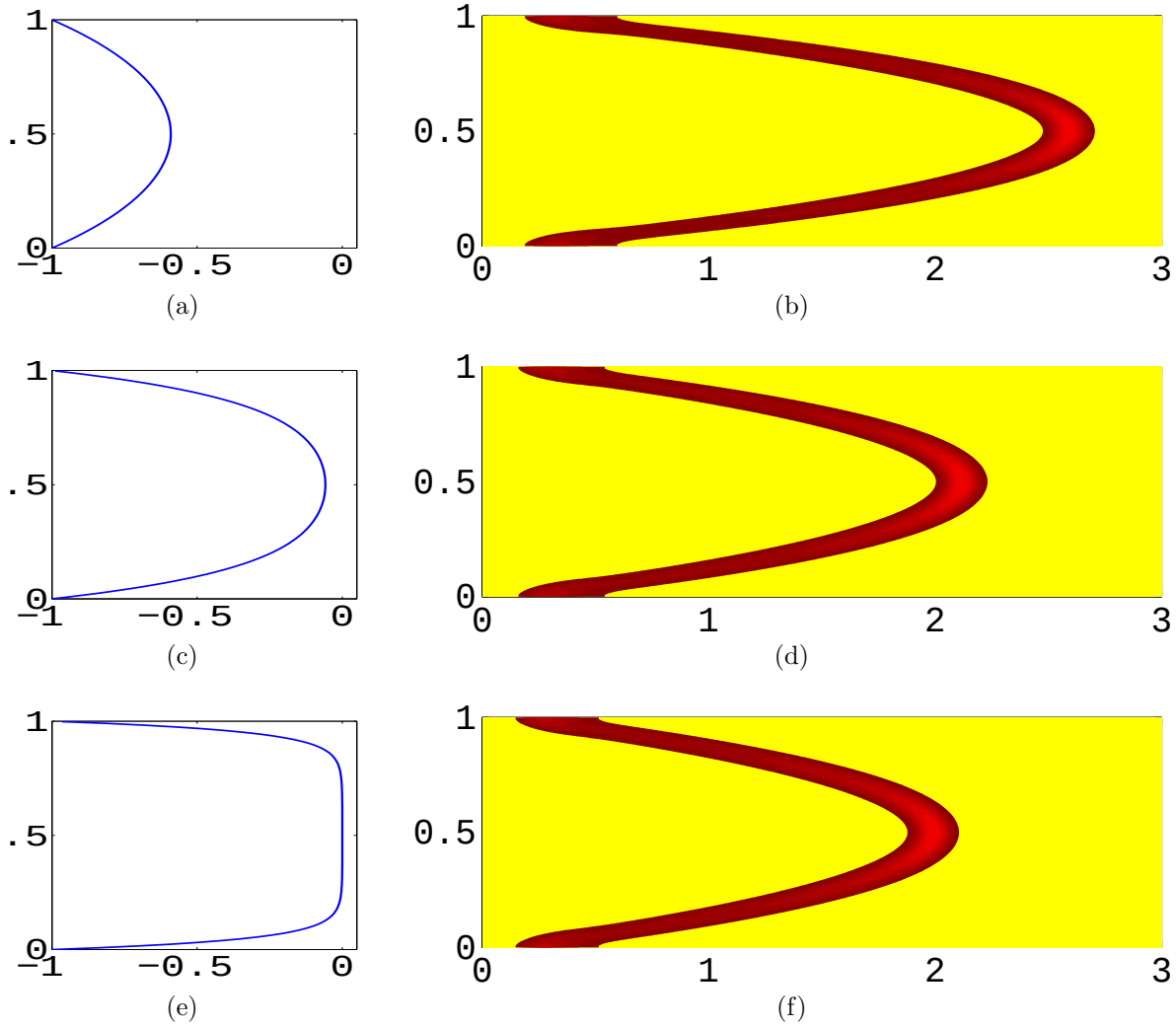

Figure 6.10: Effect of boundary layer width, λ. Left column represents $\mu^c(1.5, y)$ and right column represents concentration field, $C(x, y, 25)$ for $Re = 1$ and $Da = \phi \times 10^0$. (a) & (b) $\lambda^2 = 2 \times 10^{-1}$, (c) & (d) $\lambda^2 = 2 \times 10^{-2}$ and (e) & (f) $\lambda^2 = 2 \times 10^{-3}$. The parameter values are listed in table 6.5.

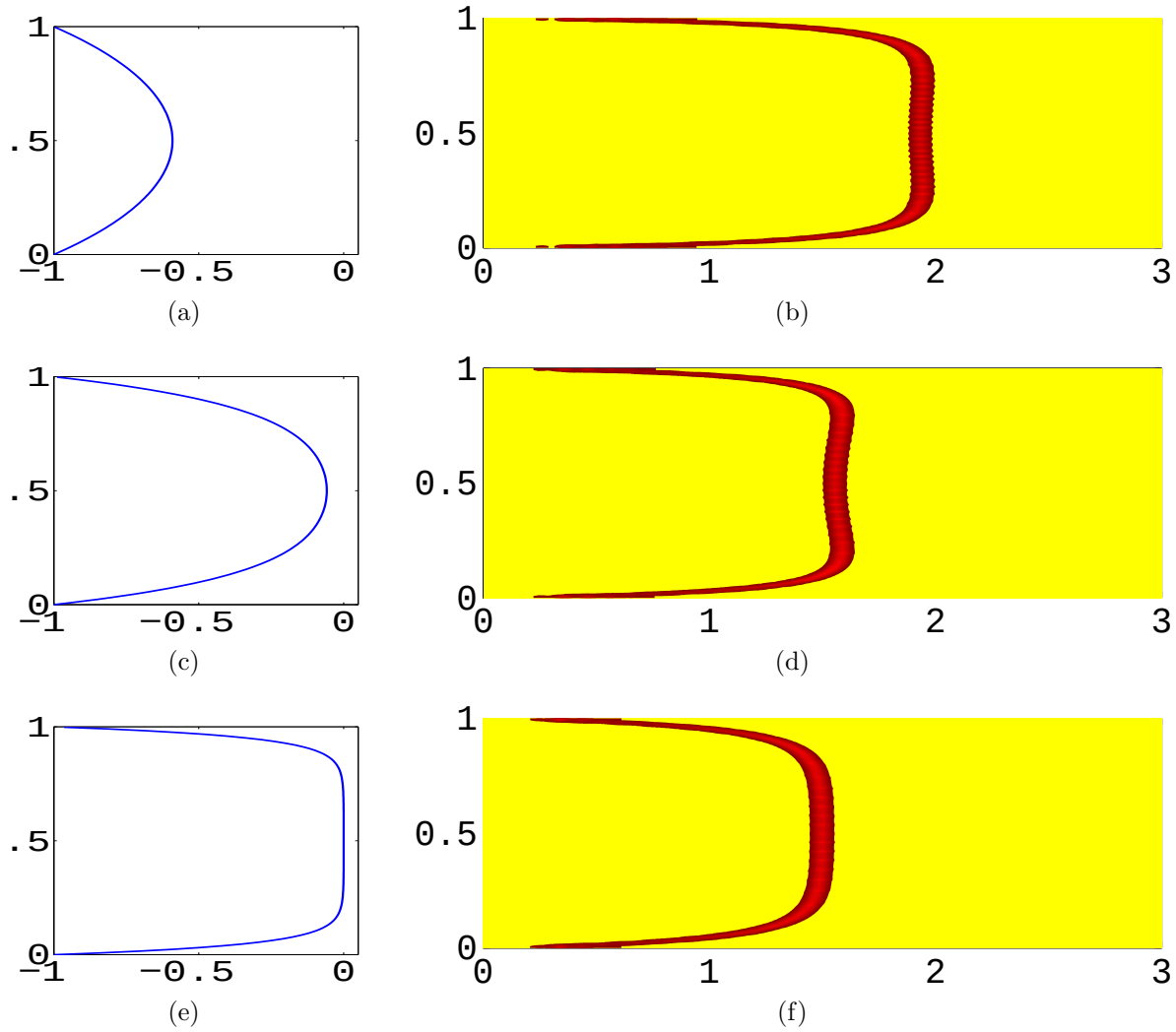

Figure 6.11: Effect of boundary layer width, λ. Left column represents $\mu^c(1.5, y)$ and right column represents concentration field, $C(x, y, 3)$ for $Re = 100$ and $Da = \phi \times 10^{-2}$. (a) & (b) $\lambda^2 = 2 \times 10^{-1}$, (c) & (d) $\lambda^2 = 2 \times 10^{-2}$ and (e) & (f) $\lambda^2 = 2 \times 10^{-3}$. The parameter values are listed in table 6.5.

First, we perform numerical experiments by decreasing the values of λ and keeping $Re = 1,\ Da = \phi \times 10^0$ with $c_\varphi = \lambda^2$. The results with $\lambda^2 = 2 \times 10^{-1},\ 2 \times 10^{-2}$ and 2×10^{-3} are presented in Fig 6.10. Here, the first column represents $\mu^c(1.5, y)$ and the second column represents the concentration field for various values of λ^2. We clearly see the influences of λ on μ^c and μ^c would accelerate the flow near each of the impermeable boundaries in a region of width λ. By keeping $c_\varphi/(\lambda^2 ReDa) = 1$, we are able to examine how a space dependent viscosity, μ^c, influences mass and momentum transfer in a porous medium. For $Re = 1,\ Da = \phi \times 10^0$, we notice that the concentration field gets accelerations to move toward the production well if the value of λ increases. In Fig 6.10, all the concentration fields are plotted at the same time, and we observe that when the value of λ^2 increases from 2×10^{-3} to 2×10^{-1} then the concentration field moves faster than it does for the lower value of λ^2 (Fig 6.10(b)).

We also examine the influences of μ^c on the concentration field by changing λ, and viscosity is reduced by a factor of 100, *i.e.,* $Re = 100$. In this case, we also keep $c_\varphi/(\lambda^2 ReDa) = 1$ with $Da = \phi \times 10^{-2}$. We present μ^c in the first column of Fig 6.11 for various values of λ and the concentration field for the corresponding values of λ in the second column. We witness the same influences of μ^c on the concentration field for the Reynolds number, $Re = 1$. This means that when the value of λ increases, then the fluid moves faster. The concentration fields are plotted in Fig 6.11 at the same time for various values of λ. We see that for the higher value of λ, *i.e.*, 0.2, the concentration field travels farther than for the case of the lower value of λ with the same time evaluation, *i.e.* $C(x, y, 3)$ (Fig 6.11(b)). Note that for a small value of λ, μ^c is nearly zero except in a narrow region that is adjacent to the boundaries.

6.7 Piston-like miscible displacement

When the interface of the displacing fluid portion is flat enough to sweep out a maximum amount of oil to the production well, then this type of displacement process is termed as a piston-like displacement (Latil, 1980). This type of displacement occurs when the fluid motion is controlled by viscous forces (Semmelbeck & HoldItch, 1988; Kjonsvik & Alvestad, 1995).

We use the following mathematical formula to calculate the efficiency of the displacement process:

$$A_{\text{eff}} = \frac{A_{\text{dis}}}{A_{\text{int}}} \times 100\%, \tag{6.1}$$

where A_{eff}, A_{int} and A_{dis} represent efficiency of the displacement process, initial fractional volume of expected displaced area and fractional volume of the displaced area, respectively. A_{eff}, A_{int} and A_{dis} will measure the fractional volume of the mass or concentration that accumulates within the region.

We apply this efficiency measurement formula to the simulations presented in Fig 6.1 in section 6.3. We immediately find that the efficiency is 21.5% for the case of $Re = 1$, *i.e.,* for the flow at high viscosity (Fig 6.1(b)), and for the low viscosity case where $Re = 100$, the efficiency is 58.7% (Fig 6.1(c)). Therefore, from these simulations we understand that if viscosity is reduced, then the displacement efficiency will increase.

In this section, we investigate the potentiality of the present statistical mechanical theory of viscosity. We discuss a conceptual model demonstrating how the flow pattern becomes piston like when a statistical-mechanical theory of viscosity is taken into consideration.

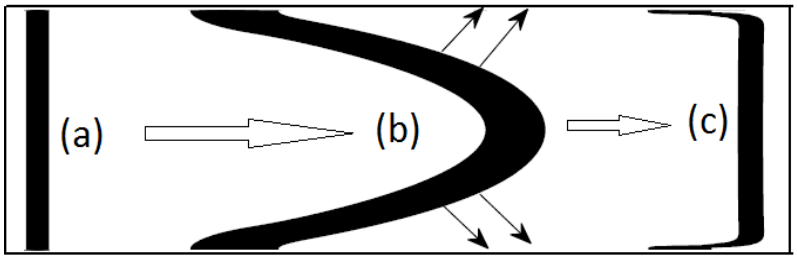

Figure 6.12: Conceptual model for solvent dissolution into oil. (a) Initial stage, (b) Dispersion or diffusion before solvent induced, (c) Expected flat shape of miscible displacement to enhance EOR.

6.7.1 A conceptual model to study solvent dissolution into oil

In the previous chapter, we saw how initially injected CO_2 (Figs 5.16(a) to 5.16(c)) was dispersed or diffused during the travel of flow in the reservoir. We aim to study how viscosity reduction helps the EOR process. In Fig 6.12, we illustrate three situations of mass transport phenomena, (a) the initial concentration distribution, (b) mass diffusion or dispersion during fluid flow in the domain, and (c) expected shape of the region displaced by CO_2 when a solvent is induced. Next, we investigate how statistical-mechanical theory of viscosity plays a role to resolve solvent dissolution.

6.7.2 Effects of the solvent dissolution for the flow at lower Reynolds number

In this investigation, we use boundary layer width, $\lambda^2 = 7.1 \times 10^{-5}$, the Darcy number, $Da = \phi \times 10^0$, the Reynolds number, $Re = 1$, and model parameter, $c_\varphi = 0.42$, to study solvent dissolution into oil. Three values of the Schmidt number, $Sc = 1 \times 10^4,\ 2 \times 10^4$, and 1×10^5 are used for the simulations, and the simulations

are presented in Fig 6.13. Other parameter values used for these simulations are listed in table 6.6.

The spatial dependent viscosity, $\mu^c(1.5, y)$, is depicted in Fig 6.13(a) where we see that the maximum value of $\mu^c(1.5, y)$ is near zero. We also see that flow patterns become piston-like as expected (Fig 6.13(b)-6.13(d)). In addition, we employ the formula expressed in eqn.(6.1) to calculate the efficiency of the miscible displacement. The efficiency for the simulations which are presented in Fig 6.13(c), 6.13(d), and 6.13(e) are calculated and found to be 87.3%, 94.3%, and 98.3%, respectively. This efficiency is improved by a factor of approximately five compared to the efficiency without the statistical-mechanical approach of viscosity reduction (ref. Fig 6.1).

Further, we have plotted the profiles of the concentration field and have presented them in Fig 6.14. We see that there is more mass dispersion for the lower value of the Schmidt number, Sc, than the higher one (Fig 6.14). So, the EOR efficiency is less for a lower value of the Schmidt number, Sc. In other words, the EOR efficiency is less for the higher value of the diffusion coefficient, D, of CO_2. The value of D can be determined empirically based on field measurements (Gelhar *et al.*, 1992). The present development may be used to validate such empirical values. Here values of the diffusion coefficient, D, are $1.75 \times 10^{-7}\mathrm{m}^2/s$, $8.75 \times 10^{-8}\mathrm{m}^2/s$, and $1.75 \times 10^{-8}\mathrm{m}^2/s$ for the simulations with the Schmidt number, Sc, 1×10^4, 2×10^4, and 1×10^5, respectively. Thus, we see that the simulation with the Schmidt number, $Sc = 1 \times 10^5$, has negligible dispersion (Fig 6.13(e)). Next, we discuss the effects of statistical-mechanical approach of viscosity reduction for the flow at the Reynolds number, $Re = 100$.

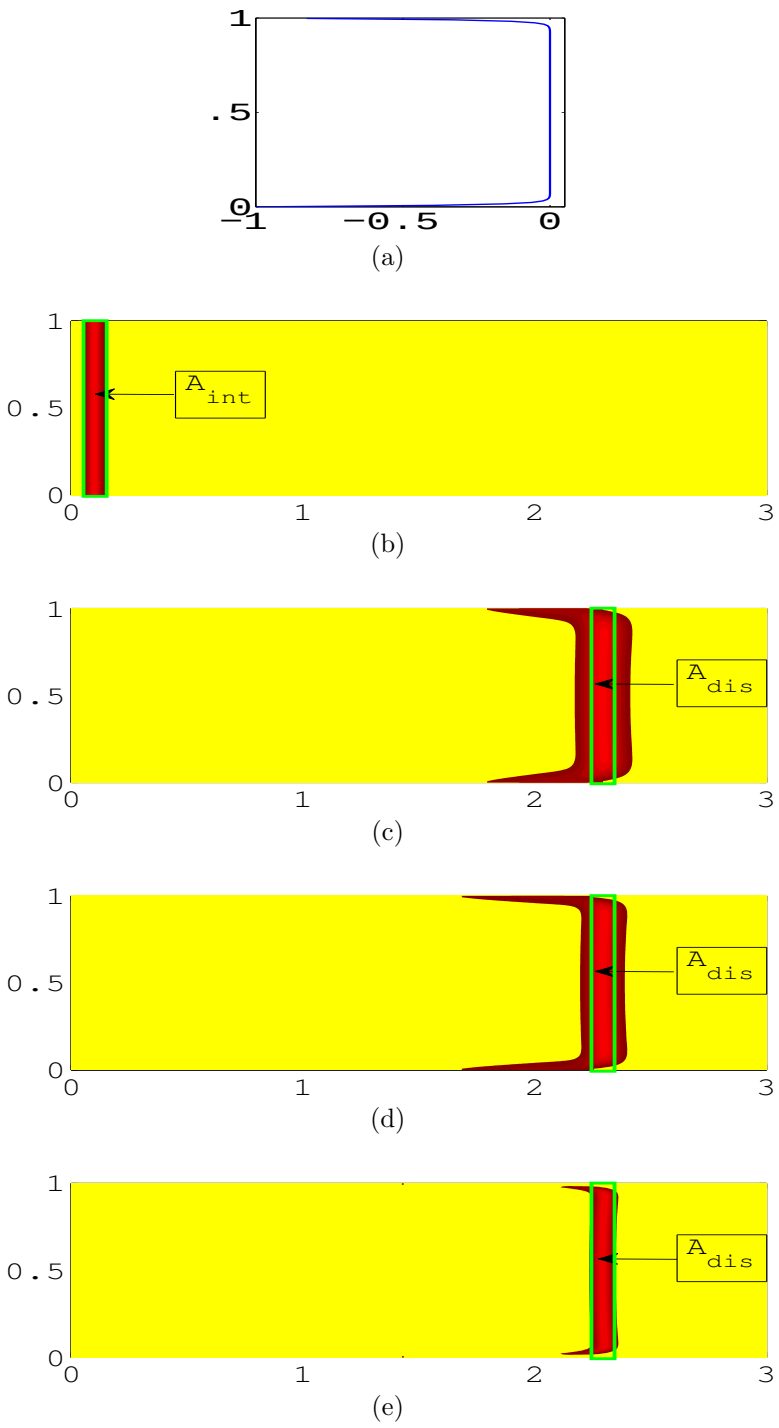

Figure 6.13: Piston-like displacement when viscous effect is reduced. For $Re = 1$, $Da = \phi \times 10^0$, and $\lambda^2 = 7.1 \times 10^{-5}$. (a) Plot of the function $\mu^c(1.5, y)$, (b) Initial stage for any value of Sc, (c) $Sc = 1 \times 10^4$, (d) $Sc = 2 \times 10^4$, (e) $Sc = 1 \times 10^5$. All the simulations are at time, $t = 16.5$ except initial case. The parameter values are listed in table 6.6.

Parameter	value for Fig 6.13 & 6.14	value for Fig 6.15 & 6.16
$L_x \times L_y$	3×1	3×1
$n_x \times n_y$	512×128	512×128
Δt	10^{-2}	10^{-2}
∇P	0.5	0.15
c_φ	0.42	1.4×10^{-3}
$\nabla \varphi$	1	1
λ^2	7.1×10^{-5}	7.1×10^{-5}
Da	$\phi \times 10^{0}$	$\phi \times 10^{-2}$
Re	1	100

Table 6.6: List of the parameters for corresponding figures.

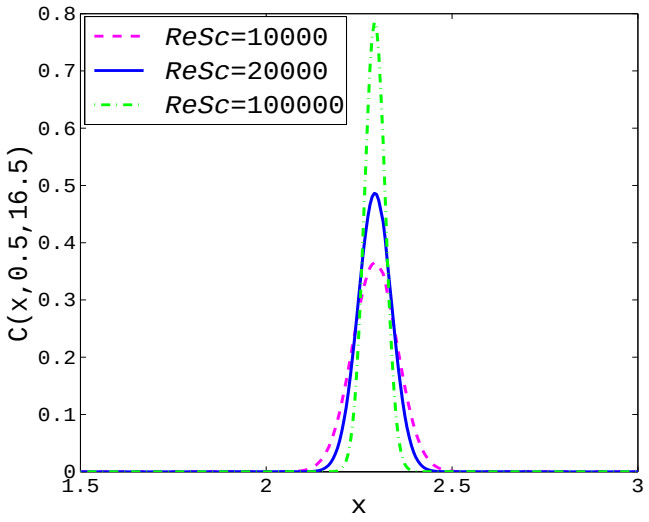

Figure 6.14: Concentration profiles for various value of Sc at time, $t = 16.5$ when $Re = 1$. The profiles are calculated along the center line of the y-axis at $y = 0.5$ for the corresponding simulations presented in Fig 6.13.

6.7.3 Effects of the solvent dissolution for the flow at higher Reynolds number

In this study, we use boundary layer width, $\lambda^2 = 7.1 \times 10^{-5}$, the Darcy number, $Da = \phi \times 10^{-2}$, the Reynolds number, $Re = 100$, and model parameter, $c_\varphi = 1.4 \times 10^{-3}$, and the simulations are presented in Fig 6.15 with the various values of the Schmidt number, Sc. In this case we also consider the three values of the Schmidt numbers, $Sc = 1 \times 10^4,\ 2 \times 10^4$, and 1×10^5 to investigate dispersion of the miscible flow. Others parameter values used for these simulations are listed in table 6.6.

The simulations are depicted in Fig 6.15. First, we plot the function, μ^c in Fig 6.15(a) and we witness the same behavior of the flow as at a low Reynolds number. Further, applying the formula (6.1), the efficiency of the miscible displacement of oil by CO_2 for the simulations which are presented in Fig 6.15(c), 6.15(d), and 6.15(e) are calculated and found to be 77%, 87%, and 94.2%, respectively.

Further, the profiles of the concentration field displayed in Fig 6.16 show that mass dispersion decreases when the value of the Schmidt number, Sc, increases. Thus, displacement efficiency is less for the lower value of Sc. This explanation is the same as for the flow at the Reynolds number, $Re = 1$.

Note that, in the case of high viscosity, $Re = 1$, we use the value of the model parameter, $c_\varphi = 1.4 \times 10^{-3}$, boundary layer width, $\lambda^2 = 7.1 \times 10^{-5}$, the Darcy number, $Da = \phi \times 10^0$, and pressure gradient $\Delta P = 0.5$ to reduce mixture viscosity so that the simulations perform as a piston-like displacement. On the other hand, for the flow at low viscosity, $Re = 100$, we use $c_\varphi = 1.4 \times 10^{-3}$ and $\lambda^2 = 7.1 \times 10^{-5}$ with the Darcy number, $Da = \phi \times 10^{-2}$ and pressure gradient, $\Delta P = 0.15$. The flow for the Reynolds number, $Re = 1$, takes time, $t = 16.5$, to reach the position approximately $x = 2.25$ of the domain (Fig 6.13), whereas the flow for the Reynolds number, $Re = 100$, takes

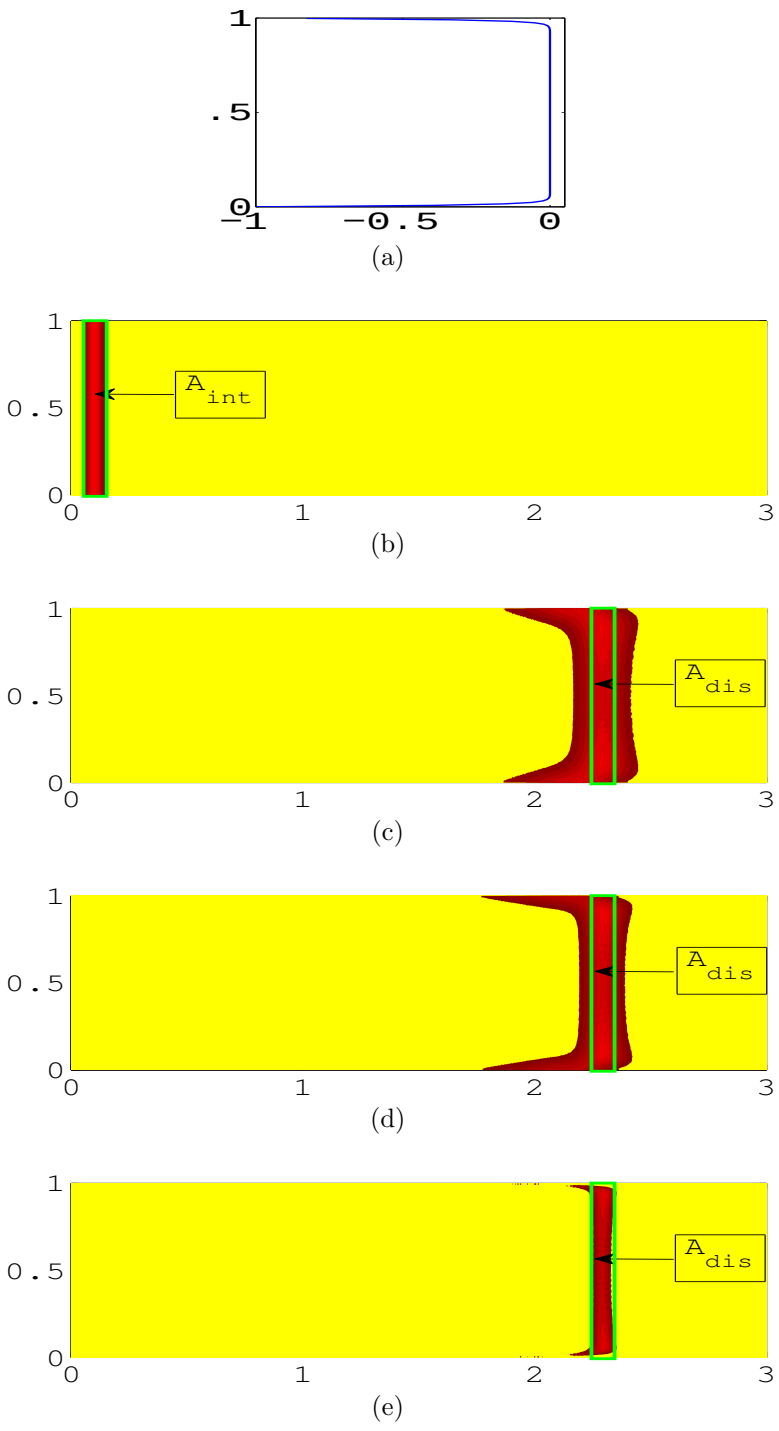

Figure 6.15: Piston-like displacement by reducing viscous effect. For $Re = 100$, $Da = \phi \times 10^{-2}$, and $\lambda^2 = 7.1 \times 10^{-5}$. (a) Plot of the function $\mu^c(1.5, y)$, (b) Initial stage for any value of Sc, (c) $Sc = 1 \times 10^4$, (d) $Sc = 2 \times 10^4$, (e) $Sc = 1 \times 10^5$. All the simulations are at time, $t = 50$, except initial case. The parameter values are listed in table 6.6.

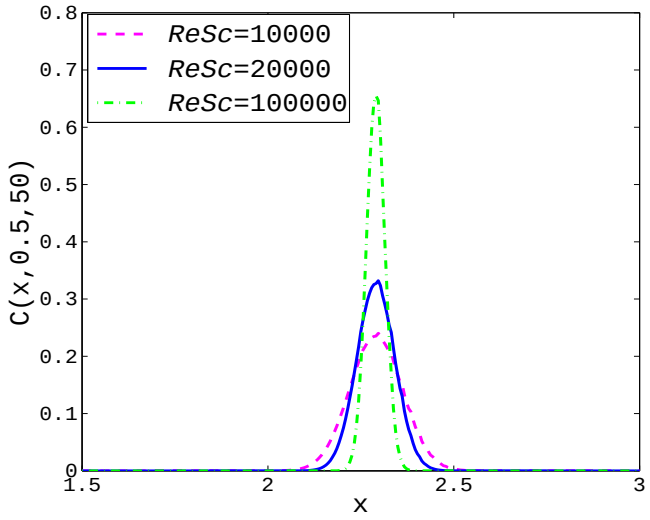

Figure 6.16: Concentration profiles for various value of Sc at time, $t = 50$, when $Re = 100$. The profiles are calculated along the center line of the y-axis at $y = 0.5$ for the corresponding simulations presented in Fig 6.15.

time, $t = 50$, to reach the same position of the domain (Fig 6.15). Here the flow rate of the higher Reynolds number is slower than the flow rate of the lower Reynolds number. This happen because of the lower pressure gradient and the lower Darcy number for the higher Reynolds number.

Therefore, the developed statistical mechanical theory of viscosity performs very well to reduce viscosity of oil and enhances the EOR process. In the next section, we discuss the pressure control to perform piston-like displacement.

6.8 Pressure maintenance

The pressure gradient plays an important role in reservoir simulations to predict the flow rate. Initial production of hydrocarbons from an underground reservoir is

accomplished by the use of natural reservoir pressure (Chen *et al.*, 2006). When the natural reservoir pressure has been depleted, then it is necessary to augment the natural pressure with an external source of pressure. This is usually accomplished by the injection of fluids, either a gas or liquid phase (Islam *et al.*, 2010). One of the purposes of the solvent injection process is to re-pressurize the reservoir and to maintain an optimal pressure level in the reservoir. Hence, the term pressure maintenance is another important parameter among the pertinent parameters in the EOR process.

At this stage we also study pressure gradient effects for the flow at high viscosity and low viscosity.

6.8.1 Optimization of pressure for the flow at low Reynolds number

We investigate the optimal pressure gradient so that the region displaced by CO_2 stays piston-like to help the EOR process. Numerical experiments for various values of the pressure gradient are investigated, among them the simulations for the pressure gradient, $\Delta P = 1,\ 0.5$, and 0.25, are presented in Fig 6.17. All other parameter values used for these simulations are listed in table 6.7. All the simulations exhibited in Fig 6.17 are at approximately the same position of the domain but at a different time. We find the optimal pressure gradient, ΔP, is 0.5. Thus, it is possible to help the EOR process more effectively with piston-like displacement by using this pressure gradient with the pertinent parameters listed in table 6.7.

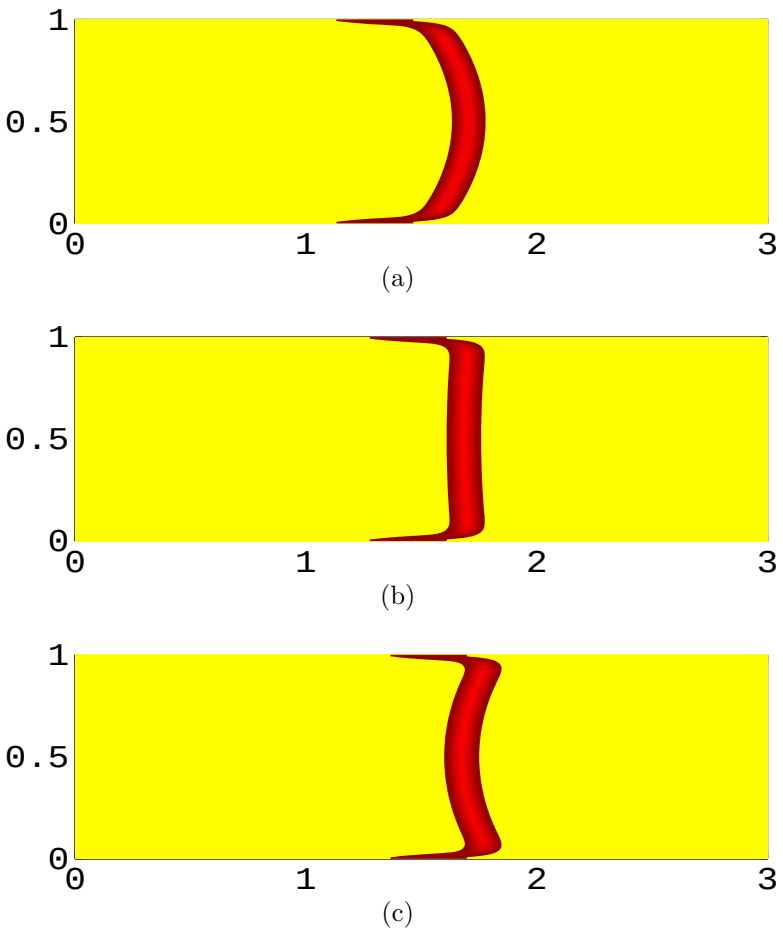

Figure 6.17: Optimized pressure gradient when Darcy number, $Da = \phi \times 10^0$, Reynolds number, $Re = 1$, boundary layer width, $\lambda^2 = 7.1 \times 10^{-5}$ and $ReSc = 2 \times 10^4$. (a) $\Delta P = 1$ at time , $t = 10.7$, (b) $\Delta P = 0.5$ at time , $t = 12$, and (c) $\Delta P = 0.25$ at time , $t = 12.8$. The parameter values are listed in table 6.7.

Parameter	value for Fig 6.17	value for Fig 6.18
$L_x \times L_y$	3×1	3×1
$n_x \times n_y$	512×128	512×128
Δt	10^{-2}	10^{-2}
$\nabla\varphi$	1	1
c_φ	0.42	1.4×10^{-3}
λ^2	7.1×10^{-5}	7.1×10^{-5}
Da	$\phi \times 10^0$	10^{-2}
Re	1	100
$ReSc$	2×10^4	2×10^4

Table 6.7: List of the parameters for corresponding Fig 6.17 and Fig 6.18.

6.8.2 Optimization of pressure for the flow at high Reynolds number

Here we also study the effect of pressure for the flow at the high Reynolds number, $Re = 100$. For the flow at the high Reynolds number, we study numerical experiments for various values of the pressure gradient such as $\Delta P = 0.20,\ 0.15$ and 0.125, and other parameters are listed in table 6.7. All the simulations exhibited in Fig 6.18 are close to the same position of the domain but at a different time. We find that the optimal pressure gradient, ΔP, is 0.15. Thus, it is possible to help the EOR process more effectively with a piston-like displacement by using this pressure gradient with the pertinent parameters listed in table 6.7.

Therefore, for the flow at low Reynolds number, *i.e.,* $Re = 1$, we need the optimal pressure gradient, $\Delta P = 0.5$, to keep a piston-like displacement (Fig 6.17(b)). On the

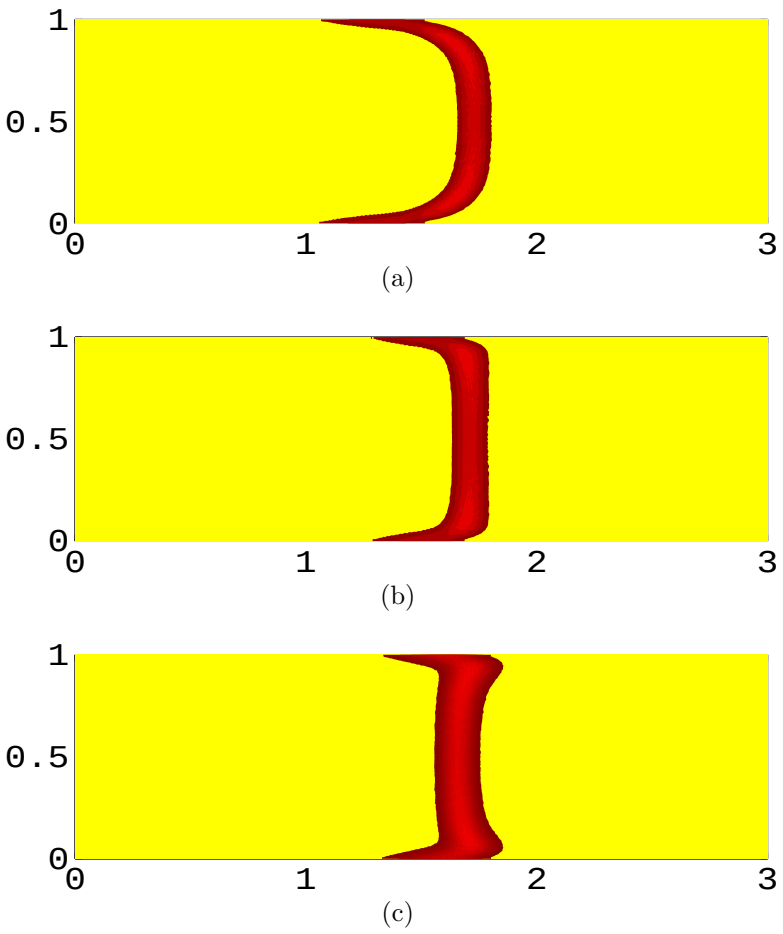

Figure 6.18: Pressure optimization when Darcy number, $Da = \phi \times 10^{-2}$, Reynolds number, $Re = 100$, boundary layer width, $\lambda^2 = 7.1 \times 10^{-5}$ and $ReSc = 2 \times 10^4$. (a) $\Delta P = 0.20$ at time , $t = 28$, (b) $\Delta P = 0.15$ at time , $t = 35.4$, and (c) $\Delta P = 0.125$ at time , $t = 40$. All the parameter values are listed in table 6.7.

other hand, the optimal pressure gradient, $\Delta P = 0.15$, is needed for the flow at the high Reynolds number, *i.e.,* $Re = 100$ (Fig 6.18(b)). Here we should mention that for the flow at the high viscosity, the pressure gradient should be about 3.3 times higher than for the lower viscosity to maintain a piston-like displacement (Fig 6.17(b) and Fig 6.18(b)). As we see in Fig 6.17(b) for the high viscosity case, it takes time, $t = 12$ to reach the position about $x = 2.25$ of the domain, whereas for the low viscosity case, it takes time, $t = 35.4$ to reach the same position (Fig 6.18(b)). Here the flow in the higher viscosity case is faster than the flow in lower viscosity case, because the lower pressure gradient and the smaller Darcy number are considered in the lower viscosity case.

6.9 Summary

Viscosity reduction is one of the important parts of research in the oil industries. We investigate the effects of viscosity and permeability on the miscible displacement of oil by CO_2. We also study the effects of boundary layer width and dispersion of mass transport phenomena on the miscible displacement of the fluids. We have found that CO_2 dissolution depends mostly on viscosity rather than permeability. In addition, the optimum pressure gradient is studied to enhance the EOR process with piston like displacement.

Chapter 7

Concluding remarks and future work

In this chapter, we summarize the present research on the miscible displacement process of two fluids in a porous medium. Finally, we briefly discuss some future research directions.

7.1 Conclusion

The study of accurate and efficient flow in porous media at pore scale is still a challenging and interesting topic (Gerritsen & Durlofsky, 2005). We have developed a generalized mathematical model by using upscaling methodology for multiscale features of the flow and porous media where a statistical mechanical theory of viscosity has been developed to resolve the effect of CO_2 dissolution. The pressure drag and the skin friction of the porous medium have been modelled by combining the statistical mechanical approach with the Darcy's law. In addition, to meet the computational challenges, a multigrid method has been used to solve the system of linear equa-

tions so that the overall computational cost could be optimized. A streamline based Lagrangian method has been developed to model the miscible mass transport mechanism.

We have compared the results of this Lagrangian method with that of an equivalent Eulerian method. The Lagrangian method performs very well by producing non-oscillatory solutions without numerical diffusion. This method is about one hundred times faster in time step. In addition, the Lagrangian method is able to refine the mesh double than Eulerian method to capture the small scale physics, however, if we refine the mesh so that it works twice as efficient as the in the Eulerian method we have to reduce time step by at least a factor of 2, but in the Lagrangian we method do not need to reduce the time step to refine the mesh. Therefore, the Lagrangian method can produce highly accurate solutions with a faster speed (see subsection 5.3.2 and Figs 5.6 & 5.7). Furthermore, this method resolves the mass conservation law more accurately compared to a representative Eulerian method (see, subsection 5.4.4 and Fig 5.15). Thus we see that the Lagrangian method is able to simulate mass transport phenomena for the miscible displacement in porous media more accurately and efficiently with an optimal computational cost. Therefore this method can be applied to study the fluid flow in oil reservoir.

Viscosity reduction is one of the most important parts of research for the oil industries to improve oil recovery (Ghosh & Shalabi, 2011; Haskin & Alston, 1989), and to transport highly viscous crude oil (Homayuni *et al.*, 2011). We have found that fluid flow in a reservoir mostly depends on viscosity rather than permeability (ref. Fig 6.1). We have focused on the development of a generalized upscaling model employing a statistical-mechanical approach to resolve the effects of CO_2 dissolution, and studied the factors for optimizing the pressure drag and the skin friction which are exerted by the porous media at the reservoir scale. Finally, the potentiality of the statistical

mechanical approach has been investigated, and we have found that the displacement pattern takes a form as if the CO_2 sample migrates like a piston without noticeable distortion (see section 6.7 and Figs 6.13 & 6.15). In other words, this approach to viscosity reduction may help the EOR processes by increasing the rate of oil production.

7.2 Future research directions

The numerical simulations presented in this thesis indicate that the streamline based Lagrangian method may be an efficient technique to study miscible fluid flows in porous media. Note that the present model exhibits much less artificial diffusion compared to similar model and does not require a time step restriction for numerical stability. The future potential research directions can be addressed as follows:
Three-dimensional simulations will help better to understand the flow behavior in a oil reservoir. Our proposed model may be extended for three-dimensional simulations of miscible displacement. In addition, this model may be applied to the investigation of miscible displacement through fractured porous media. Chen *et al.* (2006); Brand *et al.* (1991); Shubin & Bell (1984) and Ewing (1983) described the grid orientation problem that affects the oil reservoir simulations. The newly developed Lagrangian method may be applied to address this grid orientation problem.

Bibliography

Abdurahman, N. H., Rosli, Y. M., Azhari, N. H. & Hayder, B. A. 2012 Pipeline transportation of viscous crudes as concentrated oil-in-water emulsions. *Journal of Petroleum Science and Engineering* **90-91**, 139–144.

Adams, D. M. 1982 Experiences with waterflooding lloydminster heavy-oil reservoirs. *Journal of Petroleum Technology* **34(8)**, 1643–1650.

Alam, J. & Bowman, J. C. 2002 Energy-conserving simulation of incompressible electro-osmotic and pressure-driven flow. *Theoretical and Computational Fluid Dynamics* **16**, 13–150.

Alam, J. M. & Ahammad, M. J. 2013 Pressure drag and skin friction effects in a miscible flow through porous media. *Journal of Fluid Engineering* **submitted**.

Alam, J. M. & Penney, J. M. 2012 A lagrangian approach for modelling electrokinetic mass transfer in microchannels. *International Journal of Heat and Mass Transfer* **55**, 7847–7857.

Alazmi, B. & Vafai, K. 2004 Analysis of variable porosity, thermal dispersion, and local thermal non-equilibrium on free surface flows through porous media. *Journal of Heat Transfer* **126**, 389 – 399.

Bai, M. & Elsworh, D. 1995 On the modeling of miscible flow in multi-component porous media. *Transport in Porous Media* **21**, 19–46.

Batycky, R. P., Blunt, M. J. & Thiele, M. R. 1997 A 3D field-scale streamline based reservoir simulator. *SPE Reservoir Eval Eng* **12(4)**, 246–254.

Bear, J. 1972 *Dynamic of fluids in porous media*, 1st edn. American Elsevier publishing company.

Bear, J. & Bachmat, Y. 1990 *Introduction to Modeling of Transport Phenomena in porous media*, 1st edn. Kluwer Academic Publishers.

Behie, A. & Forsyth, P. A. 1983 Multigrid solution of the pressure equation in reservoir simulation. *SPE Journal* **23(4)**, 623–632.

Bhogeswara, R. & Killough, J. E. 1992 Domain decomposition and multigrid solvers for flow simulation in porous media on distributed memory parallel processors. *Journal of Scientific Computing* **7(2)**, 127–162.

Booth, R. 2008 Miscible flow through porous media. Phd thesis, University of Oxford, UK.

Brand, C. W., Heinemann, J. E. & Aziz, K. 1991 The grid orientation effect in reservoir simulation. *SPE Symposium on Reservoir Simulation, 17-20 February 1991, Anaheim, California* **SPE 21228**, 275–286.

Brandt, A. 1972 Multi-level adaptive technique for fast numerical solution to boundary-value problems. *Proceedings of the third international conference on numerical methods in fluid Dynamics, lect. Notes phys.* **18**, 82–89.

Brandt, A. 1977 Multi-level adaptive solutions to boundary-value problems. *Math. Comp.* **31**, 333–390.

Brinkman, H. C. 1947 A calculation of the viscous force exerted by a flowing fluid on a dense swarm of particles. *Appl. Sci. Res* **A1**, 27–34.

Celia, M. A., Russell, T. F., Herrera, I. & Ewing, R. E. 1990 An eulerian-lagrangian localized adjoint method for the advection-diffusion equation. *Adv. water Resources* **13(4)**, 187–206.

Chaudhary, A. S. 2011 Shale oil production performance from a stimulated reservoir volume. M.sc thesis, Petroleum Engineering, Texas A & M University, USA.

Chen, S. C. & Vafai, K. 1996 Analysis of free surface momentum and energy transport in porous media. *Numerical Heat Transfer* **29(A)**, 281 – 296.

Chen, Z. 2007 *Reservoir Simulation- Mathematical Techniques in Oil Recovery*. SIAM.

Chen, Z., Huan, G. & Ma, Y. 2006 *Computational methods for multiphase flows in porous media*. SIAM.

Chorin, A. J. 1968 Numerical solution of the navier-stokes equations. *Math. COMPUT.* **22(104)**, 745–762.

Christie, M. A., Watt, U. H. & Blunt, M. J. 2001 Tenth spe comparative solution project: A comparison of upscaling techniques. *SPE Reservoir Evaluation & Engineering* **4(4)**, 308–317.

Chung, T. J. 2010 *Computational Fluid Dynamics*, 2nd edn. Cambridge university press.

Clees, T. & Ganzer, L. 2007 An efficient algebraic multigrid solver strategy for adaptive reservoir simulation. *SPE reservoir simulation symposium 2007, USA* p. SPE 105789.

Courant, R., Fredrichs, K. O. & Lewy, H. 1928 Uber die differenzengleichungen der mathematischen physik. *Math. Ann* **100**, 32.

Crane, M. J. & Blunt, M. J. 1999 Streamline based simulation of solute transport. *Water Resources Research* **35(10)**, 3061–3078.

Cussler, E. L. 1997 *Diffusion: Mass Transfer in Fluid Systems*, 2nd edn. Cambridge University Press.

Dehghan, M. 2004 Weighted finite difference techniques for the one-dimensional convection-diffusion equation. *Applied Mathematics and Computation* **147**, 307–319.

deLemos, M. J. S. 2006 *Turbulence in Porous Media modeling and applications*, 1st edn. ELSEVIER.

Ehlers, W. & Bluhm, J. 2002 *Porous Media- Theory, experiments and numerical applications*. Springer.

Elsayed, S. A., Baker, R., Churcher, P. L. & Edmunds, A. C. 1993 Multidisciplinary reservoir characterization and simulation study of the weyburn unit. *Journal of Petroleum Technology* **45(10)**, 930–934,973.

Ergun, S. 1952 Fluid flow through packed columns. *Chem. Engng. Prog* **48(2)**, 89–94.

Ewing, R. E. 1983 *The Mathematics of Reservoir Simulation*. SIAM.

Fancher, G. H. & Lewis, J. A. 1933 Flow of simple fluids through porous materials. *Ind. Engng. Chem.* **25(10)**, 1139–1147.

Farajzadeh, R. 2009 Enhanced transport phenomena in CO_2 sequestration and CO_2 EOR. Phd thesis, Petroleum Engineering, Delft University of Technology, The Netherlands.

Fedorenko, R. P. 1962 A relaxation method for solving elliptic equations. *USSR Comput. Math. Math. Phys.* **1**, 1092–1096.

Fedorenko, R. P. 1964 The speed of convergence of an iterative process. *USSR Comput. Math. Math. Phys.* **4**, 227–235.

Fletcher, C. A. J. 1990 *Computational Techniques for Fluid Dynamics1 - fundamental and general technique*, 2nd edn. Springer-Verlag.

Garibotti, C. R. & Peszyǹska, M. 2009 Upscaling non-darcy flow. *Transp Porous Med* **80**, 401–430.

Gavin, L. 2004 Pre-darcy flow: a missing piece of the improved oil recovery puzzle? *Society of Petroleum Engineers* p. SPE 89433.

Gelhar, L. W., Welty, C. & Rehfeldt, K. R. 1992 A critical review of data on field-scale dispersion in aquifers. *Water resources Research* **28**, 1955–1974.

Gerritsen, M. G. & Durlofsky, L. J. 2005 Modeling fluid flow in oil reservoirs. *Annu. Rev. Fluid Mech.* **37**, 211–238.

Ghosh, B. & Shalabi, E. W. A. 2011 Solvent induced oil viscosity reduction and its effect on waterflood recovery efficiency. *Advances in Petroleum Exploration and Development* **2(2)**, 24 – 31.

Gozalpour, F., Ren, S. R. & Tohidi, B. 2005 CO_2 EOR and storage in oil reservoirs. *Oil & Gas Science and Technology-Rev. IFP* **60(3)**, 537–546.

Gray, W. G. & Lee, P. C. Y. 1977 On the theorems for local volume averaging of multiphase systems. *Int. J. Multiphase Flow* **3(4)**, 333–340.

Green, D. W. & Willhite, G. P. 1998 *Enhanced Oil Recovery*. Society of Petroleum Engineers.

Guo, Z. & Zhao, T. S. 2002 Lattice boltzmann model for incompressible flows through a porous medium. *Physical review E* **66**, 036304–(1–9).

Harlow, F. H. & Welch, J. E. 1965 Numerical calculation of time-dependent viscous incompressible flow of fluid with free surface. *Physics of Fluids* **8(12)**, 2182–2189.

Haskin, H. K. & Alston, R. B. 1989 An evaluation of CO_2 huff 'n' puff tests in texas. *Journal of Petroleum Technology* **41(2)**, 177–184.

Hasle, G., Lie, K.-A. & Quak, E. 2007 *Geometric Modelling, Numerical Simulation, and Optimization: Applied Mathematics at SINTEF*. Springer.

Holden, H. 2010 *Splitting Methods for Partial Differential Equations with Rough Solutions - Analysis and MATLAB programs*, april edn. European Mathematical Society.

Holtz, M. H., Nance, P. K. & Finley, R. J. 2001 Reduction of Greenhouse Gas Emissions through CO_2 EOR in Texas. *Environmental Geosciences* **8(3)**, 187–199.

Homayuni, F., Hamidi, A. A., Vatani, A., Shaygani, A. A. & Dana, R. F. 2011 Viscosity reduction of heavy and extra heavy crude oils by pulsed electric field. *Petroleum Science and Technology* **29**, 2050–2060.

Homsy, G. M. 1987 Viscous fingering in porous media. *Ann. Rev. Fluid Mech.* **19**, 271–311.

Hsu, C. T. & Cheng, P. 1990 Thermal dispersion in a porous medium. *Int. J. Heat Mass Transfer* **33(8)**, 1587–1597.

Hubbert, M. K. 1956 Darcys law and the field equations of the flow of underground fluids. *Published in Petroleum Transactions* **207**, 222–239.

Islam, M. R., Moussavizadegan, S. H., Mustafiz, S. & Abou-Kassem, J. H. 2010 *Advanced petroleum reservoir simulation*. Scrivener, Wiley.

Jenny, P., Lee, S. H. & Tchelepi, H. A. 2006 Adaptive fully implicit multi-scale finite-volume method for multi-phase flow and transport in heterogeneous porous media. *Journal of Computational Physics* **217(2)**, 627–641.

Jha, B., Cueto-Felgueroso, L. & Juanes, R. 2013 Pressure-driven miscible two-fluid channel flow with density gradients. *Physical Review letter* **111**, 144501.

Johnson, N. L. 1996 The legacy and future of CFD at LOS ALAMOS. *Canadian CFD conference, Ottawa* .

Kjonsvik, D. & Alvestad, J. 1995 An analytical method for calculating the performance of heterogeneous reservoirs and its use in uncertainty analysis. *Special Publications* **84**, 29 – 41.

Koch, D. L. & Brady, J. F. 1985 Dispersion in fixed beds. *Journal of Fluid Mechanics* **154**, 399–427.

Koval, E. J. 1963 A method for predicting the performance of unstable miscible displacement in heterogeneous media. *SPE Journal* **3(2)**, 145–154.

Kumar, M., Hoang, V. & Satick, C. 2005 High mobility ratio water flood performance prediction: Challenges and new insights. *Reservoir Evaluation & Engineering* **11(1)**, 186–196.

Kumar, M., Hoang, V., Satik, C. & Rojas, D. 2008 High-mobility-ratio water flooded performance prediction: Challenges and new insights. *Reservoir Evaluation & Engineers* pp. 186–196.

Kundu, P. K. & Cohen, I. M. 2004 *Fluid Mechanics*, 3rd edn. Elsevier Academic Press, USA.

Kundu, P. K., Cohen, I. M. & Dowling, D. R. 2012 *Fluid Mechanics*, 5th edn. Elsevier Academic Press, USA.

Latil, M. 1980 *Enhanced Oil Recovery*. Editions TECHNIP, Paris.

Lorenz, J., Bray, B. G. & Clark, C. R. 1964 Calculating viscosities of reservoir fluids from their compositions. *J. Pet. Tech.* pp. 1171–1176.

Ma, H. & Ruth, D. W. 1993 The microscopic analysis of high forchheimer number flow in porous media. *Transport in Porous Media* **13(2)**, 139–160.

MacLachlan, S. P., Tang, J. M. & Vuik, C. 2008 Fast and robust solvers for pressure correction in bubbly flow problems. *Journal of Computational Physics* **227**, 97429761.

McGuire, P. L., Redman, R. S., , Jhaveri, B. S., Yancey, K. E. & Ning, S. X. 2005 Viscosity reduction wag: An effective eor process for north slope viscous oil. *SPE Western Regional Meeting held on 30 March - 1 April 2005, Irvine, CA, USA,* **SPE 93914**, 1–10.

Mekeon, T. J. & Chu, W.-S. 1987 A multigrid model for steady flow in partially saturated porous media. *Water Resources Research* **23**, 542–550.

Mohsin, A. J. & Anazi, A. B. D. 2009 A comparison study of the of the CO_2-oil physical properties-literature correlations accuracy using visual basic modeling technique. *Oil and Gas Business* **60(5)**, 287–291.

Nathan, S. & Niall, T. R. 2006 Modeling electroosmotic and pressure-driven flows in porous microfluidic devices: Zeta potential and porosity changes near the channel walls. *The Jornal of Chemcal Physics* **125**, 94714–1–12.

Nguyen, T. V. 1986 Experimental study of non-darcy flow through perforations. *SPE Annual Technical Conference and Exhibition, 5-8 October 1986, New Orleans, Louisiana* p. SPE 15473.

Nobakht, M., Moghadam, S. & Gu, Y. 2007 Effects of viscous and capillary forces on CO_2 enhanced oil recovery under reservoir conditions. *Energy & Fuels* **21**, 3469 – 3476.

Nourozieh, H., Kariznovi, M., Jamialahmadi, M. & Shahrabadi, A. 2008 Develop a new model for saturation calculation in streamline simulation. *Simulator Development* p. SPE 114038.

Noye, B. J. & Tan, H. H. 1988 A third-order semi-implicit finite difference method for solving the one dimensional convectiondiffusion equation. *International Journal for Numerical Methods in Engineering* **26**, 1615–1629.

Obi, E.-O. & Blunt, M. J. 2004 Streamline-based simulation of advective dispersive solute transport. *Advances in Water Resources* **27**, 913–924.

Patankar, S. V. 1980 *Numerical heat transfer and fluid flow*. Hemisphere publishing corporation.

Peaceman, D. W. & Rachford, J. 1962 Numerical calculation of multidimensional miscible displacement. *SPE Journal* **2(4)**, 327–339.

Pletcher, R. H., Tannehill, J. C. & Anderson, D. A. 2013 *Computational Fluid Mechanics and Heat transfer*, 3rd edn. Taylor & Francis group.

Popov, P., Efendiev, Y. & Qin, G. 2009 Multiscale modeling and simulations of flows in naturally fractured karst reservoirs. *Communications in computational physics* **6(1)**, 162–184.

Pruess, K. & Zhang, K. 2008 Numerical modeling studies of the dissolution - diffusion - convection process during CO_2 storage in saline aquifers. *Lawrence Berkeley National Laboratory, California* **Technical Report LBNL-1243E**, 1–32.

Sahu, K. C., Ding, H., Valluri, P. & Matar, O. K. 2009 Pressure-driven miscible two-fluid channel flow with density gradients. *Physics of Fluid* **21**, 043603.

Saniere, A., Hnaut, I. & Argillier, J. F. 2004 Pipeline transportation of heavy oils, a strategic, economic and technological challenge. *Oil & Gas Science and Technology Rev. IFP* **59**, 455–466.

Sankaranarayanan, S., Shankar, N. J. & Cheong, H. F. 1998 Three- dimensional finite difference model for transport of conservative pollutants. *Ocean Engng-Elsevier* **25(6)**, 425–442.

Semmelbeck, M. E. & HoldItch, S. A. 1988 The effects of mud-filtrate invasion on the interpretation of induction logs. *Society of Petroleum Engineers* pp. 386 –392.

Sen, R. 2008 Biotechnology in petroleum recovery: The microbial EOR. *Progress in Energy and Combustion Science* **34(6)**, 714–724.

Shubin, G. R. & Bell, J. B. 1984 An analysis of the grid orientation effect in numerical simulation of miscible displacement. *Computer Methods in Applied Mechanics and Engineering* **47(1-2)**, 47–71.

Slattery, J. C. 1967 Flow of viscoelastic fluids through porous media. *AIChE* **13(6)**, 1066–1071.

Soni, J. P., ISLAM, N. & Basak', P. 1978 An experimental evaluation of non-darcian flow in porous media. *Journal of Hydrology* **38**, 231–241.

Tao, R. & Xu, X. 2006 Reducing the viscosity of crude oil by pulsed electric or magnetic field. *Energy & Fuels* **20**, 2046–2051.

Texas 2012 http://www.texasenergyfoundation.org/us-policy-shift-to-carbon-capture-utilization-and-storage/. *Texas Energy Foundation.* .

Thiele, M. R., Batycky, R. P., Blunt, M. J., Jr., F. M. O. & U, S. 1996 Simulating flow in heterogeneous systems using streamtubes and streamlines. *SPE Reservoir Engineering* **1(1)**, 5–12.

Thiele, M. R., Batycky, R. P. & Fenwick, D. H. 2010 Streamline simulation for modern reservoir-engineering work flows. *Distinguished Author Series* pp. 64–70.

Udey, N. & Spanos, T. J. T. 1993 The equations of miscible flow with negligible molecular diffusion. *Transport in Porous Media* **10**, 1–41.

Vafai, K. & Tien, C. 1982 Boundary and inertial effects on convective mass transfer in porous media. *International Journal of Heat and Mass Transfer* **25(8)**, 1183–1190.

Whitaker, S. 1969 Advances in theory of fluid motion in porous media. *Ind. Eng. Chem.* **61**, 14–28.

Whitaker, S. 1986 Flow in porous media II: The governing equations for immiscible, two-phase flow. *Transport in Porous Media* **1**, 105–125.

Whitaker, S. 1996 The forchheimer equation: a theoretical developments. *Transport in Porous Media* **25**, 27–61.

Yu, R., Bian, Y., Li, Y., Zhang, X., Yan, J., Wang, H. & Wang, K. 2012 Non-darcy flow numerical simulation of xpj low permeability reservoir. *Journal of Petroleum Science and Engineering* **92-93**, 40–47.

Zhang, Q. & Prosperetti, A. 2009 Pressure-driven flow in a two-dimensional channel with porous walls. *J. Fluid Mech.* **631**, 1–21.

Zhou, Y. C., Patnaik, B. S. V., Wan, D. C. & Wei, G. W. 2003 DSC solution for flow in a staggered double lid driven cavity. *Int. J. Numer. Meth. Engng* **57**, 211–234.